

# Exploring New Physics in Ultracold Quantum Gases: High Spin Fermions and Non-Trivial Background Manifolds

Dissertation

Presented in Partial Fulfillment of the Requirements for the Degree Doctor of Philosophy in the Graduate School of The Ohio State University

By

Biao Huang, B.S.

Graduate Program in Physics

The Ohio State University

2016

Dissertation Committee:

Professor Tin-Lun Ho, Advisor

Professor Eric Braaten

Professor Richard Furnstahl

Professor Jay Gupta

© Copyright by

Biao Huang

2016

## Abstract

A large portion of cold atom researches have been devoted to finding novel systems by taking advantage of the high manipulability of cold atom experiments. From the original Bose-Einstein condensates, to the recent realization of Harper-Hofstadter models, cold atoms have kept feeding the world with surprises of realizing systems that were once thought to be purely theoretical constructions. Such trend of research have propelled this thesis to seek for possible new physics based on current cold atom technologies, and to discuss its unique properties.

In the first part, we will discuss the local spin ordering for systems made of large spin fermions. This is a generalization of the usual magnetic ordering for spin-1/2 systems, and we shall see that the large spin characters have made qualitative difference. Here we provide a general tensorial classification for fermionic systems of arbitrary spin, and discussed their general character and associated topological defects in the Majorana representation. We have also identified a series of highly symmetric “Platonic solid states” that are stable against perturbations, and have good chance of being observed in experiments.

The second part focuses on another topic, which is the effects of background manifold on the quantum systems residing on it. We will first examine the vortex physics for Bose condensates confined on non-trivial 2D surfaces with synthetic gauge fields. In particular, we discuss in detail the cylindrical surface as an example where two types of vortices and a peculiar “necklace” pattern show up as a result of the confining geometry. Then we discuss

the topic of Hall viscosity, a unique dissipationless viscosity coefficient that is related to the adiabatic change of space geometry. We relate it to the density response of a system, and therefore provide an alternative way to compute and measure such a quantity.

This is dedicated to my parents

## Acknowledgments

I am deeply indebted to my advisor Prof. Tin-Lun Ho for his guidance and inspirations during my Ph.D. researches. His choice as well as sharp views of problems have always been enlightening for me. Especially, his focus on experiment-related issues, and the preference of looking at the underpinning principles in physical problems have deep influence on me. Also, I am very grateful to have such a generous advisor who has supported me to quite a lot of conference, summer schools and visitings during my Ph.D. period. A great deal of my knowledge was gained from such opportunities.

It has been a great pleasure to collaborate with Prof. Yuan-Ming Lu and Prof. Nandini Trivedi at OSU, and Prof. Yong Baek Kim from Toronto University in the final year of my Ph.D. life. These collaborations have extended my research into the fascinating field of spin liquid, and enabled me to use the numerical technique of quantum Monte-Carlo. Such knowledge will be very useful for my future researches, and I am grateful that they have patiently led me into the field.

I am grateful to my committee members, Prof. Eric Braaten, Prof. Dick Furnstahl, and Prof. Jay Gupta. They have been very supportive throughout my Ph.D. period to review the progress of my research. I learnt the GSL library for C++ based numerical calculations entirely from Prof. Furnstahl, and he is always ready to provide help whenever I have some problems about numerics.

In the beginning of my Ph.D. studies, the condensed matter and many-body physics courses provided by Prof. Mohit Randeria, and the discussion with Dr. Shizhong Zhang and Dr. Edward Taylor consisted of my “condensed matter and cold atom 101” series. I was fortunate to have met these nice teachers with broad knowledge in various aspects. I also would like to thank all the people I have met during my visit to Tsinghua University in my third year, and the hospitality of Prof. Hui Zhai’s group during that time. The discussions during lunch hours had been a great fun to me. Further, I would like to thank all the students and postdocs in the condensed matter group of OSU. They have been very generous about their time to help me with various difficulties in researches. Last but not least, I would like to thank my parents for all of their support for my study and career in physics. They have never hesitated to encourage me or to support my decisions heartfully.

## Vita

July 13th, 1987 ..... Born – Gutian, China

2009 ..... B.S. Beijing Normal University, China

## Publications

### **Spinor Condensates on a Cylindrical Surface in Synthetic Gauge Fields**

Tin-Lun Ho and **Biao Huang**

Physical Review Letters **115**, 155304 (2015).

### **Hall viscosity revealed via density response**

**Biao Huang**

Physical Review B **91**, 235101 (2015).

### **Local spin structure of large spin fermions**

Tin-Lun Ho and **Biao Huang**

Physical Review A **91**, 043601 (2015).

## Fields of Study

Major Field: Physics



# Table of Contents

	<b>Page</b>
Abstract . . . . .	ii
Dedication . . . . .	iv
Acknowledgments . . . . .	v
Vita . . . . .	vii
List of Tables . . . . .	xi
List of Figures . . . . .	xii
1. General Introduction . . . . .	1
2. Local Spin Order for Large Spin Fermion Systems . . . . .	5
2.1 Introduction . . . . .	5
2.2 Symmetry Classifications . . . . .	8
2.2.1 Bosonic Spinor Condensate and Fermionic Pairing . . . . .	8
2.2.2 Local Spin Ordering . . . . .	9
2.2.3 Majorana Representation on a Bloch Sphere . . . . .	13
2.3 Topological defects . . . . .	15
2.4 Energetic considerations and Platonic solid inert states . . . . .	19
2.5 Phase Transition: Ginzburg-Landau Theory . . . . .	23
2.6 Concluding Remarks . . . . .	27
2.7 Appendix . . . . .	29
2.7.1 Numerical Algorithm for Exploring Phase Diagram . . . . .	29
2.7.2 CG coefficients, $3j$ and $6j$ Symbols . . . . .	31

2.7.3	Relation Between the Components of Generalized Spherical Harmonic Operators $[\tilde{Y}_M^{(L)}(\mathbf{F})]_{\mu\nu}$ and the Clebsch-Gordon Coefficients $\langle f\mu LM; f\nu\rangle$ . . . . .	33
2.7.4	Ginzburg-Landau: General Formulation . . . . .	34
2.7.5	Ginzburg-Landau: Dimensionless Variables . . . . .	39
2.7.6	Ginzburg-Landau: Angular Momentum Decomposition . . . . .	40
3.	Non-Trivial Manifolds for Spinor Condensates in Synthetic Gauge Fields . . . . .	44
3.1	Introduction . . . . .	44
3.1.1	Preliminaries of Optical Traps . . . . .	45
3.1.2	Synthetic Gauge Fields: General Discussions . . . . .	49
3.2	Realization of a BEC on a cylindrical surface with synthetic gauge fields in Landau gauge . . . . .	54
3.2.1	Trapping BEC on a cylindrical surface . . . . .	55
3.2.2	Synthetic gauge fields in Landau gauge . . . . .	57
3.3	Vortex Physics on a Cylindrical Surface . . . . .	59
3.3.1	Lowest Landau Level Limit for Condensates . . . . .	59
3.3.2	Isolated vortex on a cylindrical surface . . . . .	61
3.3.3	Vortex array on a cylindrical surface . . . . .	64
3.3.4	Experimental Signatures . . . . .	66
3.4	Conclusions and Outlook: General Compact Surfaces . . . . .	67
3.4.1	Tentative Schemes for Spherical and Toroidal Surfaces . . . . .	68
3.4.2	Vortices on Compact Surfaces: Hopf-Poincaré Index Theorem . . . . .	70
3.5	Appendix . . . . .	72
3.5.1	Synthetic Abelian and Non-Abelian Gauge Fields . . . . .	72
3.5.2	Details of the Variational Calculation . . . . .	74
4.	Hall Viscosity and its Signatures in Density Response Functions . . . . .	78
4.1	Introduction . . . . .	78
4.1.1	Hydrodynamics . . . . .	79
4.1.2	Dissipation . . . . .	81
4.1.3	Independent Components . . . . .	82
4.2	Adiabatic Approach . . . . .	86
4.2.1	Berry Curvature for Distortion . . . . .	87
4.2.2	Distortion and Metric . . . . .	88
4.2.3	Distortion of Unit Parallelogram . . . . .	88
4.2.4	Example: Quantum Hall Systems . . . . .	92
4.3	Wen-Zee Effective Theory . . . . .	94
4.4	Density Response . . . . .	99
4.4.1	Kubo Formulae Method . . . . .	100

4.4.2	Example: Integer Quantum Hall Systems . . . . .	103
4.4.3	Hydrodynamic analysis . . . . .	105
4.4.4	Obtaining Hall Viscosity through Density Response Signatures . . . . .	107
4.5	Conclusion and outlook . . . . .	109
	Bibliography . . . . .	111

## List of Tables

Table	Page
2.1 Examples of bosonic atoms and their hyperfine spins . . . . .	6
2.2 Examples of fermionic atoms and their hyperfine spins . . . . .	7
2.3 Exploration of $T = 0$ mean field phase diagram for spin $f = 21/2$ fermion systems in the presence of spin exchange interactions. $k_n = (6\pi^2 n)^{1/3}$ , where $n$ is the <i>total</i> number of particles in the system. $\{a_F, F = 0, 2, \dots, 2f - 1\}$ are scattering channels with total spin $F$ . The spin orders of different sectors are represented in Majorana representation. $ \Phi^{(L)}\rangle$ sector would contain $2L$ points ( $L$ pairs). But different points may occupy the same location, as is the case in (I) and (II). The objects in set (II) and (III) are Platonic solids. All of these states are inert states. . . . .	21
4.1 Independent components in $\eta_{ijkl}$ . . . . .	83
4.2 Independent elements contributed by each representation . . . . .	86

## List of Figures

Figure	Page
2.1 Ferromagnetic order $\Phi^{(1)}$ represented the Majorana pair $[\hat{\mathbf{n}}] \equiv (\hat{\mathbf{n}}, -\hat{\mathbf{n}})$ . $[\hat{\mathbf{n}}]$ and $[-\hat{\mathbf{n}}]$ are distinct. . . . .	15
2.2 Uniaxial nematic state $\Phi^{(2)}$ represented by two identical Majorana pairs: It has the symmetry of a rod. $[\hat{\mathbf{n}}][\hat{\mathbf{n}}]$ and $[-\hat{\mathbf{n}}][-\hat{\mathbf{n}}]$ are identical. . . . .	16
2.3 Biaxial nematic state $\Phi^{(2)}$ with two distinct Majorana pairs: The quantum state is invariant under $\pi$ rotation about $\hat{\mathbf{n}} \times \hat{\mathbf{m}}$ , $\hat{\mathbf{n}} + \hat{\mathbf{m}}$ , $\hat{\mathbf{n}} - \hat{\mathbf{m}}$ . It has the symmetry of a brick with different edge lengths. . . . .	16
2.4 A fermionic system with spin- $f$ can possess structures represented by Platonic solids (octahedron, cube, icosahedron and dodecahedron respectively) consisting up to $4f$ vertices. The high-spin analogue of spin texture as in spin-half cases will be made of polygons with different orientations. . . . .	18
2.5 The numerals (1, 2, ..7) denote the spin order ( $\Phi^{(1)}, \Phi^{(2)}, \dots, \Phi^{(7)}$ ) of a spin $f = 7/2$ Fermi gas along the loop $C$ in real space. The loop is stretched out into a straight line along $x$ with end point ( $A$ ) identified. Here, $\lambda^{(7)} = 0$ , $\Phi^{(3)}$ , $\Phi^{(4)}$ , $\Phi^{(6)}$ form an octahedron, a cubic, and an icosahedron. $\Phi^{(5)}$ is a polyhedron with 5 vertices forming a pentagon. The texture of $\Phi_M^{(2)}(x)$ depicted implies a line defect inside loop $C$ , whereas the texture of $\Phi_M^{(1)}(x)$ is defect free. Our model calculations for spin $f = 21/2$ Fermi gas reveal Platonic solid configurations like (c), (d), (f) and dodecahedron (g) in certain parameter regimes. . . . .	19
2.6 The transition temperature for spin order $ \Phi^{(L)}\rangle$ for $L = 1, 2, 6, 3, 5, 4, 7$ , (from bottom to top), for a spin $f = 21/2$ Fermi gas. . . . .	28

3.1	Magnetic trap as a simple example of trapping potential. <b>Left:</b> In the atomic scale, energy levels are shifted due to the magnetic field. And the magnitude of shift is proportional to the strength of the field. For states $m = 1, 2$ shown schematically here, the energy is lower for weaker $B$ , and they are called “low-field-seeking” states. <b>Right:</b> The field changes in scales much larger than the atomic size, and the atom adiabatically stays in the same level with negligible transition amplitudes to other $m$ -states. Then the energy shift $\propto  B $ , and functions like a potential. . . . .	46
3.2	The blue-detuned ( $\omega > \omega_{mn}$ ) and red-detuned ( $\omega < \omega_{mn}$ ) Gaussian laser beams, and the effective potentials they produce respectively. Here $\omega$ is the frequency of the laser, and $\omega_{mn} = \omega_m - \omega_n$ is the atomic level spacing between $ m\rangle$ and $ n\rangle$ that is closest to resonance with the laser frequency. . .	47
3.3	Directions of local magnetic fields . . . . .	52
3.4	The (repulsive) blue-detuned later beam penetrates through the center of a (attractive) red-detuned laser, and the BEC is confined in the cylindrical surface. . . . .	55
3.5	The blue and red dotted lines represent the attractive and the repulsive potential due to the red-detuned and blue-detuned lasers. The green curve is the combined potential, with a minimum at $R$ . For sufficiently large $R$ and for weak harmonic confinement along $z$ , the quantum gas will form a quasi-2D cylindrical layer with thickness $\sigma \ll R$ , shown in green. . . . .	56
3.6	Figure (a) and (b) are velocity profiles for the $A$ and $B$ vortex respectively. The velocity of the $A$ (or $B$ ) vortex reaches a constant above (below) the vortex core and vanishes below (above) it over a distance of $R$ . Figure (c) shows the velocity profile of a necklace of six alternating $AB$ vortices. It is equivalent to the velocity profile of two counter circulating superfluid rings. . . . .	62
3.7	For $S \leq 4$ , the ground state contains no vortex. Within $S = 5, 6, 7, 8$ , the vortices aligned in one row at $z_i = 0$ with the pattern A-B-A-B. For $S \geq 9$ , the vortices array splits into two rows centering at $z_i = \pm Z$ , with all A vortices aligned in one row and all B vortices in another. . . . .	65
3.8	The time-of-flight image of the vortex row in figure 2(c), taken at the time $t$ such that $x_o/R = \sqrt{\hbar t/m}/R = 7$ on the $x$ - $y$ plane at $z = 0$ . Length is measured in units of $R$ . The $2n$ -fold symmetry of the image reflects the number of vortices in the vortex row. . . . .	66

3.9	The equal-potential line of blue-detuned and red-detuned lasers in the $x$ - $z$ plane for (i) cylindrical surfaces, (ii) spherical surfaces. The two schemes differ in the Gaussian width of the blue-detuned laser along $z$ -direction, which can be tuned by changing the focal length of the convex lens for the blue laser. . . . .	68
3.10	Toroidal surface produced by a attractive ring-shaped potential superposed with a repulsive ring-shaped potential. . . . .	69
3.11	Two ways to produce ring-shape potentials. (i) The ring-shape trapping potential used in the experiment c.f. [1] (this figure is taken from the reference). It is produced by superposing red and blue detuned lasers similar to the scheme for cylindrical trap in Fig. 3.9 (i). (ii) Intensity of Laguerre-Gaussian beam in $x$ - $y$ plane for modes $(l, p)$ . . . . .	71
3.12	Quadrupolar field in the $x$ - $z$ plane. . . . .	73
4.1	Distortion of unit parallelogram. The volume is held fixed. . . . .	89

## Chapter 1: GENERAL INTRODUCTION

The past two decades have witnessed the blossom of cold atom researches. Since the production of Bose-Einstein condensate in 1995 [2] — 70 years after its prediction by Einstein — a sequence of novel systems have been realized in cold atom laboratories. For instance, the crossover from weakly interacting Bardeen-Cooper-Schrieffer (BCS) pairing of fermions to the Bose-Einstein condensation (BEC) of tightly bound molecules was observed in 2004 [3–5]. It bridges two fundamental statistics, the bosonic and fermionic ones, and shows that they are two limits in a smooth crossover when one tunes the interaction in a system. Optical lattices for atoms [6, 7], which resembles the lattice potentials for electrons in solids, allows for simulation and engineering of a wide range of crystal structures in a well-controlled and tunable way. In the past few years, there has been another wave of research on topological insulating phases of matter in cold atom systems. The unique character of cold atom systems enables the engineering of a wide range of topological systems in a clean way, and also allows for the measurement of quantities that are hard to access in solid state systems, such as the Berry curvature with momentum resolution in the Brillouin zone [8, 9].

Such developments benefit from the high tunability of cold atom experiments. For instance, as composite particles, atoms interact with each other through multi-channel scattering, and such scattering will depend on the atomic levels. By applying magnetic fields,



the atomic levels are changed due to Zeeman effects, and the interaction strength are correspondingly changed. Such an idea have led to the development of “Feshbach resonance” that allows one to smoothly tune the interactions by changing magnetic fields, and therefore to study the BCS-BEC crossover. Besides the atom-atom interactions, the atom-laser interactions are also heavily exploited to engineer different systems. For example, optical lattices are produced by the interference pattern of laser beams; therefore, by changing the wavelength and intersection angles of laser beams, lattices of different geometries can be obtained (i.e. square lattice [6, 7], triangular lattice [10], honeycomb lattice [11, 12], a continuous crossover from triangular to honeycomb lattice [13], and kagome lattice [14]). Also, through a 2-photon absorption-emission process (Raman process), the phases of hopping constants can be tuned [15–17], and therefore allowing for engineering of topological bands. Exploiting the manipulability of cold atom experiments to engineer and investigate new physical systems have been fruitful in the past, and have propelled this thesis to further investigate two topics: the high spin physics for fermions, and the effects of non-trivial background manifolds on quantum systems living in it. More extensive introductions will be provided in following chapters regarding each topic, while we outline the topic for each chapter below, and briefly relate them to the current trend of research in the fields.

Very soon after the advent of optical trap, it was realized that without the freezing of spin degree of freedom by magnetic field, the spin interactions will play a significant role in determining the ground state structures [18, 19]. A large amount of theories and experiments have been done since 1998 regarding BEC with large spin (dubbed “spinor condensate”), where rich physics of topological defects as well as dynamical phenomena emerge along with BEC of different spins and interactions. (For reviews, see [20, 21]). In comparison, due to the experimental difficulties in obtaining fermionic superfluids of large spin

characters [22], large spin fermions have not received as much attention as their bosonic counterparts in the past. However, in recent years, there has been an emergence of interest in large spin fermionic systems regarding their spin structures [23] and dynamics [24,25] in normal (non-superfluid) state. It was found that although a long-range ordering is absent, the fermionic systems exhibits collective behaviors of large spin characters due to spin interactions. More recently, a class of “SU(N)” fermionic atoms, such as ytterbium [26] and strontium [27], have been successfully trapped and cooled in laboratories. These elements feature an interaction of high symmetry, so each spin component is completely indistinguishable from the other, leading to an SU(N) symmetry of the system. Such experimental successes have propelled a wave of interests in studying fermionic systems in the normal states regarding their spin structures and spin dynamics. Most of the current theoretical works concern systems of a specific spin [28–33]. Therefore, both out of theoretical completeness and the need for guiding future experiments using other elements, it is desirable to provide a road-map for the properties of high spin fermions of arbitrary spin. Due to such considerations, we discuss in Chapter 2 a general scheme to analyse fermionic systems with arbitrary spin, focusing on their local spin structures.

Chapter 3 and 4 are devoted to a separate topic, which is the quantum systems on non-trivial manifolds. The research on the effects of background manifold has a long-standing history in physics, most well-known in the study of general relativity and quantum gravity. For quantum fluids, such research can be dated back to the study of topological defects in  $^3\text{He}$  and  $^4\text{He}$  in 1970s, where the surface of the container for liquid helium could function as a curved two-dimensional surface [34, 35]. More recently, it was found that local Gaussian curvatures could lead to intriguing physical phenomena in a system. For instance,

in thin films for biological systems, there has been extensive study of vortices experiencing effective force induced by the Gaussian curvature (for a review, see [36]). Also, in graphene, it was found that straining the system would lead to effective gauge fields in the system [37]. Theoretically, an intriguing study around 1990 showed that the topological order of a quantum system can be introduced when the system is placed on manifolds of high genus [38–40]. The resulting concept of the “Hall viscosity” was observed in photonic system in 2015 [41]. Such trend of research has propel the study in Chapter 3 of ultracold quantum gases confined in curved surfaces, and in Chapter 4 of revealing the signature of Hall viscosity in density response signatures.

## Chapter 2: LOCAL SPIN ORDER FOR LARGE SPIN FERMION SYSTEMS

### 2.1 Introduction

Prior to the laboratory realization of Bose-Einstein condensates [2], the only quantum liquids realized in materials are the electron liquids in solids, and the low temperature phases of liquid  $^4\text{He}$  and  $^3\text{He}$ . All these systems are made up of spin-1/2 fermions (like electrons and  $^3\text{He}$  atoms), or spin-0 scalar bosons ( $^4\text{He}$  atoms). Bosonic excitations mediating the interactions could have slightly higher spins, such as the spin-1 photons mediating electromagnetic interactions, and the spin-2 gravitons that conducts gravitational force. From the limited pool of conventional examples, people have already felt the profound influence of having different spins for the particles in a system. Besides distinguishing statistics for bosonic and fermionic systems, having larger spin not only makes quantitative but also qualitative difference. A simple example is the cosmic “B-mode” in the cosmic microwave background. As a spin-2 object, gravitons are capable of inducing a unique tensorial perturbation – called “B-mode” – to the cosmic microwave background (CMB). It differs qualitatively from other perturbations induced by lower spin objects, such as spin-1 bosonic photons or spin-1/2 fermions, and consists of a fingerprint of gravitational effects on the CMB. Clearly, a whole host of new physics is pending discovery if a system made of higher spins are realized, especially in a controllable way.

Recent advances in cooling atomic gases to quantum degeneracy have created an exciting opportunity to study the high spin quantum fluids. Here by “spin”, it refers to the “hyperfine spin”

$$\mathbf{F} = \mathbf{L} + \mathbf{S} + \mathbf{I}, \quad (2.1)$$

that is a sum of electronic angular momentum  $\mathbf{L}$  and spin  $\mathbf{S}$ , as well as nuclear spins  $\mathbf{I}$  in an atom. The spin degree of freedom is described by  $|fm\rangle$ , an eigenstate of the spin operators ( $\mathbf{F}^2, F_z$ ). In weak magnetic fields where the Zeeman effect is small, the ground state consists of almost degenerate states of fixed  $f$  and  $m = -f, -f + 1, \dots, f$ . Up to date, the spins of atomic bosons trapped in experiments can range from  $f = 1, 2$  ( $^{87}\text{Rb}$  bosons) to  $f = 8$  ( $^{162}\text{Dy}$  bosons) [42], and those of fermions can be as high as  $f = 21/2$  ( $^{161}\text{Dy}$ ) [43]. Several examples of experimentally realized large spin systems are provided in Table 2.1. (One can also check [44] for an updated list of global cold atom experimental groups and the species of atoms they use).

Table 2.1: Examples of bosonic atoms and their hyperfine spins

Element	Spin- $f$	Group
$^7\text{Li}$	1, 2	Many
$^{23}\text{Na}$	1, 2	Many
$^{41}\text{K}$	1	Many
$^{87}\text{Rb}, ^{85}\text{Rb}$	1, 2	Many
$^{52}\text{Cr}$	3	Tilman Pfau, Stuttgart [45]
$^{168}\text{Er}$	6	R. Grimm, Innsbruck, Austria [46]
$^{164}\text{Dy}$	8	B. Lev, Stanford [47]

For Bose condensation and fermion pairing, there have been theoretical generalizations to high spin particles [18] [22] [19]. While there are many experiments on large spin Bose

Table 2.2: Examples of fermionic atoms and their hyperfine spins

Element	Spin- $f$	Group
$^{132}\text{Cs}$	3/2 respectively	Many
$^{134}\text{Cs}$		
$^{136}\text{Cs}$		
$^{40}\text{K}$	9/2	Many
$^{87}\text{Sr}$	9/2	J. Ye, JILA, Colorado [27]
$^{173}\text{Yb}$	5/2	L. Fallani, Florence [26]
$^{161}\text{Dy}$	21/2	B. Lev, Stanford [48]

condensates (or spinor condensates), experiments on large spin fermions are still at their infancy. At present, there is no realization of the superfluid phases of large spin fermions because of their very low transition temperatures. On the other hand, scatterings in different angular momentum channel and dipolar effects can lead to non-trivial spin structures in the normal state, which can be realized at higher temperatures. For instance, they are revealed by the spin dynamics of  $^{40}\text{K}$  fermions in the presence [24] or absence [25] of optical lattices, as well as by the formation of the spatial spin structure (spin wave) [23]. Theoretically, the possibility of rich spin structures for high spin fermions has already been illustrated in the cases of spin- $\frac{3}{2}$  fermions [28] [29], and alkali earth fermions with  $\text{SU}(N)$  symmetry [49]. The case of spin-3/2 fermions is very illuminating. By simply changing the spin value from 1/2 to 3/2, the system immediately gains a rich  $\text{SO}(5)$  symmetry. Such experimental and theoretical progresses have motivated the investigation in this thesis on the spin ordering of large spin fermionic systems, in the absence of superfluid orders.

In the following, we shall discuss the spin structure of spin- $f$  fermions in the normal state by analyzing their single particle density matrices. We shall show that these density matrices can be decomposed into different angular momentum components,  $L = 0, 1, \dots, 2f$

made up of a particle and a hole. We then show that each  $L$ -component can be represented by  $L$  pairs of antipodal points (or Majorana points) on a sphere. From the single particle density matrix, one can see that the  $L = 0$  component is the average density, and the  $L > 1$  components describe the spin structure of the system. The entire spin structure is then specified by a sequence of  $2f$  spheres with  $1, 2, \dots, 2f$  pairs of antipodal Majorana points respectively. To illustrate the special properties of these spin structures, we shall study the class of inert states [50] which are robust against perturbations. We show that many of these inert states have the symmetry of Platonic solids and will have non-abelian line defects. Furthermore, we shall perform mean field calculations to demonstrate the emergence of these inert states.

## 2.2 Symmetry Classifications

### 2.2.1 Bosonic Spinor Condensate and Fermionic Pairing

Before discussing local spin ordering, we review basic concepts about rotations in quantum systems. Also, we make some connections to previous works on the Bose-Einstein condensates of large spin boson, as well as pairing of large spin fermions.

Let  $\hat{\psi}_m(\mathbf{r})$  denote the field operator that destroys a particle with spin component  $m$ . Under rotation, the field operator  $\hat{\psi}_m(\mathbf{r})$  transforms as

$$\hat{\psi}_m \rightarrow D_{mm'}^{(f)}(\boldsymbol{\theta}) \hat{\psi}_{m'}, \quad (2.2)$$

where the rotation matrix reads

$$D_{mm'}^{(f)} = \langle fm | e^{-i\mathbf{F}\cdot\boldsymbol{\theta}} | fm' \rangle, \quad (2.3)$$

with  $\mathbf{F}$  the spin operator satisfying

$$[F_\mu, F_\nu] = i\epsilon_{\mu\nu\rho} F_\rho, \quad (2.4)$$

and  $|fm\rangle$ 's are the eigenvectors of spin operators  $(\mathbf{F}^2, F_z)$ . For spin- $f$  bosons, its condensate (known as spinor condensates) is a  $(2f + 1)$  component vector [18, 19],

$$\Psi_m(\mathbf{r}) = \langle \hat{\psi}_m(\mathbf{r}) \rangle, \quad m = f, f - 1, \dots, -f. \quad (2.5)$$

Then it is clear that the order parameter also transforms as a vector

$$\Psi_m \rightarrow \sum_{m'} D_{mm'}^{(f)} \Psi_{m'}. \quad (2.6)$$

For fermion superfluids, we can decompose the pairing order parameter

$$\Psi_{mn}(\mathbf{r}) = \langle \hat{\psi}_m(\mathbf{r}) \hat{\psi}_n(\mathbf{r}) \rangle, \quad m, n = f, f - 1, \dots, -f \quad (2.7)$$

into sectors of total angular momentum  $|FM\rangle$ ,

$$\left( \Delta_M^{(F)} \right)_{mn}(\mathbf{r}) = \sum_{FM} \langle FM | fm, fn \rangle \Psi_{mn}(\mathbf{r}), \quad (2.8)$$

where  $\langle FM | fm_1, fm_2 \rangle$  is the Clebsch-Gordon coefficients [51] for the addition of angular momentums. Then  $\Delta_M^{(F)}$  also transforms under rotation like a spin- $F$  spinor condensate [22],

$$\Delta_M^{(F)} \rightarrow D_{MM'}^{(F)} \Delta_{M'}^{(F)}. \quad (2.9)$$

Much of the symmetry properties in the spinor condensates and fermion pairing systems have been studied in the past decade [52].

### 2.2.2 Local Spin Ordering

Here we focus on the local spin order of a Fermi gas, which is contained in the single particle density matrix  $\rho_{m_1 m_2} = \langle \hat{\rho}_{m_1 m_2} \rangle$ ,

$$\rho_{m_1 m_2}(\mathbf{r}) = \langle \hat{\psi}_{m_2}^\dagger(\mathbf{r}) \hat{\psi}_{m_1}(\mathbf{r}) \rangle. \quad (2.10)$$



We clarify that by ‘‘local’’ order it means we are not considering correlations between different points, i.e.  $\langle \hat{\psi}(\mathbf{r})^\dagger \hat{\psi}(\mathbf{r}') \rangle$ . However, the local order  $\rho(\mathbf{r})$  itself can be non-uniform in space, for instance in the presence of spin textures or spin density waves. We will return to this point later when discussing topological defects. To lighten notations, we shall now temporarily suppress the spatial coordinate.

Under a spin rotation  $\boldsymbol{\theta}$ , the field operator rotates as in Equation (2.2), so the density matrix transforms as

$$\rho_{m_1 m_2} \rightarrow D_{m_1 m_3}^{(f)}(\boldsymbol{\theta}) \rho_{m_3 m_4} D_{m_4 m_2}^{(f)\dagger}(\boldsymbol{\theta}), \quad (2.11)$$

where repeated indices are summed over. Here we employ the rotation matrix (2.3) with the hermitian conjugate  $D_{mm'}^{(f)\dagger}(\boldsymbol{\theta}) = \langle fm|e^{i\boldsymbol{\theta}\cdot\mathbf{F}}|fm'\rangle$ .  $\mathbf{F}$  is the spin operator for spin- $f$  particles and  $|fm\rangle$  is the eigenstate of  $(\mathbf{F}^2, F_z)$ .

To sort out the spin structure of  $\rho_{m_1 m_2}$ , we decompose it in terms of tensor operators of different total angular momenta (made up of a particle-hole pair). This is achieved by introducing a  $(2f + 1) \times (2f + 1)$  matrix,

$$\left(Y_M^{(L)}\right)_{m_1 m_2} \equiv \sqrt{\frac{2L + 1}{2f + 1}} \langle fm_1 | LM; fm_2 \rangle, \quad (2.12)$$

where  $\langle fm_1 | LM; fm_2 \rangle$  is the Clebsch-Gordon coefficient. It has the important property that it transforms under rotation as

$$D_{m_1 m_2}^{(f)}(\boldsymbol{\theta}) \left(Y_M^{(L)}\right)_{m_2 m_3} D_{m_3 m_4}^{(f)\dagger}(\boldsymbol{\theta}) = \sum_{M'} \left(Y_{M'}^{(L)}\right)_{m_1 m_4} D_{M'M}^{(L)}(\boldsymbol{\theta}). \quad (2.13)$$

Thus,  $\left(Y_M^{(L)}\right)_{m_1, m_2}$  is a tensor operator [53] (with angular momentum  $L$ ) in the spin- $f$  space.

We can then expand  $\rho_{m_1 m_2}$  as

$$\rho_{m_1 m_2} = \sum_{L=0}^{2f} \sum_{M=-L}^L \Phi_M^{(L)} \left(Y_M^{(L)}\right)_{m_1 m_2}. \quad (2.14)$$

To simplify notation, we will sometimes omit  $(m_1 m_2)$  for  $(Y_M^{(L)})_{m_1 m_2}$  and  $\rho_{m_1 m_2}$ , and treat these objects as matrices  $Y_M^{(L)}$  and  $\rho$  with  $m_1, m_2$  being regarded as indices of the matrix. Since the Clebsch-Gordon coefficients are real numbers, so is  $(Y_M^{(L)})_{m_1 m_2}$ . That means  $Y_M^{(L)\dagger} = Y_M^{(L)T}$ , where  $\dagger$  and  $T$  means hermitian conjugate and transpose of the matrix. Since the Clebsch-Gordon coefficients satisfy [53]

$$Y_M^{(L)\dagger} = (-1)^M Y_{-M}^{(L)}, \quad \text{Tr} Y_M^{(L)} Y_{M'}^{(L)\dagger} = \delta_{LL'} \delta_{MM'}. \quad (2.15)$$

we have

$$\Phi_M^{(L)} = \text{Tr}(\rho Y_M^{(L)\dagger}). \quad (2.16)$$

From the rotational properties in Eqn (2.11) and (2.13), it is easy to see that the vector

$$\Phi^{(L)} \equiv (\Phi_{-L}^{(L)}, \dots, \Phi_L^{(L)})^T \quad (2.17)$$

transforms as a spin- $L$  vector in spin space,

$$\Phi_M^{(L)} \rightarrow \Phi_M'^{(L)} = \sum_{M'} D_{MM'}^{(L)} \Phi_{M'}^{(L)}. \quad (2.18)$$

Another convenient way to represent this transformation property is to regard  $\Phi_M^{(L)}$ 's as the expansion coefficients of a abstract spin state  $|\Phi^{(L)}\rangle$  in the angular momentum basis  $|L, M\rangle$ ,

$$|\Phi^{(L)}\rangle = \sum_{M=-L}^L \Phi_M^{(L)} |LM\rangle. \quad (2.19)$$

The rotation property of  $|\Phi^{(L)}\rangle$  immediately gives Eqn.(2.18). Note that not all  $\Phi_M^{(L)}$  in  $|\Phi^{(L)}\rangle$  are independent. The fact that  $\rho$  is hermitian implies that

$$\Phi_M^{(L)*} = (-1)^M \Phi_{-M}^{(L)}. \quad (2.20)$$

This means  $\Phi^{(L)}$  is specified by  $2L + 1$  independent *real* variables.

To connect with current literatures, it is worth mentioning an equivalent decomposition [22–25]. That will employ the tensor operator  $\tilde{Y}_M^{(L)}(\mathbf{F})$  satisfying the similar transform property (2.13), where  $\mathbf{F}$  is spin operator. The way to construct it is to first multiply the standard spherical harmonic function with radial coordinate  $r$ :  $r^L \tilde{Y}_M^{(L)}(\theta, \varphi)$ , and then express it in terms of Cartesian coordinates  $x, y, z$ . Finally, we replace  $x, y, z$  with spin operators  $F_x, F_y, F_z$  respectively. Since the solution to (2.13) is unique, the two objects  $Y_M^{(L)}$  and  $\tilde{Y}_M^{(L)}$  must be equivalent. Indeed, we show in the appendix Sec.2.7.3 the specific proportionality relation

$$\left[\tilde{Y}_M^{(L)}\right]_{\mu\nu}^{(f)} = (-1)^L \sqrt{\frac{(2f+L+1)!}{4\pi 2^{2L}(2f-L)!}} \left(Y_M^{(L)}\right)_{\mu\nu}^{(f)}. \quad (2.21)$$

We adopt  $Y_M^{(L)}$  in Equation (2.12) here for the convenience of later analysis.

Finally, taking the trace of the expansion in Eqn. (2.14), we have

$$\Phi^{(0)} = n/(2f+1). \quad (2.22)$$

where we have made use of the fact that

$$\text{Tr} Y_M^{(L)} = 0, \quad \text{for } L \geq 1. \quad (2.23)$$

To show Eq.(2.23), we take the Trace of Eqn.(2.13). This gives  $\text{Tr} Y_M^{(L)} = \text{Tr} Y_{M'}^{(L)} D_{M'M}^{(L)}(\boldsymbol{\theta})$  for all  $L \geq 1$  and all  $\boldsymbol{\theta}$ , which can only be satisfied if Eqn.(2.23) is valid. Because of Eqn.(2.22), one sees that the non-trivial spin structures are given by the traceless part of  $\rho$ ,

$$\tilde{\rho}_{mn} \equiv \rho_{mn} - \frac{n}{2f+1} \delta_{mn}. \quad (2.24)$$

Although  $\Phi^{(L)}$  is formally similar to a spin- $L$  spinor condensate, it has very different meaning. From Wigner-Eckart theorem (or from the relation (2.21), we note that  $Y_M^{(L)}$  is proportional to a product of  $L$  spin operators  $\mathbf{F}$  in spin- $f$  space. Thus,  $\Phi^{(1)}$  and  $\Phi^{(2)}$  are proportional to a single and to a product of two  $\mathbf{F}$  operators respectively, and thus represent

ferromagnetic and nematic order respectively in spin- $f$  space. The vectors  $\Phi^{(L)}$  for  $L \geq 1$  will be referred to as the  $L$ -th sector of spin order. All  $L = 1, 2, \dots, 2f$  sectors are contained in the traceless part of  $\tilde{\rho}$ .

### 2.2.3 Majorana Representation on a Bloch Sphere

To gain further insight, we express each sector of ordering  $|\Phi^{(L)}\rangle$  in Majorana representation as a set of  $2L$  points (referred to as Majorana points) on the unit sphere  $S_2$  [54–60]. To accomplish it, we use the Schwinger boson representation of angular momentum states,

$$|LM\rangle = \frac{a^{\dagger L+M} b^{\dagger L-M}}{\sqrt{(L+M)!(L-M)!}}|0\rangle, \quad (2.25)$$

where  $a$  and  $b$  are boson operators, and  $(a, b)^T$  transform as a spin-1/2 spinor [61]. A general state of the form Eqn.(2.19) can then be factorized as

$$|\Phi^{(L)}\rangle = \lambda^{(L)} \prod_{i=1}^{2L} (u_i^{(L)} a^\dagger + v_i^{(L)} b^\dagger) |0\rangle, \quad (2.26)$$

where  $\lambda^{(L)}$  is a constant, and  $\zeta_i^{(L)} \equiv (u_i^{(L)}, v_i^{(L)})^T$  is a normalized spinor

$$|u_i^{(L)}|^2 + |v_i^{(L)}|^2 = 1. \quad (2.27)$$

Equation (2.26) follows from the fundamental theorem of algebra which implies a homogenous polynomial  $\mathcal{P}(x, y) = \sum_{M=-L}^L \alpha_M x^{L+M} y^{L-M}$  can be factorized to  $2L$  linear terms  $\mathcal{P}(x, y) = \lambda \prod_{i=1}^{2L} (u_i x + v_i y)$ .

To simplify notations, we shall suppress the superscript  $^{(L)}$  when we discuss a specific  $L$  component. It will be reinstated when needed. Using the standard representation for a spinor

$$\zeta = (u, v)^T \equiv \left( \cos \frac{\theta}{2} e^{-i\phi/2}, \sin \frac{\theta}{2} e^{i\phi/2} \right)^T e^{i\chi/2}, \quad (2.28)$$

we have

$$\zeta^\dagger \vec{\sigma} \zeta = \hat{\mathbf{n}} = \cos\theta \hat{\mathbf{z}} + \sin\theta (\cos\phi \hat{\mathbf{x}} + \sin\phi \hat{\mathbf{y}}). \quad (2.29)$$

Hence each  $\zeta_i$  in Eqn.(2.26) can be represented as a point on the unit sphere  $S_2$  in the direction  $\hat{\mathbf{n}}_i$  with polar angle  $(\theta_i, \phi_i)$ . Note that all the phases  $\chi_i$  absorbed into the constant  $\lambda$ .

However, the  $\hat{\mathbf{n}}_i$  are not independent, as Eqn.(2.20) implies that Eqn.(2.26) can be rewritten as

$$\begin{aligned} |\Phi^{(L)}\rangle &= \sum_{M=-L}^L \frac{\Phi_M^{(L)*}}{\sqrt{(L+M)!(L-M)!}} b^{\dagger L+M} (-a^\dagger)^{L-M} |0\rangle \\ &= \lambda^* \prod_{i=1}^{2L} (u_i^* b^\dagger - v_i^* a^\dagger) |0\rangle, \end{aligned} \quad (2.30)$$

where we have suppressed the superscript  $(L)$ . Eqn.(2.30) shows that the spinors  $\zeta_i$  in Eqn.(2.26) must be accompanied by its time reversed partner  $-i\sigma_2 \zeta_i^* = (-v_i^*, u_i^*)$ . Therefore, the  $2L$  vectors  $\hat{\mathbf{n}}_i$  must appear in terms of antipodal pairs  $(\hat{\mathbf{n}}_i, -\hat{\mathbf{n}}_i) \equiv [\hat{\mathbf{n}}_i]$ . It is then sufficient to represent each pair by only one of its members. The presence of antipodal pairs implies Eqn.(2.26) is of the form

$$\begin{aligned} |\Phi^{(L)}\rangle &= \lambda^{(L)} \prod_{i=1}^L (-u_i v_i^* a^{\dagger 2} + (|u_i|^2 - |v_i|^2) a^\dagger b^\dagger + u_i^* v_i b^{\dagger 2}) |0\rangle \\ &= \frac{\lambda^{(L)}}{2} \prod_{i=1}^L (\sin \theta_i e^{i\phi_i} b^{\dagger 2} - \sin \theta_i e^{-i\phi_i} a^{\dagger 2} + \cos_i \theta_i a^\dagger b^\dagger) |0\rangle, \end{aligned} \quad (2.31)$$

with  $\lambda^{(L)*} = \lambda^{(L)}$  because of Eqn.(2.20). The  $(2L+1)$  real variables of  $\Phi^{(L)}$  is now represented by the  $L$  unit vectors  $\hat{\mathbf{n}}_i$  and a real number  $\lambda^{(L)}$ . In equilibrium, different  $\lambda^{(L)}$ 's are correlated to minimize the energy.

In summary, we have decomposed the non-trivial traceless part of the density matrix  $\tilde{\rho}_{m_1 m_2}(\mathbf{r})$ , which represent local spin order into various spin- $L$  vectors  $\Phi^{(L)}$ , where  $L = 1, 2, \dots, 2f$ . Each  $\Phi^{(L)}$  is represented by  $L$  antipodal pairs of points on a spherical surface,

whose radius  $\lambda^{(L)}$  represents the strength of the L-sector of spin order. In the following, we discuss the properties of the local spin order in each  $L$ -sector.

### 2.3 Topological defects

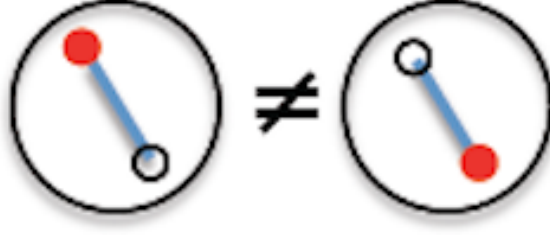


Figure 2.1: Ferromagnetic order  $\Phi^{(1)}$  represented the Majorana pair  $[\hat{\mathbf{n}}] \equiv (\hat{\mathbf{n}}, -\hat{\mathbf{n}})$ .  $[\hat{\mathbf{n}}]$  and  $[-\hat{\mathbf{n}}]$  are distinct.

For  $L = 1$ , the ferromagnetic order, there is only one pair of Majorana points  $[\hat{\mathbf{n}}]$ . (See Fig. 2.1). Since  $\hat{\mathbf{n}}$  can be in any direction, the configurational space is the unit sphere  $S^2$ . Note that  $[\hat{\mathbf{n}}]$  and  $[-\hat{\mathbf{n}}]$  are distinct because  $|\Phi^{(1)}\rangle$ :

$$|\Psi^{(1)}\rangle = \lambda \left( -\frac{1}{2} \sin\theta e^{-i\phi} a^{\dagger 2} + \cos\theta a^{\dagger} b^{\dagger} + \frac{1}{2} \sin\theta e^{i\phi} b^{\dagger 2} \right) |0\rangle \quad (2.32)$$

becomes  $-|\Phi^{(1)}\rangle$  as  $\hat{\mathbf{n}}$  changes continuously to  $-\hat{\mathbf{n}}$ . That is  $|\Phi^{(1)}\rangle \rightarrow -|\Phi^{(1)}\rangle$  as  $\theta \rightarrow \pi - \theta$ ,  $\phi \rightarrow \phi + \pi$ . Since the first homotopy group of  $S^2$  is trivial,  $(\pi_1(S_2) = 0)$ , the ferromagnetic sector ( $L = 1$ ) of spin ordering  $\{\Phi_M^{(1)}(\mathbf{r})\}$  has no topologically stable line defects [62].

For  $L = 2$ , the nematic order, there are two Majorana pairs  $[\hat{\mathbf{n}}][\hat{\mathbf{m}}]$ . If  $\hat{\mathbf{n}} = \pm\hat{\mathbf{m}}$ , the system is uniaxial nematics characterized by a single antipodal pair on the unit sphere with each pole doubly occupied. (See Fig. 2.2). Unlike  $L = 1$ , where  $[\hat{\mathbf{n}}]$  and  $[-\hat{\mathbf{n}}]$  are distinct,

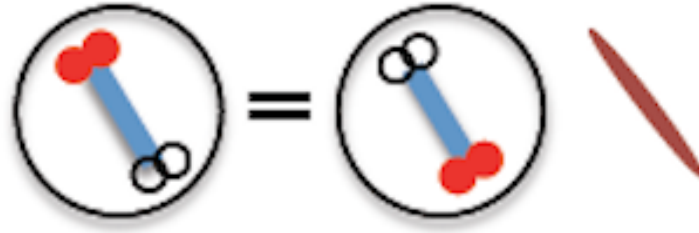


Figure 2.2: Uniaxial nematic state  $\Phi^{(2)}$  represented by two identical Majorana pairs: It has the symmetry of a rod.  $[\hat{\mathbf{n}}][\hat{\mathbf{n}}]$  and  $[-\hat{\mathbf{n}}][-\hat{\mathbf{n}}]$  are identical.

the states  $[\hat{\mathbf{n}}][\hat{\mathbf{n}}]$  and  $[-\hat{\mathbf{n}}][-\hat{\mathbf{n}}]$  are identical, as they correspond to the same state

$$|\Phi_{un}^{(2)}\rangle = \lambda(ua^\dagger + vb^\dagger)^2(-v^*a^\dagger + u^*b^\dagger)^2|0\rangle. \quad (2.33)$$

(Note that  $([\hat{\mathbf{n}}][-\hat{\mathbf{n}}] = -[\hat{\mathbf{n}}][\hat{\mathbf{n}}])$ . The configuration space is therefore  $S^2$  with antipodal points identified, which is the projected space  $P_2$ . Since  $\pi_1(P_2) = Z_2$ , there is only one type of nontrivial line defect.

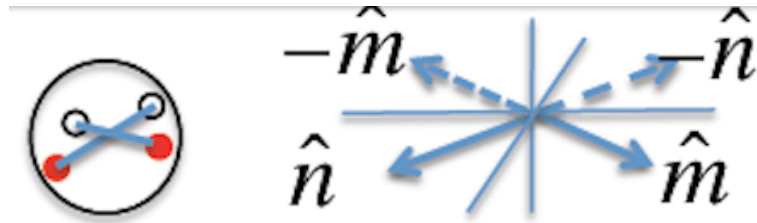


Figure 2.3: Biaxial nematic state  $\Phi^{(2)}$  with two distinct Majorana pairs: The quantum state is invariant under  $\pi$  rotation about  $\hat{\mathbf{n}} \times \hat{\mathbf{m}}$ ,  $\hat{\mathbf{n}} + \hat{\mathbf{m}}$ ,  $\hat{\mathbf{n}} - \hat{\mathbf{m}}$ . It has the symmetry of a brick with different edge lengths.

If  $\hat{\mathbf{n}} \neq \pm\hat{\mathbf{m}}$ , it is straightforward to show that  $|\Phi^{(2)}\rangle$  is unchanged only under a  $\pi$  rotation along the orthogonal axes  $\hat{\mathbf{n}} \times \hat{\mathbf{m}}$ ,  $\hat{\mathbf{n}} + \hat{\mathbf{m}}$ , and  $\hat{\mathbf{n}} - \hat{\mathbf{m}}$ . The system has two distinct antipodal pairs,  $[\hat{\mathbf{n}}]$  and  $[\hat{\mathbf{m}}]$ . Choosing the  $z$ -axis along  $\hat{\mathbf{n}} \times \hat{\mathbf{m}}$ , the polar angles of  $\hat{\mathbf{n}}$  and  $\hat{\mathbf{m}}$  are  $(\pi/2, \phi_1)$  and  $(\pi/2, \phi_2)$  respectively. The corresponding quantum state is

$$|\Phi_{bi\perp}^{(2)}\rangle = \frac{\lambda}{4}(-e^{-i\phi_1}a^\dagger{}^2 + e^{i\phi_1}b^\dagger{}^2)(-e^{-i\phi_2}a^\dagger{}^2 + e^{i\phi_2}b^\dagger{}^2)|0\rangle, \quad (2.34)$$

which is unchanged under a  $\pi$ -rotation about  $\hat{\mathbf{z}}$  when changing  $\phi_i$  to  $\phi_i + \pi$ . Next, if we choose the  $z$ -axis along  $\hat{\mathbf{n}} + \hat{\mathbf{m}}$ , and the  $x$ -axis along  $\hat{\mathbf{n}} - \hat{\mathbf{m}}$ , the polar angles of  $\hat{\mathbf{n}}$  and  $\hat{\mathbf{m}}$  are then  $(\theta, 0)$  and  $(\theta, \pi)$  respectively. The corresponding state is

$$|\Phi_{bi\parallel}^{(2)}\rangle = \frac{\lambda}{4}(-\sin\theta[a^\dagger{}^2 + b^\dagger] + 2\cos\theta a^\dagger b^\dagger)(\sin\theta[a^\dagger{}^2 + b^\dagger] + 2\cos\theta a^\dagger b^\dagger)|0\rangle. \quad (2.35)$$

This state is also invariant under a rotation of  $\pi$  about  $\hat{\mathbf{z}}$ , which changes  $a^\dagger$  to  $-ia^\dagger$ ,  $b^\dagger$  to  $ib^\dagger$ . The system is therefore a bi-axial nematics, and has nonabelian line defects [62].

For  $L \geq 3$ , there will be more pairs of Majorana points. A simple situation is that all pairs locate at the same position, as what happens for uniaxial nematics. The discussions above show that for odd and even  $L$ , the configuration space is  $S^2$  and  $P_2$  respectively. In general, the pairs of points can distribute arbitrarily, forming the vertices of an irregular polygon, as those in Fig. 1 (e). The fact that *the Majorana points must appear in antipodal pairs forbids the polygon to have tetrahedral symmetry*, as shown in (Fig.1 (iv)). This is different from the situation in bosonic spinor condensates where tetrahedral symmetry is allowed in the case when spin  $f \geq 2$  [55].

Of particular interests are the cases when the Majorana points are distributed in high symmetry, such as the Platonic solids shown in Fig. (c) (d) (f) (g), which are cube, octahedron, icosahedron, and dodecahedron respectively. The symmetry groups of (c) and (d) is



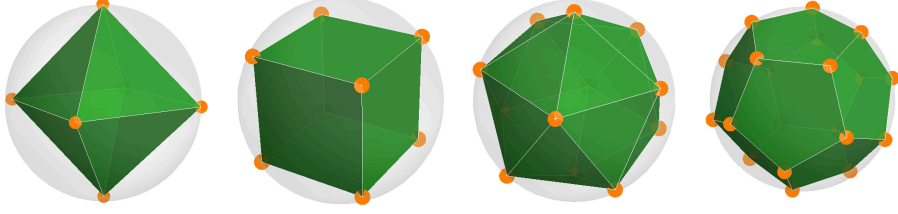


Figure 2.4: A fermionic system with spin- $f$  can possess structures represented by Platonic solids (octahedron, cube, icosahedron and dodecahedron respectively) consisting up to  $4f$  vertices. The high-spin analogue of spin texture as in spin-half cases will be made of polygons with different orientations.

the octahedral group  $O$ , and that for (f) and (g) is icosahedral group  $Y$ . These states belong to the class of “inert states” whose structures (i.e. distribution of Majorana points) are independent of interaction parameters [63]. These states, if present, must therefore occupy a finite region in parameter space, and have a good chance of being observed. We show in the next section through a mean field calculation that all these Platonic solids states can arise from spin exchange interaction [18].

As mentioned before, the spin order is specified by the set of vectors  $\{\Phi^{(L)}\}$  with  $L = 1, 2, \dots, 2f$ . In general, when dipolar interaction is taken into account, these vectors (and their corresponding Majorana points in  $S_2$ ) will vary in space, forming a spin texture in each  $L$ -sector. The general behavior of these spin textures  $\{\Phi^{(L)}(\mathbf{r})\}$  is illustrated in Figure 1 (1-7) for the case of  $f = 7/2$ . The figure displays the spin orders  $|\Phi^{(L)}(x)\rangle$  along a loop  $C$  in real space, which can be represented as a straight line along  $x$  with end points identified. The entire set of spin order  $\{\Phi^{(L)}(x), L = 1, 2, \dots, 2f\}$  is represented as an array of  $2f$  spherical surfaces with radius  $|\lambda^{(L)}(x)|$  and  $L$  pairs of antipodal Majorana points. One can recall that the spin texture in spin-1/2 systems corresponds to a rotation of a vector in space; the direction of the vector designates the local spin order  $\langle \mathbf{S} \rangle$ . In comparison, the spin textures

in higher  $L$ -sector of the spin order correspond to the rotation (or even deformation) of a polygon in space. As long as  $\lambda^{(L)}(x) \neq 0$  and different Majorana pairs do not merge as one traverses the loop  $C$ , each  $L$  sector can have its own line defects.

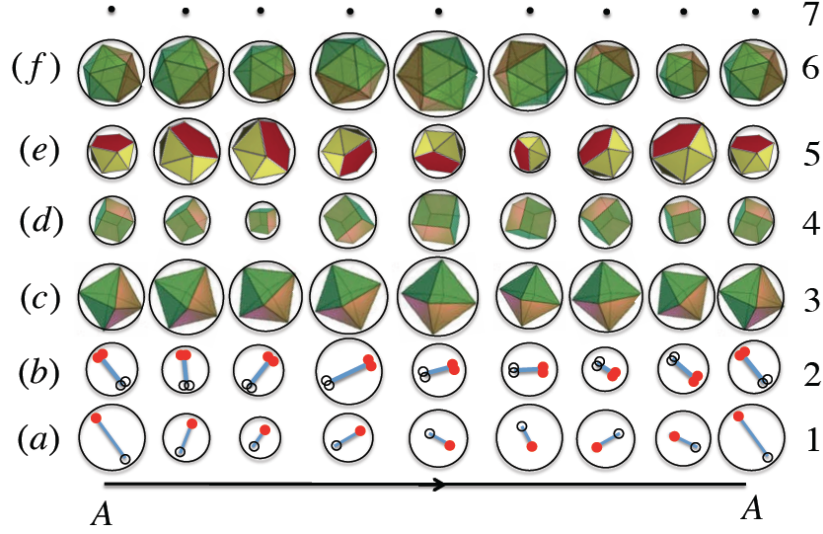


Figure 2.5: The numerals (1, 2, ..7) denote the spin order ( $\Phi^{(1)}, \Phi^{(2)}, \dots, \Phi^{(7)}$ ) of a spin  $f = 7/2$  Fermi gas along the loop  $C$  in real space. The loop is stretched out into a straight line along  $x$  with end point ( $A$ ) identified. Here,  $\lambda^{(7)} = 0$ ,  $\Phi^{(3)}, \Phi^{(4)}, \Phi^{(6)}$  form an octahedron, a cubic, and an icosahedron.  $\Phi^{(5)}$  is a polyhedron with 5 vertices forming a pentagon. The texture of  $\Phi_M^{(2)}(x)$  depicted implies a line defect inside loop  $C$ , whereas the texture of  $\Phi_M^{(1)}(x)$  is defect free. Our model calculations for spin  $f = 21/2$  Fermi gas reveal Platonic solid configurations like (c), (d), (f) and dodecahedron (g) in certain parameter regimes.

## 2.4 Energetic considerations and Platonic solid inert states

Next, we discuss how interaction effects give rise to the spin order discussed above. We shall consider a general short range spin-exchange interaction between fermions [18]. Such a description has been shown to be effective in recent experiments in  $^{40}\text{K}$  [23–25], where dipolar interactions are negligible. Many other high spin systems (i.e.  $^{161}\text{Dy}$ ) have stronger

dipolar interactions which will lead to non-uniform spin ordering. As a first step, we shall ignore dipolar interactions. In practice, dipolar interactions can be averaged out to zero through a sequence of magnetic pulses [64]. On the other hand, many competing orders may arise at low temperatures, including the superconducting ordering. Different orders would be favored in different regions in the parameter space. For instance, for spin-1/2 fermions, attractive interaction leads to superconducting phase while repulsive interaction induces magnetic ordering [65, 66]. For higher spin systems, in general, the orders may have overlap in the parameter space and different orders will compete with each other. Here we do not consider the possibility of competing phases, and discuss first the parameter regions that can give rise to spin ordering.

Finally, we emphasize that the structures discussed in previous sections do not rely on the magnetic ordering as discussed below. The emergence of magnetic ordering shown below not only leads to the existence of different  $L$  sectors, but also ensures that local spin ordering at different locations are long-range correlated, as in the magnetism of familiar spin-1/2 situation. At higher temperature when long-range magnetic ordering vanishes (like superconductivity), the higher  $L$ -sectors of spin ordering may still persists locally. The discussion of high temperature regime is left for future works, while in the following we focus on the possible magnetic states at low temperatures.

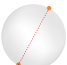



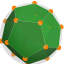
The Hamiltonian for local spin-exchange interaction is  $H = H_0 + H_1$ , where the kinetic and interaction parts are

$$H_0 = \int d^3 \mathbf{r} \sum_m \psi_m^\dagger(\mathbf{r}) \left( \frac{\hbar^2 \nabla^2}{2\tilde{m}} - \mu \right) \psi_m(\mathbf{r}), \quad (2.36)$$

$$H_1 = \int d^3 \mathbf{r} \sum_{\substack{m_1 m_2 \\ m_3 m_4}} \psi_{m_1}^\dagger(\mathbf{r}) \psi_{m_2}^\dagger(\mathbf{r}) \gamma_{m_1 m_2 m_3 m_4} \psi_{m_4}(\mathbf{r}) \psi_{m_3}(\mathbf{r}), \quad (2.37)$$

Table 2.3: Exploration of  $T = 0$  mean field phase diagram for spin  $f = 21/2$  fermion systems in the presence of spin exchange interactions.  $k_n = (6\pi^2 n)^{1/3}$ , where  $n$  is the total number of particles in the system.  $\{a_F, F = 0, 2, \dots, 2f - 1\}$  are scattering channels with total spin  $F$ . The spin orders of different sectors are represented in Majorana representation.  $|\Phi^{(L)}\rangle$  sector would contain  $2L$  points ( $L$  pairs). But different points may occupy the same location, as is the case in (I) and (II). The objects in set (II) and (III) are Platonic solids. All of these states are inert states.

Set	$k_n a_0$	$k_n a_2$	$k_n a_4$	$k_n a_6$	$k_n a_8$	$k_n a_{10}$	$k_n a_{12}$	$k_n a_{14}$	$k_n a_{16}$	$k_n a_{18}$	$k_n a_{20}$
(I)	0.1	0.3	0.4	0.45	0.5	0.5	0.45	0.45	-0.3	-0.5	-0.5
(II)	-0.1	-0.6	-0.6	0.55	0.75	0.75	0.45	-0.75	-0.8	0.8	0.8
(III)	-0.6	-0.74	0.87	0.79	0.84	-0.8	-0.83	0.82	0.82	-0.85	0.85

Set	Sectors of Spin Order
(I)	 $ \Phi^{(1,2,3,4)}\rangle$
(II)	 $ \Phi^{(4,8)}\rangle$ and  $ \Phi^{(6)}\rangle$
(III)	 $ \Phi^{(6)}\rangle$ and  $ \Phi^{(10)}\rangle$

where  $\tilde{m}$  is the fermion mass,  $\mu$  is the chemical potential, and

$$\gamma_{m_1 m_2 m_3 m_4} = \frac{1}{2} \sum_{F=0,2,\dots}^{2f-1} g_F \sum_{M_F=-F}^F \langle m_1 m_2 | F M_F \rangle \langle F M_F | m_3 m_4 \rangle. \quad (2.38)$$

Here  $\langle m_1 m_2 | F M_F \rangle$  is an abbreviation for Clebsch-Gordon coefficients

$\langle f m_1; f m_2 | F M_F \rangle$ .  $g_F \equiv 4\pi\hbar^2 a_F / \tilde{m}$  is the interaction constant in the scattering channel with total spin- $F$ , and  $a_F$  is the corresponding scattering length [67]. For half integer spin  $f$ ,  $\langle f m_1; f m_2 | F M_F \rangle = \pm \langle f m_2; f m_1 | F M_F \rangle$  for odd/even  $F$  respectively. Thus, (2.37) and Fermi statistics require  $F$  to be even integers only. That means  $\gamma_{m_1 m_2 m_3 m_4}$  is odd under the exchange  $m_1 \leftrightarrow m_2$  or  $m_3 \leftrightarrow m_4$ .

(It is useful here to summarize our notations.  $(f, m)$  are the eigenvalues of single atom spin operators  $(\mathbf{F}^2, F_z)$ .  $(F, M_F)$  is the total spin and magnetic quantum number when two

atoms scatter with each other.  $(L, M)$  introduced previously denote the particle-hole total angular momentum quantum numbers, and are the quantum numbers we use to classify spin orders in terms of different sectors  $|\Phi^{(L)}\rangle$  in (2.19). )

We shall study the *uniform* spin order using the mean field approximation. The order parameter is  $\rho_{m_1 m_2}$  defined in (2.10), and it is equal to the average

$$\rho_{m_1 m_2} = \int \frac{d^3 \mathbf{r}}{V} \rho_{m_1 m_2}(\mathbf{r}) = \frac{1}{V} \sum_{\mathbf{k}} \langle c_{\mathbf{k} m_2}^\dagger c_{\mathbf{k} m_1} \rangle, \quad (2.39)$$

where we used the Fourier transform  $\psi_m(\mathbf{r}) = \frac{1}{\sqrt{V}} \sum_{\mathbf{k}} e^{i\mathbf{k}\cdot\mathbf{r}} c_{\mathbf{k} m}$ , and  $V$  is the volume. Then the mean field Hamiltonian reads  $H_{\text{MF}} = \sum_{\mathbf{k}, m_1 m_2} c_{\mathbf{k} m_1}^\dagger \mathcal{H}_{m_1 m_2}(\mathbf{k}) c_{\mathbf{k} m_2}$ , with

$$\mathcal{H}_{m_1 m_2}(\mathbf{k}) = (\varepsilon_{\mathbf{k}} - \mu) \delta_{m_1 m_2} + 4\Gamma_{m_1 m_2}, \quad (2.40)$$

$$\Gamma_{m_1 m_2} = \sum_{m_3 m_4} \gamma_{m_1 m_3 m_2 m_4} \rho_{m_4 m_3}. \quad (2.41)$$

Here  $\varepsilon_{\mathbf{k}} = \hbar^2 k^2 / 2\tilde{m}$  is the kinetic energy. The quadratic Hamiltonian can be diagonalized in spin space through a unitary transform  $(U^\dagger \mathcal{H}(\mathbf{k}) U)_{m_1 m_2} = (\varepsilon_{\mathbf{k}} - \mu_{m_1}[\Gamma]) \delta_{m_1 m_2}$ , where  $\mu_m[\Gamma] = \mu - 4(U^\dagger \Gamma U)_{mm}$ . Then the quasi-particles  $b_{\mathbf{k} m_1} = \sum_{m_2} U_{m_1 m_2}^\dagger c_{\mathbf{k} m_2}$  are free fermions obeying  $\frac{1}{V} \sum_{\mathbf{k}} \langle b_{\mathbf{k} m_1}^\dagger b_{\mathbf{k} m_2} \rangle = n_{m_1} \delta_{m_1 m_2}$ , where  $n_{m_1} = \frac{1}{V} \sum_{\mathbf{k}} \left( e^{(\varepsilon_{\mathbf{k}} - \mu_{m_1}[\Gamma]) / k_B T} + 1 \right)^{-1}$ . With the above information, we can determine the order parameter through the consistency equation

$$\rho_{m_1 m_2} = \sum_{m_3} U_{m_1 m_3} n_{m_3} U_{m_3 m_2}^\dagger, \quad (2.42)$$

and obtain the spin vector  $\{\Phi^{(L)}\}$  using Eqn.(2.16).

We have solved the self consistency Equation (2.42) at  $T = 0$  numerically for the case of  $f = 21/2$  with some specific value of gas parameters  $\{k_n a_F\}$ 's, where

$$k_n = (6\pi^2 n)^{1/3}, \quad (2.43)$$

and  $n$  is the total number density. See Table 2.3. Since  $a_F$ 's are unknown at present, we have tried various parameter sets, labelled (I) to (III) in Table 2.3. Their mean field states are:

(I): Only  $\Phi^{(1)}, \Phi^{(2)}, \Phi^{(3)}, \Phi^{(4)}$  are nonzero. The Majorana points of each one of them collapse into a single antipodal pair like (a) and (b) in Fig. 1. The pairs of different  $L$  orient differently.

(II): Only  $\Phi^{(4)}, \Phi^{(6)}, \Phi^{(8)}$  are non-zero.  $\Phi^{(4)}$  and  $\Phi^{(8)}$  form cubes (Fig.1(d)).  $\Phi^{(6)}$  forms an octahedron (Fig.1(c)). For  $\Phi^{(8)}$  and  $\Phi^{(6)}$ , the vertices of the cube and octahedron are doubly occupied respectively.

(III): Only  $\Phi^{(6)}$  and  $\Phi^{(10)}$  are non-zero.  $\Phi^{(6)}$  forms an isocahedron (Fig.1(f)) and  $\Phi^{(10)}$  forms a dodacahedron (Fig.1(g)).

The states found in (II) and (III) are the Platonic solids. All the states in (I) to (III) are the so-called inert states as the distances between Majorana points in these states are independent of interactions. All these states are found in a region containing the parameter set in Table 2.3. There are also non-inert states in other regions of parameter space. We emphasize that the scattering lengths in Table. 2.3 satisfy  $k_n a < 1$  and are below the resonance regime, so the atom loss due to strong interaction should be small.

## 2.5 Phase Transition: Ginzburg-Landau Theory

Since there are many scattering parameters  $\{a_F, F = 0, 2, \dots, 2f\}$  for large spin systems, it is laborious to explore every corner in the phase diagram numerically. However, considerable insight can be gained by exploring the phase transition boundary using Ginzburg-Landau theory.

Near the phase boundary, the spin order  $\tilde{\rho}_{m_1 m_2}$  defined in Eqn.(2.24) is small . We can then expand the free energy in mean field approximation

$$\Omega = -\frac{1}{\beta} \ln(\text{Tr} e^{-\beta H_{\text{MF}}}) - B \quad (2.44)$$

around  $\tilde{\rho}_{m_1 m_2} = 0$ , where  $\beta = 1/k_B T$  is the inverse temperature. Here  $H_{\text{MF}} = H_{\text{MF}}^{(0)} + H_{\text{MF}}^{(1)}$ , with

$$H_{\text{MF}}^{(0)} = \sum_{\mathbf{k}m} (\epsilon_{\mathbf{k}} - \mu) c_{\mathbf{k}m}^\dagger c_{\mathbf{k}m}, \quad (2.45)$$

$$H_{\text{MF}}^{(1)} = \sum_{\mathbf{k}m_1 m_2} \tilde{\Gamma}_{m_1 m_2} c_{\mathbf{k}m_1}^\dagger c_{\mathbf{k}m_2}, \quad (2.46)$$

$$\tilde{\Gamma}_{m_1 m_2} = 4 \sum_{m_3 m_4} \gamma_{m_1 m_3 m_2 m_4} \tilde{\rho}_{m_4 m_3}, \quad (2.47)$$

and we have restored the condensate energy  $B = \langle H - H_{\text{MF}} \rangle_{\text{MF}}$  to the free energy:

$$\begin{aligned} B &= 2V \sum_{m_1 \dots m_4} \gamma_{m_1 m_2 m_3 m_4} \rho_{m_3 m_1} \rho_{m_4 m_2} \\ &= 2V \sum_{m_1 m_2} \tilde{\Gamma}_{m_1 m_2} \tilde{\rho}_{m_2 m_1} + V n^2 \sum_{F=0,2,\dots}^{2f-1} g_F \frac{2F+1}{(2f+1)^2}. \end{aligned} \quad (2.48)$$

Terms linear in  $\tilde{\rho}_{mm'}$  vanishes due to the identity

$$\langle f m_1; f m_2 | F M_F \rangle = (-1)^{f+m_2} \sqrt{\frac{2F+1}{2f+1}} \langle f(-m_2); F M_F | f m_1 \rangle \quad (2.49)$$

and the completeness relation  $1 = \sum_m |f m\rangle \langle f m|$ . Similarly, one can show that  $\tilde{\Gamma}_{m_1 m_2}$  is traceless and Hermitian.

Using the technique of linked cluster expansion [68], we have

$$\Omega = \Omega_0 - B - \frac{1}{\beta} \sum_{l=1}^{\infty} M_l, \quad \Omega_0 = -\frac{1}{\beta} \ln \text{Tr} e^{-\beta H_{\text{MF}}^{(0)}}, \quad (2.50)$$

$$M_l = \frac{(-1)^l}{l!} \int_0^\beta d\tau_1 \dots \int_0^\beta d\tau_l \langle \mathcal{T}_\tau H_{\text{MF}}^{(1)}(\tau_1) \dots H_{\text{MF}}^{(1)}(\tau_l) \rangle_c, \quad (2.51)$$

where  $H_{\text{MF}}^{(1)}(\tau) = e^{\tau H_0} V e^{-\tau H_0}$ , and “ $\langle \dots \rangle_c$ ” means connected diagrams,  $\mathcal{T}_\tau$  is the imaginary-time ordering. Evaluating (2.51) using Wick’s theorem and keeping up to second order in  $\tilde{\rho}_{m_1 m_2}$ , we have

$$\Delta\Omega = -\frac{V}{2} \left( \text{Tr} \tilde{\Gamma} \tilde{\rho} + \chi(T, \mu) \text{Tr} \tilde{\Gamma}^2 \right), \quad (2.52)$$

where we have treated  $\tilde{\Gamma}_{m_1 m_2}$  and  $\tilde{\rho}_{m_1 m_2}$  as matrices. The susceptibility function is

$$\chi(T, \mu) = \frac{1}{T} \sum_{\mathbf{k}} f_{\mathbf{k}} (1 - f_{\mathbf{k}}) = \int_0^\infty d\varepsilon D(\varepsilon) \left( -\frac{\partial f(\varepsilon)}{\partial \varepsilon} \right), \quad (2.53)$$

where  $D(\varepsilon) = 3n \sqrt{\varepsilon} / 2\varepsilon_n^{3/2}$  is the density of states,  $\varepsilon_n = \hbar^2 k_n^2 / 2\tilde{m}$ , and  $f_{\mathbf{k}} = (e^{(\varepsilon_{\mathbf{k}} - \mu)/T} + 1)^{-1}$  is the Fermi distribution function.  $\chi(T, \mu)$  is always positive and increases as temperature is lowered.

Now we express (2.52) in terms of  $\Phi_M^{(L)}$  to see the emergence of each  $L$ -sector of the spin order. Note that  $\tilde{\rho}_{m_1 m_2}$  has the same expansion as those of  $\rho_{m_1 m_2}$  in equation (2.14), except for the absence of  $L = 0$  term. Combined with (2.47), we have

$$\tilde{\Gamma}_{m_1 m_2} = - \sum_{L=1}^{2f} \sum_{M=-L}^L \Phi_M^{(L)} G_L \left( \mathcal{Y}_M^{(L)} \right)_{m_1 m_2}, \quad (2.54)$$

$$G_L = 2 \sum_{F=0,2,\dots}^{2f-1} g_F (2F+1) W(FL). \quad (2.55)$$

Here we used the identity

$$\begin{aligned} & \sum_{m_1 m_2 M_F} \langle FM_F | f m_1; f m_a \rangle \langle f m_1 | LM; f m_2 \rangle \langle f m_2; f m_b | FM_F \rangle \\ &= \langle s m_b | LM; s m_a \rangle (-1)^{2f-F} (2F+1) W(FL), \end{aligned} \quad (2.56)$$

which is derived from the definition of Racah coefficients  $W(f f f f; FL) \equiv W(FL)$  [53].

Feeding the expansions into (2.52), we reach the concise form

$$\Delta\Omega = \frac{n^2 V}{2} \sum_{L=1}^{2f} \sum_{M=-L}^L |\Phi_M^{(L)}|^2 G_L [1 - \chi(T, \mu) G_L]. \quad (2.57)$$



Equation (2.57) shows that  $\Phi^{(L)}$  will emerge if

$$(i) \ G_L > 0, \quad \text{and} \quad (ii) \ \chi G_L \geq 1, \quad (2.58)$$

where the equal sign gives the phase boundary. Up to the quadratic order in  $\Phi_M^{(L)}$ , all  $M$  components are degenerate. Higher order terms in  $\Phi^{(L)}$  will lift the degeneracy and mix different  $L$  components. Condition (i) is necessary for the ordered phase to be stable. Consider a single  $\Phi_M^{(L)}$ , which means  $\tilde{\Gamma} = -G_L \Phi_M^{(L)} \mathcal{Y}_M^{(L)}$ . Then for the ordering to be stable, the energy  $B$  in Eqn.(2.48) must be lowered due to the presence of spin orders  $\Phi_M^{(L)}$ . Since  $B = -2V(\Phi_M^{(L)} \mathcal{Y}_M^{(L)})^2 G_L + \text{constant}$ , the case  $G_L > 0$  will ensure the spin-ordered phase is energetically favored over the normal phase. Condition (ii) simply means that the spin-ordered state is at least a local minimum in the free energy functional.

To help further understanding the conditions (2.58), consider a spin-1/2 systems. Here the only non-trivial spin order is  $L = 1$  ferromagnetic ordering, and  $G_1 = g_0$ . Then conditions (i) reduces to  $g_0 > 0$ , which means the interactions are repulsive. Condition (ii)  $\chi g_0 \geq 1$  is the Stoner criterion for ferromagnetic ordering. (Note  $\chi \rightarrow D(\varepsilon_F)$  at  $T = 0$ ). For higher spin systems,  $G_L$  represents the total interaction strength responsible for triggering the spin order  $|\Phi^{(L)}\rangle$ . Since the Racah coefficients  $W(FL)$  can be both positive and negative, not all  $g_F$ 's have to be repulsive in order to create a critical total interaction  $G_L$  to start the spin order, unlike the spin-1/2 case.

Experimental parameters are usually expressed by scattering length  $a_F$ . Thus, we define the total scattering length  $A_L$

$$G_L = \frac{8\pi\hbar^2 A_L}{\tilde{m}}, \quad A_L = \sum_F a_F (2F + 1) W(F, L). \quad (2.59)$$

Next, we note that  $\chi(T, \mu)$  in Eqn.(2.53) has the dimension of density of state. It scales as  $\sqrt{\mu}$  and hence represents a momentum scale. We can then define a wavevector  $k(T, \mu)$  as

$\chi(T, \mu) = (\tilde{m}/2\pi^2\hbar^2)k(T, \mu)$ . (Note that  $k(0, \mu) = k_n$ ). Condition (ii) then becomes

$$k(T, \mu)A_L \geq \frac{\pi}{4}, \quad \text{or} \quad k_n A_L \geq \frac{\pi}{4} \frac{k_n}{k(T, \mu)}, \quad (2.60)$$

where the equal sign gives the phase boundary.

Certainly, the larger the  $A_L$ , the easier for the  $L$ -th spin order to emerge. However, for small gas parameters  $k_n a_F < 1$ , it is not clear whether Eq.(2.60) can be satisfied. On the other hand, one sees from equation (2.59) that  $A_L$  will be maximized if the sign of  $a_F$  matches that of the Racah coefficient  $W(F, L)$ . To demonstrate this effect, we consider a set of  $a_F$ 's with the same magnitude  $\bar{a}$  with a sign matching that of  $W(F, L)$ . Equation (2.60) then becomes

$$k_n \bar{a} \geq \frac{\pi/4}{\sum_{F=0,2,..}^{2f} (2F+1)|W(F, L)|} \frac{k_n}{k(T, \mu)}. \quad (2.61)$$

This condition is plotted in Figure 2 for a spin  $f = 21/2$  Fermi gas. It shows spin orders as high as  $L = 7$  can emerge at the phase boundary for  $k_n \bar{a} < 1$ . While equation (2.61) is sufficient for the appearance of  $\Phi^{(L)}$ , it is not necessary. Once a low order  $\Phi^{(L)}$  is present, say,  $L = 1$ , higher  $L$  spin order can emerge through non-linear coupling as temperature is lowered. Finally, we note from Eqn.(2.61) that the larger the spin  $f$  of the fermions, the larger the sum in Eqn.(2.61), and the smaller the gas parameter  $k_n \bar{a}$  needed to activate the spin order.

## 2.6 Concluding Remarks

Since the diagonal element of the density matrix is the spin population along a specified spin quantization axis, say  $\hat{\mathbf{z}}$ , they can be determined by the Stern-Gerlach method. To access the off diagonal elements, one can apply a magnetic pulse to rotate  $\rho$  to  $\rho' = D\rho D^\dagger$ , where  $D$  is a rotational matrix, see Eqn.(2.11). The diagonal elements of  $\rho'$  will then

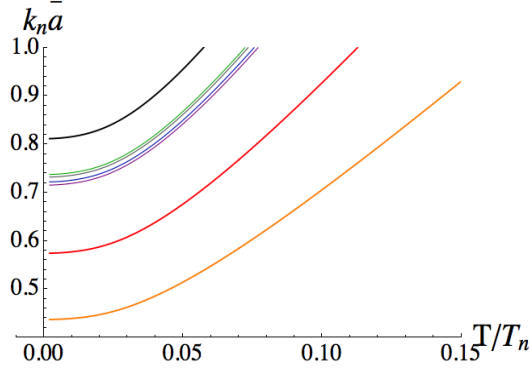


Figure 2.6: The transition temperature for spin order  $|\Phi^{(L)}\rangle$  for  $L = 1, 2, 6, 3, 5, 4, 7$ , (from bottom to top), for a spin  $f = 21/2$  Fermi gas.

contain information of the off-diagonal elements of  $\rho$  due to the rotation  $D$ . By repeating the measurement of diagonal matrix elements for different  $D$ 's, one can then extract the information of the off-diagonal matrix elements of the original density matrix  $\rho$ .

Large spin quantum gases are fertile grounds for new quantum matter. Here, we have pointed out the very rich spin order possible in large spin fermions, most of which have no analog in electron matter. We show that the spin order in different sectors can be conveniently described as Majorana antipodal points on a sequence of spheres representing the spin order of different particle-hole angular momenta. Our model calculations show that some of these orders can take the form of Platonic solids, which are structures that exist within certain *region* of the parameter space instead of a single point. These structures are therefore robust and will have good chance to be realized.

## 2.7 Appendix

### 2.7.1 Numerical Algorithm for Exploring Phase Diagram

In this appendix we specify the numerical algorithm for exploring the zero-temperature phase diagram, and introduce the dimensionless variables. The mean-field Hamiltonian reads

$$H = \sum_k c_k^\dagger c_k (\epsilon_k - \mu) + \sum_{k\mu\nu} c_{k\mu}^\dagger \Gamma_{\mu\nu} c_{k\nu}, \quad (2.62)$$

$$\Gamma_{\mu\nu} = 4 \sum_{FM} g_F \sum_{mn} \rho_{nm} \langle \mu m | FM \rangle \langle FM | \nu n \rangle. \quad (2.63)$$

where the dimensions for various quantities are  $[c_k] = 1$ ,  $[\Gamma] = E$ ,  $\rho_{\mu\nu} = \frac{1}{V} \sum_k \langle c_{k\nu}^\dagger c_{k\mu} \rangle$ ,  $[\rho] = L^{-3}$ . Here the density of states is

$$D(\epsilon) = A \sqrt{\epsilon}, \quad (2.64)$$

The particle number density<sup>1</sup> defines the Fermi energy

$$n = \frac{2}{3} A \epsilon_F^{\frac{3}{2}}, \quad A = \left( \frac{3n}{2} \right) \frac{1}{\epsilon_F^{\frac{3}{2}}}. \quad (2.65)$$

From the diagonalized mean field Hamiltonian

$$H = \sum_{k\alpha} b_{k\alpha}^\dagger b_{k\alpha} \left( \frac{\epsilon_k}{\epsilon_F} - \frac{(\mu - \mu_\alpha)}{\epsilon_F} \right), \quad (2.66)$$

we have  $n_\alpha = \frac{2}{3} A (\mu - \mu_\alpha)^{3/2}$ , that is,

$$\frac{n_\alpha}{n} = \left( \frac{\mu - \mu_\alpha}{\epsilon_F} \right)^{\frac{3}{2}}. \quad (2.67)$$

Finally, the interaction strength  $gn = \frac{4\pi\hbar^2 a}{m} n$  has dimension  $[gn] = E$ . And one can rescale it with respect to Fermi energy and obtain a dimensionless quantity<sup>2</sup>

$$\frac{gn}{\epsilon_F} = \frac{4\pi\hbar^2 a}{m} \cdot \frac{4\pi k_F^3}{3(2\pi)^3} / \frac{\hbar^2 k_F^2}{2m} = \frac{4}{3\pi} k_F a \approx 0.42 \times k_F a \quad (2.68)$$

<sup>1</sup> In current experiments on ultracold fermion gas, the typical number density is  $n \sim 10^{15-18} m^{-3}$

<sup>2</sup> For resonantly interacting fermion gas, a typical scattering length is  $a \sim 10^3 a_B \sim 10^{-7} m$ , where  $a_B = 0.5 \times 10^{-10}$  is the Bohr radius. Thus,  $g/\epsilon_F \sim 10^{-19} m^3$ .

The whole process is

1. Choose  $k_F a$ , which is a dimensionless number.
2. Convert to  $gn/\epsilon_F$  using (2.68), which is dimensionless. Choose initial  $\rho_{\mu\nu}/n$ , which is again dimensionless and of order 1. Then  $\Gamma_{\mu\nu}/\epsilon_F \sim (gn/\epsilon_F)(\rho/n)$  is dimensionless.
3. Diagonalize  $\Gamma_{\mu\nu}/\epsilon_F$ , get dimensionless matrices  $T_{\mu\nu}$  and the dimensionless chemical potential bias  $\mu_\alpha/\epsilon_F$ .

4. Then, solve for  $\mu/\epsilon_F$  through

$$1 = \sum_{\alpha} \frac{n_{\alpha}}{n} = \sum_{\alpha} \left( \frac{\mu}{\epsilon_F} - \frac{\mu_{\alpha}}{\epsilon_F} \right)^{3/2}. \quad (2.69)$$

5. Obtain  $n_{\alpha}/n$  through

$$\frac{n_{\alpha}}{n} = \left( \frac{\mu}{\epsilon_F} - \frac{\mu_{\alpha}}{\epsilon_F} \right)^{3/2}. \quad (2.70)$$

6. Then the consistency equation for the dimensionless order parameter  $\rho_{\mu\nu}/n$  becomes

$$\frac{\rho_{\mu\nu}}{n} = U_{\mu\alpha} \frac{n_{\alpha}}{n} U_{\alpha\nu}^{\dagger}. \quad (2.71)$$

The iteration process is that one start from an arbitrary  $\rho_{\mu\nu}$  and solve for  $U_{\mu\alpha}$  and  $n_{\alpha}$ .

Then, we use equation (2.71) to update the  $\rho_{\mu\nu}$  and start a new iteration.

## 2.7.2 CG coefficients, 3j and 6j Symbols

In the main text, we have extensively used the addition of angular momentums, which applies the following symmetry relations [53] for the Clebsch-Gordon coefficients:

$$\begin{aligned}
\langle j_1 m_1; j_2 m_2 | j_3 m_3 \rangle &= (-1)^{j_1+j_2-j_3} \langle j_1 - m_1; j_2 - m_2 | j_3 - m_3 \rangle \\
&= (-1)^{j_1+j_2-j_3} \langle j_2 m_2; j_1 m_1 | j_3 m_3 \rangle \\
&= (-1)^{j_1-m_1} \sqrt{\frac{2j_3+1}{2j_2+1}} \langle j_1 m_1; j_3 - m_3 | j_2 - m_2 \rangle \\
&= (-1)^{j_2+m_2} \sqrt{\frac{2j_3+1}{2j_1+1}} \langle j_3 - m_3; j_2 m_2 | j_1 - m_1 \rangle \\
&= (-1)^{j_1-m_1} \sqrt{\frac{2j_3+1}{2j_2+1}} \langle j_3 m_3; j_1 - m_1 | j_2 m_2 \rangle \\
&= (-1)^{j_2+m_2} \sqrt{\frac{2j_3+1}{2j_1+1}} \langle j_2 - m_2; j_3 m_3 | j_1 m_1 \rangle. \tag{2.72}
\end{aligned}$$

It is also useful to introduce the so-called 3j symbols, which describe the addition of two angular momentums and are related to the Clebsch-Gordon coefficients by the following equation:

$$\begin{pmatrix} j_1 & j_2 & j_3 \\ m_1 & m_2 & m_3 \end{pmatrix} = \frac{(-1)^{j_1-j_2-m_3}}{\sqrt{2j_3+1}} \langle j_1 m_1; j_2 m_2 | j_3 - m_3 \rangle, \tag{2.73}$$

$$\langle j_1 m_1; j_2 m_2 | j_3 m_3 \rangle = (-1)^{j_1-j_2+m_3} \sqrt{2j_3+1} \begin{pmatrix} j_1 & j_2 & j_3 \\ m_1 & m_2 & -m_3 \end{pmatrix}. \tag{2.74}$$

The symmetry properties of 3j-symbols include:

$$\begin{aligned}
&\begin{pmatrix} j_1 & j_2 & j_3 \\ m_1 & m_2 & m_3 \end{pmatrix} = \begin{pmatrix} j_2 & j_3 & j_1 \\ m_2 & m_3 & m_1 \end{pmatrix} = \begin{pmatrix} j_3 & j_1 & j_2 \\ m_3 & m_1 & m_2 \end{pmatrix} \\
&= (-1)^{j_1+j_2+j_3} \begin{pmatrix} j_1 & j_2 & j_3 \\ -m_1 & -m_2 & -m_3 \end{pmatrix} = (-1)^{j_1+j_2+j_3} \begin{pmatrix} j_1 & j_3 & j_2 \\ m_1 & m_3 & m_2 \end{pmatrix} \\
&= (-1)^{j_1+j_2+j_3} \begin{pmatrix} j_2 & j_1 & j_3 \\ m_2 & m_1 & m_3 \end{pmatrix} = (-1)^{j_1+j_2+j_3} \begin{pmatrix} j_3 & j_2 & j_1 \\ m_3 & m_2 & m_1 \end{pmatrix}. \tag{2.75}
\end{aligned}$$

In the main text, for technical reasons we have also used the 6j symbols, which physically describe the addition of three angular momentums. The relation between 6j-symbol

and the Racah coefficient reads

$$\begin{pmatrix} a & b & e \\ d & c & f \end{pmatrix} = (-1)^{a+b+c+d} W(abcd; ef). \quad (2.76)$$

The symmetry properties of  $6j$ -symbols include

1. When *any* two columns are interchanged, it remains invariant. e.g.

$$\begin{Bmatrix} a & b & c \\ d & e & f \end{Bmatrix} = \begin{Bmatrix} b & a & c \\ e & d & f \end{Bmatrix} \quad (2.77)$$

and etc.

2. When two elements in one row are interchanged with two elements of another, it is invariant, e.g.

$$\begin{Bmatrix} a & b & c \\ d & e & f \end{Bmatrix} = \begin{Bmatrix} a & e & f \\ d & b & c \end{Bmatrix} \quad (2.78)$$

and etc.

The summation rule for  $6j$  symbol reads

$$\sum_{j_3} (2j_3 + 1) \begin{Bmatrix} j_1 & j_2 & j_3 \\ l_1 & l_2 & l_3 \end{Bmatrix} \begin{Bmatrix} j_1 & j_2 & j_3 \\ l_1 & l_2 & l'_3 \end{Bmatrix} = \frac{1}{2l_3 + 1} \delta_{l_3 l'_3}, \quad (2.79)$$

$$\sum_{l_3} (-1)^{j_1+j_2+j_3} (2l_3 + 1) \begin{Bmatrix} j_1 & j_2 & j_3 \\ l_1 & l_2 & l_3 \end{Bmatrix} \begin{Bmatrix} j_1 & l_1 & J \\ j_2 & l_2 & l_3 \end{Bmatrix} = \begin{Bmatrix} j_1 & j_2 & j_3 \\ l_2 & l_1 & J \end{Bmatrix}. \quad (2.80)$$

Finally, the  $3j$  and  $6j$  symbols are connected through the following relation:

$$\begin{aligned} & \sum_{\mu_1 \mu_2 \mu_3} (-1)^{\mu_1 + \mu_2 + \mu_3} \begin{pmatrix} j_1 & l_2 & l_3 \\ m_1 & \mu_2 & -\mu_3 \end{pmatrix} \begin{pmatrix} l_1 & j_2 & l_3 \\ -\mu_1 & m_2 & \mu_3 \end{pmatrix} \begin{pmatrix} l_1 & l_2 & j_3 \\ \mu_1 & -\mu_2 & m_3 \end{pmatrix} \\ &= (-1)^{l_1 + l_2 + l_3} \begin{Bmatrix} j_1 & j_2 & j_3 \\ l_1 & l_2 & l_3 \end{Bmatrix} \begin{pmatrix} j_1 & j_2 & j_3 \\ m_1 & m_2 & m_3 \end{pmatrix}, \end{aligned} \quad (2.81)$$

or written in another way,

$$\begin{aligned}
& \sum_{m\mu} (-1)^{\mu_1+\mu_2+\mu_3} \begin{pmatrix} j_1 & j_2 & j_3 \\ m_1 & m_2 & m_3 \end{pmatrix} \begin{pmatrix} j_1 & l_2 & l_3 \\ m_1 & \mu_2 & -\mu_3 \end{pmatrix} \begin{pmatrix} l_1 & j_2 & l_3 \\ -\mu_1 & m_2 & \mu_3 \end{pmatrix} \\
& \quad \begin{pmatrix} l_1 & l_2 & j_3 \\ \mu_1 & -\mu_2 & m_3 \end{pmatrix} \\
& = (-1)^{l_1+l_2+l_3} \left\{ \begin{matrix} j_1 & j_2 & j_3 \\ l_1 & l_2 & l_3 \end{matrix} \right\}. \tag{2.82}
\end{aligned}$$

### 2.7.3 Relation Between the Components of Generalized Spherical Harmonic Operators $[\tilde{Y}_M^{(L)}(\mathbf{F})]_{\mu\nu}$ and the Clebsch-Gordon Coefficients $\langle f\mu|LM; f\nu\rangle$

As described in the main text, the generalized spherical harmonic operators  $\tilde{Y}_M^{(L)}(\mathbf{F})$  are constructed by first multiplying the standard spherical harmonic function with radial coordinates:  $r^L Y_M^{(L)}(\theta, \varphi)$ , and then replacing the Cartesian coordinates  $(x, y, z)$  with spin operators  $(F_x, F_y, F_z)$ . In many current literatures, this operator is used to perform tensorial decomposition instead of the Clebsch-Gordon coefficients used in this thesis. So we discuss the relation between  $[\tilde{Y}_M^{(L)}(\mathbf{F})]_{\mu\nu}$  and  $\langle f\mu|LM; f\nu\rangle$  below.

They both satisfy the definition for spherical tensors

$$U Y_M^{(L)} U^\dagger = \sum_{M'} Y_{M'}^{(L)} U_{M'M}^{(F)}, \tag{2.83}$$

so they must be proportional to each other, with proportionality coefficients independent of  $M$ . This means they must satisfy the same symmetry property when changing  $M \rightarrow -M$ . Specifically, we know that

$$Y_{F,-M} = (-1)^M Y_{FM}^\dagger. \tag{2.84}$$



Moreover,

$$\text{Tr} \left( Y_{FM}^{(f)\dagger} Y_{F'M'}^{(f)} \right) = \frac{(2f + F + 1)!}{4\pi 2^{2F} (2f - F)!} \delta_{FF'} \delta_{MM'}, \quad (2.85)$$

$$\begin{aligned} \sum_{\mu\nu} \langle f\mu | FM; f\nu \rangle \langle f\nu | F'M'; f\mu \rangle &= \sum_{\mu\nu} \sqrt{\frac{2f+1}{2F+1}} (-1)^{f+\nu} \langle F, -M | f, -\mu; f\nu \rangle \\ &\quad \times \langle f, -\mu; f\nu | F'M' \rangle \sqrt{\frac{2f+1}{2F+1}} (-1)^{f+\nu} \\ &= \frac{2f+1}{2F+1} \delta_{FF'} \delta_{MM'}. \end{aligned} \quad (2.86)$$

Examples show that there is a  $(-1)^F$  factor difference between them. Thus, in summary,

$$[Y_{FM}]_{\mu\nu}^{(f)} = (-1)^F \sqrt{\frac{2F+1}{2f+1} \frac{(2f+F+1)!}{4\pi 2^{2F} (2f-F)!}} \langle f\mu | FM; f\nu \rangle. \quad (2.87)$$

## 2.7.4 Ginzburg-Landau: General Formulation

We have the mean-field Hamiltonian

$$H_{MF} = \sum_{k, m_1, m_2} [(\epsilon_k - \mu) \delta_{m_1 m_2} + \Gamma'_{m_1 m_2}] c_{km_1}^\dagger c_{km_2} - B, \quad (2.88)$$

where

$$\Gamma'_{m_1 m_2} = 4 \sum_{FM} g_F \sum_{m_3 m_4} \rho_{m_4 m_3} \langle m_1 m_3 | FM \rangle \langle FM | m_2 m_4 \rangle, \quad (2.89)$$

$$B = 2V \sum_{FM} g_F \sum_{m_1 m_2 m_3 m_4} \rho_{m_2 m_1} \rho_{m_4 m_3} \langle m_1 m_3 | FM \rangle \langle FM | m_2 m_4 \rangle. \quad (2.90)$$

Near the phase boundary,

$$R_{\mu\nu} = \rho_{\mu\nu} - \frac{n}{2f+1} \delta_{\mu\nu} \quad (2.91)$$

is a small quantity, where we have subtracted  $\frac{1}{2f+1} \text{Tr} \rho_{\mu\nu} = n$  to make  $R_{\mu\nu}$  traceless. Here  $n$  is the particle number density. Then, we intend to expand the thermodynamic potential

$$\Omega = -\frac{1}{\beta} \ln(\text{Tr} e^{-\beta H_{MF}}) \quad (2.92)$$

with respect to  $R_{\mu\nu}$ .

To do so, we decompose the mean field Hamiltonian as

$$H_{MF} = H_0 + H_1 \quad (2.93)$$

where  $H_0$  is

$$H_0 = \sum_{k\sigma} (\epsilon_k - \mu) c_{k\sigma}^\dagger c_{k\sigma} - B, \quad (2.94)$$

and  $B$  is the condensation energy,

$$B = 2V \sum_{FM} g_F \left[ \frac{n^2}{(2f+1)^2} \right] \quad (2.95)$$

$$+ \sum_{m_1 \dots m_4} R_{m_2 m_1} R_{m_4 m_3} \langle m_1 m_3 | FM \rangle \langle FM | m_2 m_4 \rangle. \quad (2.96)$$

$B$  should be negative to make the condensate stable. In addition, here the chemical potential includes the trace of the interaction part,

$$\mu \leftrightarrow \mu - \frac{\text{Tr} \Gamma'}{2f+1} = \frac{4n}{2f+1} \sum_{FM} g_F \sum_m |\langle \sigma m | FM \rangle|^2 = \mu - 4n \sum_F g_F \frac{2F+1}{(2f+1)^2}. \quad (2.97)$$

The last step is achieved through the symmetry property of Clebsch-Gordan coefficients in equation (2.72). Similarly we can show that the linear  $R_{\mu\nu}$  term in  $B$  vanishes, and  $\Gamma_{m_1 m_2}^1$  is traceless and Hermitian. Finally, the second term in (2.93) reads

$$H_1 = \sum_{km_1 m_2} \Gamma_{m_1 m_2} c_{km_1}^\dagger c_{km_2}, \quad (2.98)$$

$$\Gamma_{m_1 m_2} = 4 \sum_{FM} g_F \sum_{m_3 m_4} R_{m_4 m_3} \langle m_1 m_3 | FM \rangle \langle FM | m_2 m_4 \rangle. \quad (2.99)$$

To expand the grand thermodynamic potential, we apply the technique of linked-cluster expansion [68]

$$\Omega = \Omega_0 - \frac{1}{\beta} \sum_{l=1}^{\infty} M_l, \quad (2.100)$$

where the correction

$$M_l = \frac{(-1)^l}{l!} \int_0^\beta d\tau_1 \dots \int_0^\beta d\tau_l \langle T_\tau V(\tau_1) \dots V(\tau_l) \rangle_{\text{con.}} \quad (2.101)$$

(Here the subscript “con.” means to include only connected diagrams.) Here  $V(\tau)$  means the operators in the “interacting picture”,  $V(\tau) = e^{\beta H_0} V e^{-\beta H_0}$ . In particular,

$$c_{km}(\tau) = c_{km} e^{-\beta(\epsilon_k - \mu)}, \quad c_{km}(\tau)^\dagger = c_{km}^\dagger e^{\beta(\epsilon_k - \mu)}. \quad (2.102)$$

The non-interacting part  $\Omega_0$  in equation (2.100) is evaluated easily

$$\begin{aligned} Z_0 &= \text{Tr} e^{-\beta H_0} = e^{\beta B} \text{Tr} e^{-\beta \sum_{k\sigma} (\epsilon_k - \mu) c_{k\sigma}^\dagger c_{k\sigma}} \\ &= e^{\beta B} \prod_{pm} \sum_{n_{pm}=0}^1 \langle n_{pm} | \prod_{k\sigma} e^{-\beta(\epsilon_k - \mu) c_{k\sigma}^\dagger c_{k\sigma}} | n_{pm} \rangle \\ &= e^{\beta B} \prod_{pm} (1 + e^{-\beta(\epsilon_p - \mu)}), \end{aligned} \quad (2.103)$$

$$\begin{aligned} \Omega_0 &= -\frac{1}{\beta} \ln Z_0 = -\frac{1}{\beta} [\beta B + \sum_{pm} \ln(1 + e^{-\beta(\epsilon_p - \mu)})] \\ &= -B - \frac{(2f+1)}{\beta} \sum_p \ln(1 + e^{-\beta(\epsilon_p - \mu)}). \end{aligned} \quad (2.104)$$

Then we evaluate the corrections. The first order term  $M_1$  is expected to vanish due to symmetry consideration of the system. We can also verify it by explicit calculations:

$$\begin{aligned} M_1 &= - \int_0^\beta d\tau \langle V(\tau) \rangle_0 = - \int_0^\beta d\tau \sum_{k\mu\nu} \Gamma_{\mu\nu} \langle c_{k\mu}^\dagger c_{k\nu} \rangle_{\text{con.}} \\ &= - \int_0^\beta d\tau \sum_{k\mu\nu} \Gamma_{\mu\nu} \frac{\delta_{\mu\nu}}{1 + e^{\beta(\epsilon_k - \mu)}}. \end{aligned} \quad (2.105)$$

Since  $\Gamma_{\mu\nu}$  is traceless, we proved  $M_1 = 0$  as desired. In the above derivation we used the property that  $\langle \dots \rangle$  is evaluated with  $H_0$ , so it is diagonal in spin space.

The second order term in equation (2.100) is

$$\begin{aligned}
M_2 &= \frac{1}{2} \int_0^\beta d\tau_1 \int_0^\beta d\tau_2 \sum_{km_1m_2;pm_3m_4} \Gamma_{m_1m_2} \Gamma_{m_3m_4} \\
&\quad \times \langle T_\tau c_{km_1}^\dagger(\tau_1) c_{km_2}(\tau_1) c_{pm_3}^\dagger(\tau_2) c_{pm_4}(\tau_2) \rangle \text{con.} \\
&= \int_0^\beta d\tau_1 \int_0^{\tau_1} d\tau_2 \sum_{km_1m_2;pm_3m_4} \Gamma_{m_1m_2} \Gamma_{m_3m_4} \langle c_{km_1}^\dagger c_{km_2} c_{pm_3}^\dagger c_{pm_4} \rangle \text{con.} \\
&= \frac{\beta^2}{2} \sum_{km_1m_2;pm_3m_4} \Gamma_{m_1m_2} \Gamma_{m_3m_4} \\
&\quad \times \left[ \frac{\delta_{m_1m_4}}{1 + e^{\beta(\epsilon_k - \mu)}} \times \delta_{m_2m_3} \left( 1 - \frac{1}{1 + e^{\beta(\epsilon_k - \mu)}} \right) \right] \delta_{kp} \\
&= \frac{\beta^2}{4} \left( \sum_k \frac{1}{1 + \cosh \beta(\epsilon_k - \mu)} \right) \sum_{\mu\nu} |\Gamma_{\mu\nu}|^2. \tag{2.106}
\end{aligned}$$

where in the last step we used the Hermitian property of  $\Gamma_{\mu\nu}$ . In summary, the second order term is found to be

$$\begin{aligned}
M_2 &= -2V \sum_F g_F \sum_{m_1\dots m_4} R_{m_2m_1} R_{m_4m_3} \langle m_1m_3 | FM \rangle \langle FM | m_2m_4 \rangle \\
&\quad - \frac{1}{\beta} \left[ \frac{\beta^2}{4} \left( \sum_k \frac{1}{1 + \cosh \beta(\epsilon_k - \mu)} \right) \sum_{\mu\nu} |\Gamma_{\mu\nu}|^2 \right] \\
&= -\frac{V}{2} \sum_{\mu\nu} \Gamma_{\mu\nu} R_{\nu\mu} - \frac{\beta}{4} \left( \sum_k \frac{1}{1 + \cosh \beta(\epsilon_k - \mu)} \right) \sum_{\mu\nu} |\Gamma_{\mu\nu}|^2 \tag{2.107}
\end{aligned}$$

with  $\Gamma_{\mu\nu}$  given in (2.99).

To include the higher order terms, we have the expression

$$\begin{aligned}
\Omega &= \text{const.} - \frac{1}{2} \left( V \sum_{\mu\nu} \Gamma_{\mu\nu} R_{\nu\mu} + f_2(T, \mu) \text{Tr} \Gamma^2 \right) \\
&\quad + f_3(T, \mu) \text{Tr} \Gamma^3 + f_4(T, \mu) \text{Tr} \Gamma^4, \tag{2.108}
\end{aligned}$$

where the additive constant is

$$\text{const.} = -V \frac{2n^2}{(2f+1)^2} \sum_F g_F (2F+1), \tag{2.109}$$

and the functions  $f_i(T, \mu)$  are

$$f_2(T, \mu) = \frac{1}{T} \sum_k n_k(1 - n_k) = \frac{1}{2T} \sum_k \frac{1}{1 + \cosh(\epsilon_k - \mu)/T}, \quad (2.110)$$

$$\begin{aligned} f_3(T, \mu) &= \frac{1}{6T^2} \sum_k n_k(1 - n_k)(1 - 2n_k) \\ &= \frac{1}{12T^2} \sum_k \frac{\tanh(\epsilon_k - \mu)/2T}{1 + \cosh(\epsilon_k - \mu)/T}, \end{aligned} \quad (2.111)$$

$$\begin{aligned} f_4(T, \mu) &= -\frac{1}{24T^3} \sum_k n_k(1 - n_k)(6n_k^2 - 6n_k + 1) \\ &= -\frac{1}{24T^3} \sum_k \frac{-1 + \frac{1}{2} \cosh \frac{\epsilon_k - \mu}{T}}{(1 + \cosh \frac{\epsilon_k - \mu}{T})^2}. \end{aligned} \quad (2.112)$$

The expansion up to 4th order is only meaningful if  $f_4(T, \mu) > 0$  within the temperature range under concern. From Eq. (2.112),  $f_4(T, \mu) > 0$  for approximately  $T/T_F < 0.35$ .

The above equations can be readily used to recover the simple spin-half case. Note that

<sup>3</sup>

$$\lim_{T \rightarrow 0} \frac{1}{2T} \frac{1}{1 + \cosh(\epsilon - \mu)/T} = \delta(\epsilon - \mu). \quad (2.113)$$

Thus,

$$f_2(T = 0, \mu) = AV \sqrt{\mu} = D(\mu)V. \quad (2.114)$$

Also, for spin-half,  $R = \begin{pmatrix} \delta n & \Delta \\ \Delta^* & -\delta n \end{pmatrix}$ ,  $\Gamma = -2g_0R$ ,  $R^2 \equiv \psi^2 = \sqrt{\delta n^2 + |\Delta|^2}$ . Then all the odd order term vanishes, and we have

$$\Omega = -\frac{g_0 n^2 V}{2} + (1 - 2g_0 D(\epsilon_F)) 2g_0 V \psi^2 + (\# > 0) \psi^4 + \dots \quad (2.115)$$

Thus, for  $g_0 > 0$  (which makes the condensation energy in the constant term negative), the second order phase transition occurs at  $2g_0 D(\epsilon_F) = 1$ , which is the renowned Stoner criterion for magnetization instability [66].

<sup>3</sup> The summation over  $\mathbf{k}$  can be expressed as  $\sum_{\mathbf{k}} = \int AV \sqrt{\epsilon} d\epsilon = \int \frac{3n}{2\epsilon_F^{3/2}} V \sqrt{\epsilon} d\epsilon$ , where  $D(\mu) = A \sqrt{\mu}$ ,  $A = 3n/2\epsilon_F^{3/2}$ , and  $\epsilon_F = \mu(2f + 1)^{2/3}$ .

### 2.7.5 Ginzburg-Landau: Dimensionless Variables

We employ the following dimensionless variables

$$\begin{aligned} g_F &\leftrightarrow \frac{g_F n}{\epsilon_F}, & R_{\mu\nu} &\leftrightarrow \frac{R_{\mu\nu}}{n}, & \Gamma_{\mu\nu} &\leftrightarrow \frac{\Gamma_{\mu\nu}}{\epsilon_F}, \\ f_n(T, \mu) &\leftrightarrow \epsilon_F^{n-1} f_n(T, \mu), & T &\leftrightarrow \frac{T}{T_F}, & \mu &\leftrightarrow \frac{\mu}{\epsilon_F}. \end{aligned} \quad (2.116)$$

Before phase transition or near the phase transition boundary, particles will distribute equally among all  $f$ -states,

$$n_\alpha(\mu_0, T) = \frac{n_\alpha(\epsilon_F, T)}{2f + 1} \quad (2.117)$$

and in particular, at  $T = 0$ , since  $n_\alpha/n = \mu^{3/2}$ ,

$$\frac{\mu_0}{\epsilon_F} = (2f + 1)^{-2/3}. \quad (2.118)$$

Further, converting the sum over  $\vec{k}$  into an integral using footnote 3, we obtain the dimensionless formulae

$$\begin{aligned} \frac{\Omega}{N\epsilon_F} = \text{const.} &- \frac{1}{2} \left( \sum_{\mu\nu} \Gamma_{\mu\nu} R_{\nu\mu} + f_2(\mu_0, T) \text{Tr}\Gamma^2 \right) \\ &+ f_3(\mu_0, T) \text{Tr}\Gamma^3 + f_4(\mu_0, T) \text{Tr}\Gamma^4, \end{aligned} \quad (2.119)$$

where the additive constant is

$$\text{const.} = -\frac{2}{(2f + 1)^2} \sum_F g_F (2F + 1), \quad (2.120)$$

and the functions  $f_i(\mu_0, T)$  are

$$f_2(\mu_0, T) = \frac{3}{4T} \int_0^\infty \frac{\sqrt{x} dx}{1 + \cosh(x - \mu_0)/T}$$

$$\xrightarrow{T \rightarrow 0} \frac{3}{2} \sqrt{\mu_0} \quad (2.121)$$

$$f_3(\mu_0, T) = \frac{1}{8T^2} \int_0^\infty \sqrt{x} dx \frac{\tanh(x - \mu_0)/2T}{1 + \cosh(x - \mu_0)/T}$$

$$\xrightarrow{T \rightarrow 0} \frac{1}{8\sqrt{\mu_0}} \quad (2.122)$$

$$f_4(\mu_0, T) = \frac{1}{16T^3} \int_0^\infty \frac{1 - \frac{1}{2} \cosh \frac{x - \mu_0}{T}}{(1 + \cosh \frac{x - \mu_0}{T})^2} \sqrt{x} dx$$

$$\xrightarrow{T \rightarrow 0} \frac{1}{64\mu_0^{3/2}} \quad (2.123)$$

Here we used the identities

$$\lim_{T \rightarrow 0} \frac{1}{2T} \int dx \frac{k(x)}{1 + \cosh(x/T)} = k(0), \quad (2.124)$$

$$\lim_{T \rightarrow 0} \frac{1}{2T^2} \int dx k(x) \frac{\tanh(x/2T)}{1 + \cosh(x/T)} = k'(0), \quad (2.125)$$

$$-\lim_{T \rightarrow 0} \frac{1}{T^3} \int dx k(x) \frac{1 - \frac{1}{2} \cosh \frac{x - \mu_0}{T}}{(1 + \cosh \frac{x - \mu_0}{T})^2} = k''(0). \quad (2.126)$$

which can be derived by noticing that

$$\lim_{T \rightarrow 0} \frac{1}{2T} \frac{1}{1 + \cosh(x/T)} = \delta(x), \quad (2.127)$$

$$-T \frac{d}{dx} \left( \frac{1}{1 + \cosh(x/T)} \right) = \frac{\tanh(x/2T)}{1 + \cosh(x/2T)}, \quad (2.128)$$

$$-\frac{T^2}{2} \frac{d^2}{dx^2} \left( \frac{1}{1 + \cosh(x/T)} \right) = \frac{1 - \frac{1}{2} \cosh \frac{x - \mu_0}{T}}{(1 + \cosh \frac{x - \mu_0}{T})^2}. \quad (2.129)$$

## 2.7.6 Ginzburg-Landau: Angular Momentum Decomposition

In previous sections, we have decomposed the grand thermodynamic potential  $\Omega$  into different orders of  $\Gamma_{m_1 m_2}$ , where  $\Gamma_{m_1 m_2}$  is generally a superposition of different total angular

momentums. In this sections, we further separate

$$\Gamma_{\mu\nu} = 4 \sum_F g_F \sum_{m_1 m_2} R_{m_2 m_1} \langle \mu m_1 | FM \rangle \langle FM | \nu m_2 \rangle, \quad (2.130)$$

into components of different total angular momentums using the decomposition

$$R_{\mu\nu} = \sum_{FM} c_{FM} \langle f\mu | FM; f\nu \rangle, \quad (2.131)$$

where  $c_{FM}$ 's are given by

$$c_{FM} = (-1)^{F+M} \frac{2F+1}{2f+1} \sum_{\mu\nu} R_{\mu\nu} \langle f\mu | FM; f\nu \rangle. \quad (2.132)$$

The above relation can be derive with the aid of Eq. (2.72),

$$R_{\mu\nu} = \sum_{JM_J} c_{JM_J} \langle f\mu | JM_J; f\nu \rangle = \sum_{JM_J} c_{JM_J} \langle JM_J | f, -\nu; f\mu \rangle \sqrt{\frac{2f+1}{2J+1}} (-1)^{f+\nu}. \quad (2.133)$$

So

$$\sum_{\mu\nu} R_{\mu\nu} \langle f-\nu; f\mu | FM \rangle (-1)^{f+\nu} = \sum_{JM_J} \sqrt{\frac{2f+1}{2J+1}} c_{JM_J} \delta_{FJ} \delta_{MM_J} = \sqrt{\frac{2f+1}{2F+1}} c_{FM}. \quad (2.134)$$

We remark that a similar decomposition can be carried out using  $Y_{FM}$ , while here we use the Clebsch-Gordon coefficients in (2.131) for technical convenience. Note that  $\langle f\mu | F-M; f\nu \rangle = \langle f-\nu | F-M; f-\mu \rangle (-1)^{F+M} = (-1)^{2F+M} \langle f\nu | FM; f\mu \rangle$ . In our case,  $f$ 's are half-integers, so  $F$ 's are integers, and therefore

$$\langle f\mu | F-M; f\nu \rangle = (-1)^M \langle f\nu | FM; f\mu \rangle. \quad (2.135)$$

Thus, if we expand

$$R_{\mu\nu} = \sum_{FM} c_{FM} \langle f\mu | FM; f\nu \rangle,$$

the coefficient also satisfies  $c_{F-M} = c_{FM}^* (-1)^M$  due to the Hermitian property of  $R_{\mu\nu}$ .



The purpose of such decomposition is to obtain the total angular momentum, i.e. if only  $c_{2M} \neq 0$ , we know the total angular momentum is 2. This is true because  $\langle f\mu|FM; f\nu\rangle$  satisfies the definition for a spherical tensor of order  $(F, M)$ , which can be shown through the following. Let the rotation matrix be  $U = e^{-i(\vec{f}_1 + \vec{f}_2) \cdot \vec{\theta}} = U_1 U_2$ , then

$$\begin{aligned} \langle LM|f_1\mu_1 f_2\mu_2\rangle &= \langle LM|U^\dagger U|f_1\mu_1 f_2\mu_2\rangle \\ &= \sum_{L'M', \mu'_1 \mu'_2} \langle LM|U^\dagger|L'M'\rangle \langle L'M'|f_1\mu'_1 f_2\mu'_2\rangle \langle f_1\mu'_1 f_2\mu'_2|U|f_1\mu_1 f_2\mu_2\rangle \\ &= \sum_{M' \mu'_1 \mu'_2} (U^\dagger)_{MM'}^{(L)} \langle LM'|f_1\mu'_1 f_2\mu'_2\rangle U_{\mu'_1 \mu_1}^{(f_1)} U_{\mu'_2 \mu_2}^{(f_2)}. \end{aligned}$$

Then,

$$\sum_{\mu_1} (U^\dagger)_{\mu_1 \mu'_1}^{(f_1)} \langle LM|f_1\mu_1 f_2\mu_2\rangle = \sum_{M' \mu'_2} (U^\dagger)_{MM'}^{(L)} \langle LM'|f_1\mu'_1; f_2\mu'_2\rangle U_{\mu'_2 \mu_2}^{(f_2)}.$$

Thus, we have

$$\sum_{M'} \langle f\mu|FM'; f\nu\rangle U_{M'M}^{(F)} = \sum_{\mu' \nu'} (U^\dagger)_{\mu \mu'}^{(f)} \langle f\mu'|FM; f\nu'\rangle U_{\nu' \nu}^{(f)}, \quad (2.136)$$

which is the definition for a spherical tensor.

The key of performing the decomposition is to apply the relation

$$\begin{aligned} &\sum_{\mu \nu M} \langle FM|f\mu; fm\rangle \langle f\mu|F_1 M_1; f\nu\rangle \langle f\nu; fn|FM\rangle \\ &= \langle fn|F_1 M_1; fm\rangle (-1)^{2f-F} (2F+1) W(ffff, FF_1), \end{aligned} \quad (2.137)$$

where  $W(ffff, FF_1)$  is the Racah coefficient. In our case  $F$  is an even number and  $2f$  is an odd number, so  $(-1)^{2f-F} = -1$ . Then

$$\Gamma_{\mu \nu} = \sum_{F_1 M_1} c_{F_1 M_1} K_{F_1} \langle f\mu|F_1 M_1; f\nu\rangle, \quad (2.138)$$

where

$$K_{F_1} = -4 \sum_F g_F (2F+1) W(ffff; FF_1). \quad (2.139)$$

Further note that

$$\sum_{\mu\nu} \langle f\mu|F_1M_1; f\nu\rangle \langle f\nu|F_2M_2; f\mu\rangle \quad (2.140)$$

$$= (-1)^{f+\nu} \sqrt{\frac{2f+1}{2F_1+1}} \langle f-\nu; f\mu|F_1M_1\rangle \times (-1)^{f+\mu} \sqrt{\frac{2f+1}{2F_2+1}} \langle f-\nu; f\mu|F_2-M_2\rangle \quad (2.141)$$

$$= \frac{2f+1}{2F_1+1} \delta_{F_1F_2} \delta_{M_1, -M_2} (-1)^{M_1}. \quad (2.142)$$

Using the property  $c_{F_1, -M_1} = (-1)^{M_1} c_{F_1M_1}^*$ , we have

$$\sum_{\mu\nu} \Gamma_{\mu\nu} R_{\nu\mu} = \sum_{F_1M_1, F_2M_2} c_{F_1M_1} K_{F_1} c_{F_2M_2} \sum_{\mu\nu} \langle f\mu|F_1M_1; f\nu\rangle \langle f\nu|F_2M_2; f\mu\rangle \quad (2.143)$$

$$= \sum_{F_1M_1} |c_{F_1M_1}|^2 \frac{2f+1}{2F_1+1} K_{F_1}, \quad (2.144)$$

$$\sum_{\mu\nu} \Gamma_{\mu\nu} \Gamma_{\nu\mu} = \sum_{F_1M_1} |c_{F_1M_1}|^2 \frac{2f+1}{2F_1+1} K_{F_1}^2. \quad (2.145)$$

And the second order term in the thermodynamic potential is then

$$M_2 = \sum_{F_1M_1} |c_{F_1M_1}|^2 \left[ -\frac{1}{2} \frac{2f+1}{2F_1+1} K_{F_1} (1 + f_2(T) K_{F_1}) \right]. \quad (2.146)$$

with  $K_{F_1}$  given by (2.139). After the scaling (with Fermi energy  $\epsilon_F$  and number density  $n$ )

introduced in Appendix 2.7.1, we have

$$\frac{gn}{\epsilon_F} \approx 0.42 \times k_F a. \quad (2.147)$$

## **Chapter 3: NON-TRIVIAL MANIFOLDS FOR SPINOR CONDENSATES IN SYNTHETIC GAUGE FIELDS**

### **3.1 Introduction**

We explore another new directions in cold atom researches in this chapter, which is the effects of non-trivial background manifold where the quantum gases could reside. In the study of quantum matter, one usually deals with Euclidean space. Spaces with non-zero curvatures or non-trivial topology are seldom encountered. However, recent studies show that many important properties of many-body systems can be revealed by changing the geometry or topology of the background manifold. For instance, the ground state degeneracy of a quantum Hall system is shifted by an amount proportional to the genus of the manifold [69]. A change of the spatial geometry of the system can also lead to a dissipation free “Hall viscosity” response in two dimensional systems [70–72], which is the topic of the next chapter. Furthermore, it was found in graphene that curvature effects can mimic those of gauge fields [37]. The fact that manifolds with non-Euclidean geometry can help uncover new features of quantum matter makes it desirable to create manifolds of controllable shape, and to develop capability to add in synthetic gauge fields.

The purpose of this chapter is to discuss how to create quantum gases on curved surfaces with synthetic gauge fields, as well as their properties. As a first step, we consider in detail a spinor Bose-Einstein condensate (BEC) in the form of a cylindrical surface (produced by an

annulus trap). Bose condensation will magnify quantum phenomena on the macroscopic scale, while large spins will lead to stronger synthetic gauge fields through Berry phase effects. This study is also an extension of the on-going effort of generating synthetic gauge fields in quantum gases (using rotating traps [73–80], Raman transitions or shaking lattices [81–88]) to explore the effect of geometry and topology of the underlying manifold on BECs in such settings (there has also been a recent study in a lattice system [89]). Finally, we will briefly discuss the extension to other shapes of manifolds, such as spherical and toroidal surfaces, and the vortex physics associated with them.

### 3.1.1 Preliminaries of Optical Traps

Trapping potentials in cold atom systems are generally produced by introducing a smooth energy shift of the atomic levels in space. Specifically, when atoms are subject to an external field, i.e. electric field, magnetic field, etc., its energy levels will be shifted. Then if the external field is inhomogeneous but does not change too rapidly (compared with the size of the atom) in space, atoms will adiabatically stay in the same energy level  $E_n + E'_n(\mathbf{r})$ , but with spatially dependent energy shifts. Such an energy shift essentially functions like a potential  $V(\mathbf{r}) = E'(\mathbf{r})$  in length scales much larger than the atomic size.

A simple example is the potential produced by Zeeman effects when atoms are exposed to inhomogeneous magnetic fields. It amounts to a generalized Stern-Gerlach experiment. The atomic levels are shifted by  $E_n - m\boldsymbol{\mu} \cdot \mathbf{B}(\mathbf{r})$ , where  $\boldsymbol{\mu}$  is the magnetic moment of the atom (which is chiefly contributed by electrons as the nuclear moment is several orders of magnitudes smaller), and  $m$  is the magnetic quantum number for the state. If an atom adiabatically stays in certain state  $|fm\rangle$ , the energy shift is linearly proportional to the strength of magnetic field  $|\mathbf{B}(\mathbf{r})|$ , see Fig. 3.1. In fact, this is the idea behind earliest magnetic traps

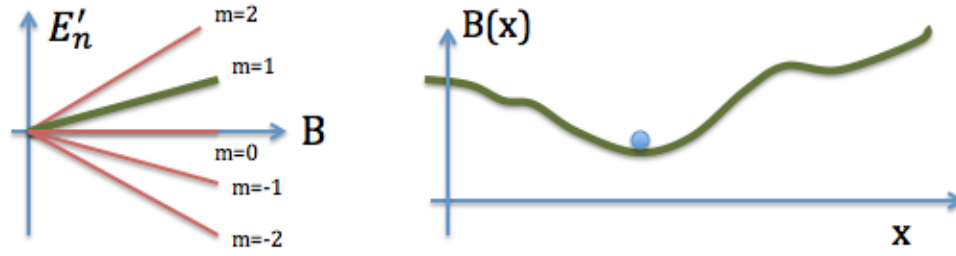


Figure 3.1: Magnetic trap as a simple example of trapping potential. **Left:** In the atomic scale, energy levels are shifted due to the magnetic field. And the magnitude of shift is proportional to the strength of the field. For states  $m = 1, 2$  shown schematically here, the energy is lower for weaker  $B$ , and they are called “low-field-seeking” states. **Right:** The field changes in scales much larger than the atomic size, and the atom adiabatically stays in the same level with negligible transition amplitudes to other  $m$ -states. Then the energy shift  $\propto |B|$ , and functions like a potential.

used in cold atom experiments, and is still widely used nowadays. Usually a quadrupolar magnetic field is used, which can be produced by two parallel rings carrying currents circulating in the opposite directions. The field is weakest in the center, and therefore for “low-field seeking states” the effective potential functions as a trapping one. For more details, see [67].

The magnetic trap discussed above has the character that the internal degree of freedom  $m$  is frozen by external magnetic field, which is the basis for magnetic trapping. Optical trapping, on the other hand, uses the Stark shift introduced by the electric-field component in a laser beam, and does not lift the degeneracy of different  $m$ 's. Therefore, the ground state manifold  $|fm\rangle$  consist of fixed  $f$  but degenerate  $m = -f, -f + 1, \dots, f$  states. We review the basic properties of optical traps below.

When a neutral atom is exposed to electric fields  $\mathcal{E}$  (in an electromagnetic field), its charge distribution of the electron cloud is distorted, and it acquires an electric dipole in

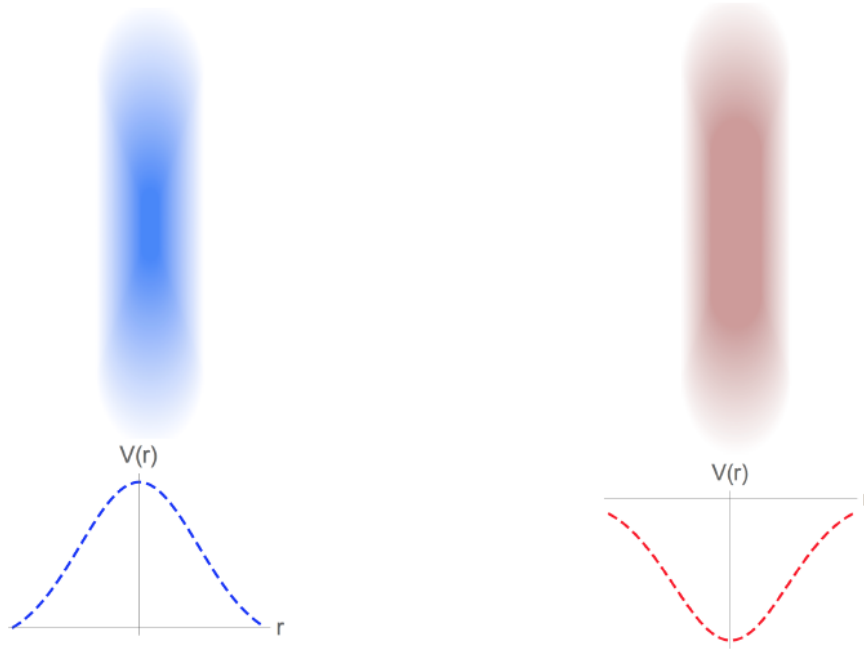


Figure 3.2: The blue-detuned ( $\omega > \omega_{mn}$ ) and red-detuned ( $\omega < \omega_{mn}$ ) Gaussian laser beams, and the effective potentials they produce respectively. Here  $\omega$  is the frequency of the laser, and  $\omega_{mn} = \omega_m - \omega_n$  is the atomic level spacing between  $|m\rangle$  and  $|n\rangle$  that is closest to resonance with the laser frequency.

the lowest order approximation

$$\hat{\mathbf{d}} = -e \sum_j \hat{\mathbf{r}}_j, \quad (3.1)$$

where  $\mathbf{r}_j$  are the position of atomic electrons relative to the nuclei. The atomic levels are correspondingly shifted due to such perturbations. The Hamiltonian describing such influence is

$$H = H_0 + H', \quad H' = -\hat{\mathbf{d}} \cdot \mathcal{E} \quad (3.2)$$

where  $H_0$  gives the unperturbed atomic levels. Here in the atomic scale, we consider the electric field to be constant in space and it oscillates with frequency  $\omega$

$$\mathcal{E} = \mathcal{E}_0 \cos \omega t. \quad (3.3)$$

Denote the unperturbed atomic levels generally as  $|n\rangle$  with frequency  $\omega_n$ , and expand the perturbed wave function as

$$|\psi(t)\rangle = \sum_n a_n(t) e^{-i\omega_n t} |n\rangle. \quad (3.4)$$

From the Schrodinger's equation we have

$$i\hbar \partial_t a_n(t) = \sum_l a_l(t) \langle n|H'(t)|l\rangle e^{-i\omega_{nl}t}, \quad (3.5)$$

where  $\omega_{ln} = \omega_l - \omega_n$ . Suppose initially the state is  $|l\rangle$ , to the second order approximation [67],

$$\begin{aligned} \dot{\phi}_l &= \frac{\langle l|d_i|l\rangle}{\hbar} \mathcal{E}_0 \cos \omega t \\ &+ \frac{\mathcal{E}_0^2}{2\hbar^2} \sum_{n \neq l} |\langle n|d_i|l\rangle|^2 e^{-i\omega_{nl}t} \cos \omega t \left[ \frac{e^{i(\omega_{nl}+\omega)t} - 1}{\omega_{nl} + \omega} + \frac{e^{i(\omega_{nl}-\omega)t} - 1}{\omega_{nl} - \omega} \right]. \end{aligned} \quad (3.6)$$

Here we denote  $a_l(t) = e^{i\phi_l(t)}$ , so  $\phi_l$  indicates an energy shift of the initial state  $l$  with frequency  $\omega_l$  in (3.4). The dipole selection rule gives  $\langle l|d_i|l\rangle = 0$ , and states with different orbital angular momentums are coupled. In other words, states with different magnetic quantum numbers remain almost degenerate, unlike in the case of magnetic trapping [18].

Taking a time-average, we have the energy shift

$$E'_l(\mathbf{r}) = \hbar \langle \dot{\phi}_l \rangle_t = \frac{\mathcal{E}_0^2(\mathbf{r})}{2\hbar} \sum_n \frac{\omega_{nl}}{\omega_{nl}^2 - \omega^2} |\langle n|d_i|l\rangle|^2. \quad (3.7)$$

Regarding the energy shift as trapping potential, there are two characters that will be extensively used later on this chapter:

1. **Blue-detuned and red-detuned lasers.** The most important contribution usually comes from the state  $n$  where  $\omega_{nl}$  is closest to the laser frequency  $\omega$ . Without loses of generality, let us set  $\omega_{nl} > 0$ . Then we see for lower frequency  $\omega < \omega_{nl}$ , the potential is an attractive one, and the laser beam is called a red-detuned one. Similarly for  $\omega > \omega_{nl}$  the laser beam is called a blue-detuned one producing repulsive potentials.

2. **Strength of potential.** Clearly, the stronger the laser field  $\mathcal{E}_0$  is, the stronger the potential will be. To obtain a local maximum, one can put a lense in front of a laser beam to focus it. Usually the intensity of the laser beam has the Gaussian shape; then around the center of the Gaussian intensity, the atoms approximately feel a harmonic trap.

A schematic plot for the lasers and their effective potentials are plotted in Fig.3.2.

### 3.1.2 Synthetic Gauge Fields: General Discussions

We review some of the experimental schemes to generate synthetic gauge fields in cold atom systems. The difference of cold atom systems from usual solid-state electronic systems is that atoms are neutral particles, and do not feel the Lorentz forces as charged electrons do. The effort of making the neutral atoms behave like charged particles moving in electromagnetic fields leads to the subject of “synthetic gauge fields”.

The common feature in all the experimental schemes is that one actually tries to synthesize the “gauge potential”  $\mathbf{A}_{\text{syn}}$ , instead of the electric or magnetic fields  $\mathbf{E}$ ,  $\mathbf{B}$ . Specifically, in the kinetic term of the Hamiltonian

$$T = \frac{\mathbf{p}^2}{2m} \rightarrow \frac{(\mathbf{p} - \mathbf{A}_{\text{syn}}(\mathbf{x}))^2}{2m}, \quad (3.8)$$

one tries to generate a position-dependent kick to the momentum. Then the effective Hamiltonian resembles that in the presence of a gauge field (described by the gauge potential  $\mathbf{A}_{\text{syn}}$ ). As such, it is clear that the “synthetic gauge field” generated in this way generally will not enjoy the gauge freedom  $\mathbf{A} \rightarrow \mathbf{A} + \nabla\chi$ , because different  $\mathbf{A}_{\text{syn}}$  corresponds to different physical systems. (For a specific example that shows the physical difference between “Landau gauge” and “spherical gauge” for uniform magnetic fields, see [90]. It chiefly concerns the effect of boundary conditions). In this sense, the word “synthetic gauge field”



is a bit misleading, as gauge degree of freedom is often regarded as an important feature of gauge fields. But with these caveats in mind, in the following we will follow most literatures and continue calling the synthesized gauge potential a “synthetic gauge field” for a charge-neutral system.

Up to date, there has been a number of experimental schemes realizing Abelian or non-Abelian synthetic gauge fields (spin-orbit coupling) in the cold atom setting, both in the presence or absence of optical lattices. These include the rotating gases [91], Raman coupling [92], shaking lattice [93], and spin textures [94–96]. For concreteness, we next quickly review the scheme in rotating gases for example. Such a scheme involves a time-dependent trapping potential  $V(\mathbf{r}, t)$  that rotates at certain frequency  $\Omega$ . Then, the non-interacting part of the Hamiltonian

$$T + V = \frac{\mathbf{p}^2}{2m} + V(\mathbf{r}, t) \quad (3.9)$$

can be rewritten in the frame rotating with the potential as

$$\rightarrow T_R + V_R = \left( \frac{\mathbf{p}^2}{2m} - \boldsymbol{\Omega} \cdot \mathbf{L} \right) + V(\mathbf{r}) \quad (3.10)$$

where the trapping potential becomes static in the co-moving frame, and the Hamiltonian gains an additional term due to the centrifugal force in the non-inertial frame [91, 97]. We will derive it in a moment. Here  $\mathbf{L} = \mathbf{r} \times \mathbf{p}$  is the angular-momentum operator. Use the relation  $\boldsymbol{\Omega} \cdot (\mathbf{r} \times \mathbf{p}) = \mathbf{p} \cdot (\boldsymbol{\Omega} \times \mathbf{r})$ , we easily see

$$T_R = \frac{(\mathbf{p} - \mathbf{A}_{\text{rot}})^2}{2m} - \frac{m(\boldsymbol{\Omega} \times \mathbf{r})^2}{2} \quad (3.11)$$

where the synthetic gauge potential

$$\mathbf{A}_{\text{rot}} = m\boldsymbol{\Omega}(-y, x) = m\boldsymbol{\Omega} \times \mathbf{r} \quad (3.12)$$

Such a gauge potential corresponds to a static uniform magnetic field  $\mathbf{B} = \nabla \times \mathbf{A}_{\text{rot}} = 2m\Omega \mathbf{e}_z$ .

We can understand the derivation of (3.10) from two perspectives. One uses the transform of Hamiltonian and states between rotating and laboratory frames

$$H_{\text{rot}} = e^{-i(\Omega t) \cdot \mathbf{L}} H(t) e^{i(\Omega t) \cdot \mathbf{L}}, \quad |\psi_{\text{rot}}\rangle = e^{i(\Omega t) \cdot \mathbf{L}} |\psi\rangle. \quad (3.13)$$

In the laboratory frame we have the Schrodinger's equation  $i\partial_t |\psi\rangle = H(t) |\psi\rangle$ , so in the rotating frame we have  $i\partial_t |\psi_{\text{rot}}\rangle = (H_{\text{rot}} - \Omega \cdot \mathbf{L}) |\psi_{\text{rot}}\rangle$ . Alternatively, we can start from the Lagrangian, which is an absolute independent of frames

$$\mathcal{L} = \frac{m\mathbf{v}^2}{2} - V(\mathbf{r}, t) = \frac{m(\mathbf{v}_{\text{rot}} + \Omega \times \mathbf{r}_{\text{rot}})^2}{2} - V(\mathbf{r}_{\text{rot}}) \quad (3.14)$$

Then we directly construct the Hamiltonian in the rotating frame through Legendre transform

$$\begin{aligned} \mathbf{p}_{\text{rot}} &= \frac{\partial \mathcal{L}}{\partial \mathbf{v}_{\text{rot}}} = m(\mathbf{v}_{\text{rot}} + \Omega \times \mathbf{r}_{\text{rot}}), \\ H_{\text{rot}} &= \mathbf{v}_{\text{rot}} \cdot \mathbf{p}_{\text{rot}} - \mathcal{L} = \frac{m\mathbf{v}_{\text{rot}}^2}{2} - \frac{m(\Omega \times \mathbf{r}_{\text{rot}})^2}{2} + V(\mathbf{r}_{\text{rot}}) \\ &= \frac{(\mathbf{p}_{\text{rot}} - m\Omega \times \mathbf{r}_{\text{rot}})^2}{2m} - \frac{m(\Omega \times \mathbf{r}_{\text{rot}})^2}{2} + V(\mathbf{r}_{\text{rot}}) \\ &= \frac{\mathbf{p}_{\text{rot}}^2}{2m} - \Omega \times \mathbf{L} + V(\mathbf{r}_{\text{rot}}), \end{aligned} \quad (3.15)$$

$$(3.16)$$

which is the same as (3.10).

Later on in this chapter, we will employ another scheme that uses the spin textures of the system to generate synthetic Abelian and non-Abelian gauge fields. We provide some general discussions of this scheme in the following [94, 95]. The idea is that for particles with spin, we can separate its wave function  $\psi(\mathbf{r}) = \zeta(\mathbf{r})\phi(\mathbf{r})$  in terms of spin and density degrees of freedom. If the external magnetic field fixes the spin degree of freedom  $\zeta(\mathbf{r})$  (i.e. by Zeeman effects), then the effective Hamiltonian for the density degree of freedom  $\phi(\mathbf{r})$

resembles that of a charged particle moving in electromagnetic field. For instance, consider a system in a strong magnetic field where the spin of a particle adiabatically follows the direction of the field everywhere. Then when a particle completes a loop, its spin rotations endow the particle a Berry phase, just like that for a charged particle moving in a magnetic field.

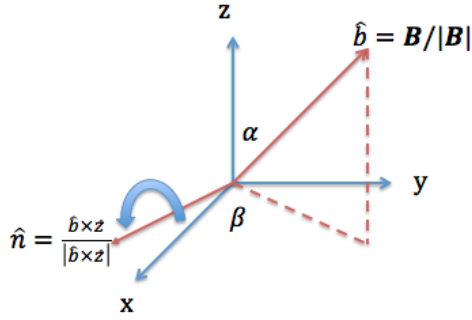


Figure 3.3: Directions of local magnetic fields

Now we lay down the concrete mathematical formulation for such a scheme. Consider a neutral particle with certain spin moving in external magnetic fields:

$$H = \frac{\mathbf{p}^2}{2m} - \lambda_1 \mathbf{B}(\mathbf{r}, t) \cdot \mathbf{F} + \lambda_2 (\mathbf{B}(\mathbf{r}, t) \cdot \mathbf{F})^2. \quad (3.17)$$

Here the external real magnetic field  $\mathbf{B}(\mathbf{r}, t)$  serves to produce a (linear and quadratic) Zeeman effect for neutral atoms, and it can vary in space and time.  $\mathbf{F}$  is the spin operator. The system satisfies the Schrodinger equation  $i\hbar\partial_t|\psi\rangle = H|\psi\rangle$ . Now we perform a local spin rotation such that everywhere the spin-quantization axis is along the direction of local magnetic field

$$|\psi_r\rangle = U|\psi\rangle, \quad U = e^{i\alpha\hat{n}\cdot\mathbf{F}} \quad (3.18)$$

Here  $\alpha(\mathbf{r}, t)$  is the angle between the  $z$ -axis and the direction of the magnetic field

$$\hat{\mathbf{b}} = \mathbf{B}/|\mathbf{B}| = (\sin \alpha \cos \beta, \sin \alpha \sin \beta, \cos \alpha), \quad (3.19)$$

and the local rotation axis is

$$\hat{\mathbf{n}}(\mathbf{r}, t) = \hat{\mathbf{b}} \times \mathbf{e}_z / |\hat{\mathbf{b}} \times \mathbf{e}_z| = (\sin \beta, -\cos \beta, 0). \quad (3.20)$$

See Fig. 3.3. Then

$$U\mathbf{B} \cdot \mathbf{F}U^\dagger = |\mathbf{B}|F_z, \quad (3.21)$$

$$U\mathbf{p}U^\dagger = (\mathbf{p} - i\hbar U\nabla U^\dagger) \quad (3.22)$$

$$i\hbar\partial_t|\psi_r\rangle = (i\hbar(\partial_t U)U^\dagger + UHU^\dagger)U|\psi\rangle \quad (3.23)$$

and the Schrodinger's equation in the transformed frame becomes

$$i\hbar\partial_t|\psi_r\rangle = \left[ \frac{(\mathbf{p} - \mathbf{A}_{\text{syn}})^2}{2m} + \Phi_{\text{syn}} - \lambda_1|\mathbf{B}|F_z + \lambda_2|\mathbf{B}|^2F_z^2 \right] |\psi_r\rangle, \quad (3.24)$$

Here the synthetic vector and scalar potentials are

$$\mathbf{A}_{\text{syn}} = i\hbar U\nabla U^\dagger, \quad \Phi_{\text{syn}} = i\hbar(\partial_t U)U^\dagger. \quad (3.25)$$

Now we can see the emergence of synthetic electric and magnetic fields, as well as non-Abelian gauge fields (spin-orbit coupling) in different parameter regimes. Specifically, in the Abelian regime where  $\lambda_2 \rightarrow 0$  and  $\lambda_1$  are strong enough, the spins are all polarized along the direction of local magnetic field. Then in the rotated frame the state is  $|f, m_f = f\rangle$ , where  $f$  is the spin of the particle. Thus, we can replace  $F_z \rightarrow f$ , and  $F_x, F_y \rightarrow 0$  in  $U = e^{-i\alpha\hat{\mathbf{n}}\cdot\mathbf{F}}$  after taking derivatives. In this case, we obtain the Abelian synthetic gauge field  $\mathbf{A}_{\text{syn}}, \Phi_{\text{syn}}$  with electric and magnetic fields equal to

$$\mathbf{E}_{\text{syn}} \equiv -\frac{\partial\mathbf{A}_{\text{syn}}}{\partial t} - \nabla\Phi = i\hbar \left[ (\nabla U)(\partial_t U^\dagger) - (\partial_t U)(\nabla U^\dagger) \right], \quad (3.26)$$

$$\mathbf{B}_{\text{syn}} \equiv \nabla \times \mathbf{A}_{\text{syn}} = i\hbar(\nabla U) \times (\nabla U^\dagger). \quad (3.27)$$

Thus, we see that a spatially varying external magnetic field (that polarizes  $(\alpha, \hat{n})$  in  $U, U^\dagger$ ) results in synthetic magnetic field; if the external magnetic field further depends on time, it also induces a synthetic electric field.

In another parameter regime where  $\lambda_1, \lambda_2$  takes the values such that more than one spin components are almost degenerate in the ground state, we have the non-Abelian gauge field  $\mathbf{A}_{\text{syn}}, \Phi_{\text{syn}}$ . We briefly discuss such extensions in the appendix of this chapter. In the following we will focus on the Abelian case.

### 3.2 Realization of a BEC on a cylindrical surface with synthetic gauge fields in Landau gauge

A cylindrical surface has a non-trivial topology (i.e. a hole) and an extrinsic curvature. As we shall see, the non-trivial topology of this surface leads to two types of vortices (denoted as  $A$  and  $B$ ) with the *same* circulation, in contrast to the single type of vortex for given circulation in planar geometry. This is because there are only two conformal maps that take a plane into a cylinder that satisfy the topological constraint. We further show that in the presence of a synthetic magnetic field, the confining potential of the annulus will give rise to a “necklace” of vortices – a row of alternating  $A$  and  $B$  vortices surrounding the center of the cylinder at  $z = 0$ , rather than the usual hexagonal vortex array in a planar geometry. Such vortex patterns will shown up in time-of-flight experiments as a density distribution with  $2n$ -fold rotational symmetry around the axis of the cylinder, ( $n$  being the number of  $A$ - $B$  vortex pairs in the ground state), which can be detected easily. The fact that structures as fundamental as vortices can come in different varieties on a cylindrical surface suggests that many new phenomena are in store for more complex curved spaces.

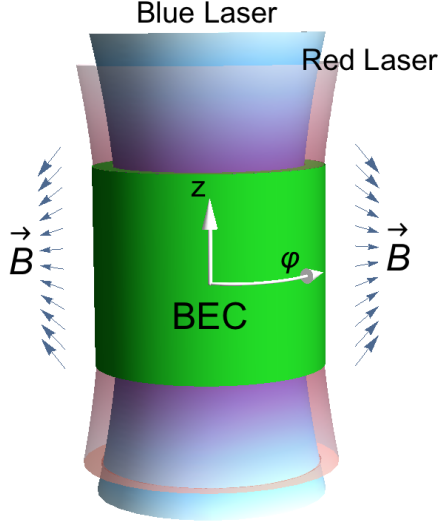


Figure 3.4: The (repulsive) blue-detuned laser beam penetrates through the center of a (attractive) red-detuned laser, and the BEC is confined in the cylindrical surface.

### 3.2.1 Trapping BEC on a cylindrical surface

To create a quasi 2D BEC in the form of a cylindrical surface, we first create an annulus trap of narrow width by piercing through a trap (produced by a red-detuned laser) with a repulsive potential (produced by a blue-detuned laser), as shown in Fig.3.4. This will create a confining well in the radial direction with a minimum at radius  $R$ . A harmonic potential  $V(z) = M\omega_z^2 z^2/2$  is applied along  $z$ . If  $\omega_z$  is much weaker than the trap frequency in the radial direction, then a quantum gas in this trap will form a quasi-2D cylindrical surface with radius  $R$ , thickness  $\sigma$ , and finite height. (See Fig. 3.4).

The total potential produce by the red and blue detuned laser, denoted as  $V_R$  and  $V_B$ , is

$$V(r) = -V_R e^{-r^2/2\sigma_r^2} + V_B e^{-r^2/2\sigma_b^2}, \quad (3.28)$$

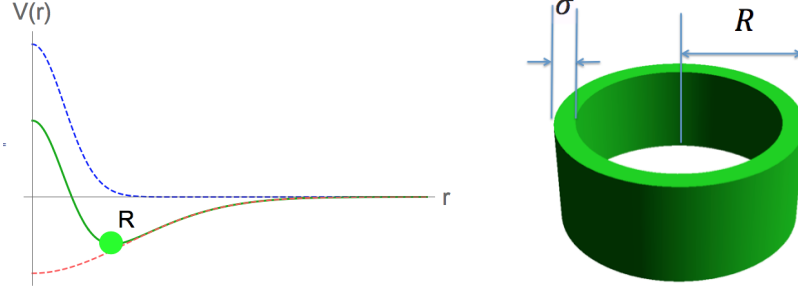


Figure 3.5: The blue and red dotted lines represent the attractive and the repulsive potential due to the red-detuned and blue-detuned lasers. The green curve is the combined potential, with a minimum at  $R$ . For sufficiently large  $R$  and for weak harmonic confinement along  $z$ , the quantum gas will form a quasi-2D cylindrical layer with thickness  $\sigma \ll R$ , shown in green.

where  $\sigma_r, \sigma_b$  are the Gaussian width of these lasers. The minimum  $r_o$  is located at

$$0 = \left. \frac{\partial V}{\partial r} \right|_{r=r_0} \Rightarrow r_0^2 = \frac{2\sigma_b^2 \sigma_r^2}{\sigma_r^2 - \sigma_b^2} \ln \left( \frac{V_B \sigma_r^2}{V_R \sigma_b^2} \right). \quad (3.29)$$

For  $r_o > 0$ , we need (i)  $\sigma_r > \sigma_b$  (“blue laser penetrating through the center of red laser”), and (ii)  $V_B/V_R > \sigma_b^2/\sigma_r^2$ , (blue laser must be strong enough to repulse gases from the center). By tuning the relative strength and width of the red and blue detuned lasers, we can adjust the location of the minimum  $r_o$ .

The “width” of the annulus potential is given by the trapping frequency around the minima  $r_0$ , where  $V(r)$  around  $r_0$  behaves like

$$V(r) \approx V^{(0)} + \frac{M\omega_r^2}{2}(r - r_0)^2, \quad M\omega_r^2 = V^{(2)} \quad (3.30)$$

$$V^{(2)} = \left. \frac{\partial^2 V}{\partial r^2} \right|_{r_0} = \frac{V_R}{\sigma_r^2} \left( 1 - \frac{r_0^2}{\sigma_r^2} \right) e^{-r_0^2/2\sigma_r^2} - \frac{V_B}{\sigma_b^2} \left( 1 - \frac{r_0^2}{\sigma_b^2} \right) e^{-r_0^2/2\sigma_b^2} \quad (3.31)$$

The trapping frequency  $\omega_r$  can be tuned by changing  $V_R$  and  $V_B$  together, while keeping the ratio  $V_R/V_B$  fixed.

It is convenient to introduce the dimensionless variables

$$\kappa_1 = \frac{\sigma_r}{\sigma_b}, \quad \kappa_2 = \frac{\omega_B}{\omega_R}, \quad (3.32)$$

where  $\omega_{B(R)} = \sqrt{V_{B(R)}/M\sigma_{b(r)}}$ . Then the radius and harmonic trapping frequency becomes

$$r_0 = \sigma_r \sqrt{\frac{4\kappa_1^2 \ln \kappa_2}{\kappa_1^2 - 1}}, \quad (3.33)$$

$$\omega_r = \omega_R \left[ \left( 1 - \frac{4\kappa_1^2 \ln \kappa_2}{\kappa_1^2 - 1} \kappa_2^{-\frac{2\kappa_1^2}{\kappa_1^2 - 1}} \right) - \kappa_2^2 \left( 1 - \frac{4\kappa_1^4 \ln \kappa_2}{\kappa_1^2 - 1} \kappa_2^{-\frac{2\kappa_1^4}{\kappa_1^2 - 1}} \right) \right]^{\frac{1}{2}}. \quad (3.34)$$

For instance, we choose  $\kappa_1 = 2, \kappa_2 = 1.2$ , then  $r_0 \approx 0.99\sigma_r, \omega_r \approx 0.78\omega_R \Rightarrow$  thickness  $\approx \sqrt{\frac{\hbar}{0.78M\omega_R}} \approx \frac{3.1 \times 10^{-5}}{\sqrt{\omega_R}} m$ , where  $\omega_R$  takes the unit of Hertz. For  $\omega_R = 200\text{Hz}$ , the thickness  $\sim 2.2\mu m$ . Thus, for  $\sigma_r \approx 22\mu m$  we approximately have the radius-thickness ratio for the cylindrical surface as  $R/\sigma = 10$ . These parameters are used to plot the potential  $V(r)$  in Fig. 1.

### 3.2.2 Synthetic gauge fields in Landau gauge

Next, we insert a quadrupolar magnetic field  $\mathbf{B}$  into the center of the cylinder, (see Fig. 3.4),

$$\begin{aligned} \mathbf{B}(\mathbf{x}) &= B_0(x\hat{x} + y\hat{y} - 2z\hat{z}) \\ &= B_0r(\sin\theta \cos\varphi\hat{x} + \sin\theta \sin\varphi\hat{y} - 2\cos\theta\hat{z}). \end{aligned} \quad (3.35)$$

Such a field configuration was used recently in the experiment by Hall's group [98]. Our configuration is a modification of their setup by piercing through the harmonic potential



with a blue-detuned laser. For sufficiently large  $B_o$ , the low energy space is made up of bosons with spin pointing to the direction of the local field  $\mathbf{B}(\mathbf{x})$ . Denoting the direction of the spin as

$$\hat{l} = \cos\beta\hat{z} + \sin\beta(\cos\alpha\hat{x} + \sin\alpha\hat{y}), \quad (3.36)$$

we have

$$\alpha = \varphi, \quad \cos\beta = -\frac{2z}{\sqrt{R^2 + 4z^2}}. \quad (3.37)$$

The condensate wave function of bosons with spin  $S$  is then  $\psi_a(\mathbf{x}) = \zeta_a(\mathbf{x})\phi(\mathbf{x})$ , where  $a$  is the spin index,  $\zeta_a(\mathbf{x})$  is a normalized vector aligned with the local magnetic field, i.e.  $\hat{\mathbf{B}}(\mathbf{x}) \cdot \mathbf{S}_{ab}\zeta_b(\mathbf{x}) = S\zeta_a(\mathbf{x})$ .

The energy functional reads (with spin indices suppressed)

$$E[\psi] = \int d^2x \left[ \frac{\hbar^2}{2M} |\nabla\psi|^2 - (\mu - V(z)) |\psi|^2 + \frac{g}{2} |\psi|^4 \right]. \quad (3.38)$$

Here, we have  $\nabla = \hat{z}\partial_z + R^{-1}\hat{\varphi}\partial_\varphi$ . With  $\zeta_a(\mathbf{x})$  frozen by  $\mathbf{B}(\mathbf{x})$ , (3.38) reduces to a functional of  $\phi(\mathbf{x})$ . The kinetic part becomes

$$|\nabla\psi|^2 = \left| \left( \frac{\nabla}{i} + \frac{\zeta^\dagger \nabla \zeta}{i} \right) \phi \right|^2 + [|\nabla\zeta|^2 + (\zeta^\dagger \nabla \zeta)^2] |\phi|^2. \quad (3.39)$$

Both  $|\nabla\zeta|^2$  and  $(\zeta^\dagger \nabla \zeta)^2$  serve as additional harmonic potential around  $z = 0$ . Near  $z = 0$  they have the effect of a harmonic trap:

$$|\nabla\zeta|^2 + (\zeta^\dagger \nabla \zeta)^2 = \frac{S}{2} \frac{5R^2 + 4z^2}{(R^2 + 4z^2)^2} \approx \frac{S}{2R^2} [5 - 32(z/R)^2]. \quad (3.40)$$

We shall then denote the total harmonic trap along  $z$  as  $V_z = \frac{1}{2}M\tilde{\omega}_z^2 z^2$ . Thus, the system represents scalar charged bosons  $\phi(\mathbf{x})$  moving in synthetic magnetic field, with the gauge potential and field strength

$$\mathbf{A}_{syn} = i\zeta^\dagger \nabla \zeta = S(\nabla\alpha) \cos\beta \approx -\frac{\hat{\varphi}}{R} \frac{2zS}{R}, \quad \mathbf{B}_{syn} = \nabla \times \mathbf{A}_{syn} \approx (2S/R^2)\hat{\mathbf{r}} \quad (3.41)$$

near  $z = 0$ . The strength of the synthetic field is proportional to  $2S$ , so a vortex ground state is expected for condensates with sufficiently large spin. To simplify notations, we measure length in units of  $R$ , so that  $z/R \rightarrow z$ , and  $z$  is now dimensionless. We further introduce the dimensionless variables

$$\tilde{\alpha} \equiv M\bar{\omega}_z R^2/\hbar, \quad \tilde{\mu} \equiv \mu/(\hbar^2/2MR^2), \quad \tilde{g} \equiv g/(\hbar^2/2MR^2), \quad (3.42)$$

then the energy functional becomes  $E[\psi] = \frac{\hbar^2}{2MR^2} \int d^2x \mathcal{E}$ ,

$$\mathcal{E} = |\partial_z \phi|^2 + \left| (-i\partial_\varphi + 2S z) \phi \right|^2 - (\tilde{\mu} - \tilde{\alpha}^2 z^2) |\phi|^2 + \frac{\tilde{g}}{2} |\phi|^4. \quad (3.43)$$

### 3.3 Vortex Physics on a Cylindrical Surface

#### 3.3.1 Lowest Landau Level Limit for Condensates

The physics in the lowest Landau level (LLL) [99] can provide useful physical intuitions. The non-interacting part of the Hamiltonian in Eq. (3.43) is

$$h = -\partial_z^2 + (-i\partial_\varphi + 2S z)^2 + \tilde{\alpha}^2 z^2. \quad (3.44)$$

It describes a charged particle in a magnetic field in the Landau gauge in the presence of a harmonic potential. The eigenstates in the LLL are  $f_m(\varphi, z) = e^{-im\varphi} e^{-\nu(z-z_m)^2/2}$ ,  $z_m = \frac{2S}{\nu} m$ ,  $\nu \equiv \sqrt{4S^2 + \tilde{\alpha}^2}$ , with energy  $\varepsilon_m = \nu + \frac{\tilde{\alpha}^2}{\nu^2} m^2$ . The state  $f_m$  is a ring at  $z_m$  with  $m$  units of circulation around the azimuthal direction. It is useful to rewrite  $f_m$  as

$$f_m(\varphi, z) = C_m w^m e^{-\nu z^2/2}, \quad w = e^{-iu}, \quad u = \varphi + i \frac{2S}{\nu} z \quad (3.45)$$

where  $C_m = e^{-2S^2 m^2/\nu^3}$ . Here,  $u$  is the complex number that represents the point  $(\varphi, z)$ , and  $w$  is the conformal map that takes the cylinder  $(\varphi, z)$  into a 2D plane  $(w_x, w_y)$ . Eq.(3.45) shows  $f_m$  is a simple power of  $w$  apart from the Gaussian in  $z$ .

Due to the trapping potential along  $z$ , the states within LLL are not completely degenerate, and the energy is

$$\varepsilon_m \equiv \mathcal{E}_{0m} = \nu + \frac{\tilde{a}^2}{\nu^2} m^2 \quad (3.46)$$

For non-interacting systems, bosons will condense in the  $m = 0$  state. However, as in the planar case, an increasing repulsive interaction will change the condensate at  $m = 0$  to other linear combination of  $m$  states so as to reduce the repulsion energy. The spacing, the width, and their ratio for states of different  $m$  are

$$\Delta z = \frac{2S}{\nu^2}, \quad \bar{W} = \frac{1}{\sqrt{\nu}}, \quad \frac{\bar{W}}{\Delta \bar{z}} = \frac{\nu^{3/2}}{2S} \quad (3.47)$$

That means one state has density covering  $\nu^{3/2}/2S$  nearby states.

Next we consider the effect of interactions. Expand the many-body wave function in terms of ground state free wave-functions

$$\Psi(z, \varphi) = \sum_{m=0, \pm 1, \dots} C_m \phi_m(z, \varphi), \quad N = \sum_m |C_m|^2. \quad (3.48)$$

We have the GP energy functional:

$$K[C] = \sum_m (\varepsilon_m - \tilde{\mu}) |C_m|^2 + \frac{1}{2} \sum_{[m]} \Gamma_{1234} C_1^* C_2^* C_3 C_4, \quad (3.49)$$

$$\Gamma_{m_1 m_2 m_3 m_4} = \gamma e^{-\frac{S^2}{\nu^3} [(m_1 - m_2)^2 + (m_3 - m_4)^2]} \delta_{m_1 + m_2, m_3 + m_4}. \quad (3.50)$$

Without interaction, all particles will condense in the  $m = 0$  state. Repulsion will cause particles to populate other  $m$  levels to reduce interaction energy. If the population terminates at some state  $m$ , the wave function is

$$\Psi(z, \varphi) = \left( \sum_m B_m \tilde{W}^m \right) e^{-\nu z^2/2}, \quad B_m = DC_m e^{-\frac{2S^2 m^2}{\nu^3}}, \quad \tilde{W} = e^{\frac{2S\bar{z}}{\nu} + i\varphi}, \quad (3.51)$$

Since any polynomial can be written in factorized form, we have

$$\Psi(z, \varphi) = \lambda \prod_n (\tilde{w} - b_n) e^{-\tilde{w}^2/2}, \quad (3.52)$$

and  $b_i$ 's are the location for vortices in  $\tilde{w}$ -space. If only  $-M, \dots, M$  are populated,  $\sum_m B_m \tilde{w}^m = \tilde{w}^{-M} \sum_{l=0, \dots, 2M} B_l \tilde{w}^l$ , so there will be  $2M$  vortices.

One can get the intuition of the vortex pattern through the following simple considerations. If only 2 states being populated, i.e.  $(-M, M)$ ,  $(B_{-M} + B_M w^{2M})$ , so  $b_n$  in Ea.(3.52) is given by  $b_n = (-B_{-M} e^{i2\pi n} / B_M)^{1/2M}$ ,  $n = 0, 1, \dots, (2M - 1)$ . The vortices will then line up with the same  $z$  along the azimuthal direction. This feature can be understood from the fact that the state  $f_m$  has magnitude peak at  $z_m$ , and it carries angular momentum  $m\hbar$ :  $L_z e^{-im\varphi} = -m\hbar e^{im\varphi}$ . As the two different rings are populated, in the region where their wave functions overlap, the flows arises from different rings have different velocities, which will create a shear flow and hence a vortex.

We shall not discuss the vortex transition in the LLL. Instead, we point out that a linear combination of the form  $B_M \phi_M + B_{-M} \phi_{-M}$  amounts to a linear array of  $2\pi$ -vortices, since  $B_M w^M + B_{-M} w^{-M} = B_{-M} w^{-M} \prod_{\ell=1}^{2M} (w - (-\frac{B_{-M}}{B_M})^{1/2M} e^{\pi\ell/M})$ . It is easy to see that a vortex in the  $w$  space is also a vortex in the  $u$  space.

### 3.3.2 Isolated vortex on a cylindrical surface

To bring the discussion closer to current experiments, we consider a gas with  $\sim 10^5$  bosons, which typically occupy many Landau levels. If  $\phi(\varphi, z)$  has a vortex at  $u_j = \varphi_j + i\frac{2S}{\nu} z_j$  with unit circulation, then as  $u \rightarrow u_j$ , it must be of the form  $\phi \propto (u - u_j)$ . On the other hand,  $\phi(\varphi, z)$  must be a linear combination of the basis functions  $\{e^{im\varphi}, m \in \mathbb{Z}\}$  due to the

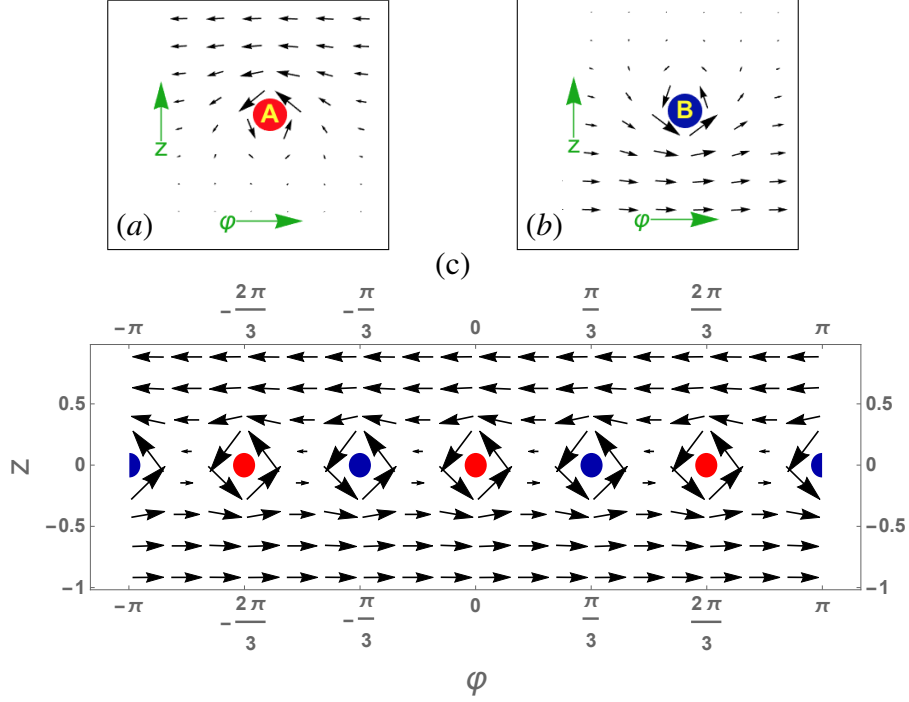


Figure 3.6: Figure (a) and (b) are velocity profiles for the  $A$  and  $B$  vortex respectively. The velocity of the  $A$  (or  $B$ ) vortex reaches a constant above (below) the vortex core and vanishes below (above) it over a distance of  $R$ . Figure (c) shows the velocity profile of a necklace of six alternating  $AB$  vortices. It is equivalent to the velocity profile of two counter circulating superfluid rings.

periodicity along  $\varphi$ . This implies the phase winding of  $\phi(\varphi, z)$  is of the form

$$\phi(\varphi, z) \propto W_j^\pm, \quad W_j^\pm = (e^{\pm iu} - e^{\pm iu_j}); \quad u = \varphi + i\frac{2S}{v}z. \quad (3.53)$$

Their corresponding superfluid velocity are

$$\mathbf{v}_s = \nabla\Theta_j^\pm, \quad \Theta_j^\pm = \arg(W_j^\pm) \quad (3.54)$$

Note that both  $W_j^+$  and  $W_j^-$  have the same  $+2\pi$  circulation, since both reduce to  $u - u_j$  as  $u \rightarrow u_j$ . Their velocity profiles, however, are very different. The gradients

$$\partial_\varphi \Theta_j^\pm = \mp \frac{e^{\pm \frac{2S}{v}(z-z_j)} - \cos(\varphi - \varphi_j)}{2 \left[ \cosh \frac{2S}{v}(z - z_j) - \cos(\varphi - \varphi_j) \right]}, \quad (3.55)$$

$$\partial_z \Theta_j^\pm = \frac{2S}{v} \frac{\sin(\varphi - \varphi_j)}{2 \left[ \cosh \frac{2S}{v}(z - z_j) - \cos(\varphi - \varphi_j) \right]}. \quad (3.56)$$

show that  $\nabla \Theta_j^+$  and  $\nabla \Theta_j^-$  are related by a  $\pi$  rotation about vortex core. Far from the vortex core, they approach a constant on one side and vanish on the other,

$$\nabla \Theta_j^+ \rightarrow \begin{cases} -1 \cdot \hat{\varphi}, & z \gg z_j \\ 0, & z \ll z_j \end{cases}, \quad \nabla \Theta_j^- \rightarrow \begin{cases} 0, & z \gg z_j \\ 1 \cdot \hat{\varphi}, & z \ll z_j \end{cases}. \quad (3.57)$$

as shown in Fig.3.6 (a) and (b). Because of this feature, we refer to  $\Theta_j^+$  and  $\Theta_j^-$  as the *A*- and *B*-vortex as their velocities are mostly non-vanishing ‘‘above’’ and ‘‘below’’ the vortex core respectively. It is easy to see that vortices with  $\ell$ -circulation will also come in two different types,  $(e^{\pm iu} - e^{\pm iu_j})^\ell$ .

The presence of two types of vortices of the same circulation marks a key difference between the cylindrical and the planar BEC. In the latter case, there is one typical vortex with  $+2\pi$  circulation, of the form  $x + iy$ . This difference can be traced back to the conformal map  $w = e^{cu}$  that takes a 2D plane  $(w_x, w_y)$  into a cylinder  $(\varphi, z)$ , and  $c$  is a complex number that describes the change in scale and orientation of the cylindrical strip with respect to  $(w_x, w_y)$ -plane. However, since the wave function of the BEC is made up of the basis functions  $\{e^{im\varphi}\}$ ,  $c$  can only be  $\pm i$  for vortices of unit circulation, reducing the infinite number of mapping down to 2. The periodicity of the basis function, which exists in all Landau levels, reflects the underlying topology of the cylindrical surface.

### 3.3.3 Vortex array on a cylindrical surface

The condensate wavefunction is  $\phi = \sqrt{n} \exp(i\Theta)$ , where  $n$  is the density profile and  $\Theta$  is its phase function. For a condensate containing vortices, its wave function can be approximated as  $\sqrt{n} = \sqrt{n_{TF}} f$ , where  $n_{TF}$  is the Thomas-Fermi (TF) density profile in the absence of vortices, and  $f$  is a function that is 1 everywhere except within a region of the size of the coherence length around the vortex singularity. In our calculations, we shall use the variational form

$$f(u) = \prod_j \tanh \frac{|u - u_j|}{\xi} \quad (3.58)$$

for a system with vortices located at  $u_j$ , where  $\xi$  is the core size, also written in units of  $R$ . This form has been shown to match well with experiment for rotating gases [100]. For a condensate with  $A$ -vortices at points  $(\{u_j, j = 1, \dots, Q\})$  and  $B$ -vortices on another set of points  $(\{u_{j'}, j' = 1, \dots, Q'\})$ , we take the following variational form of phase function  $\Theta$ ,

$$\exp(i\Theta) = W/|W|, \quad W = \prod_{j=1}^Q W_j^+ \prod_{j'=1}^{Q'} W_{j'}^-. \quad (3.59)$$

The entire variational wave function is therefore specified by the total particle number (which fixes the chemical potential and hence  $n_{TF}$ ), and the location of vortices.

With the variational wavefunction  $\phi = \sqrt{n_{TF}} f \exp(i\Theta)$ , the energy in Eq.(3.38) becomes a function of the coordinates  $(\varphi_j, z_j)$  of the vortices. We have searched for the minimum of this function numerically by varying the vortex locations. Since the system has reflection symmetry in  $z$ -direction,  $A$  and  $B$  vortices must appear in pairs at appropriate location to respect this symmetry. Our results are shown in Fig. 3.7. We have found that for  $S \leq 4$ , the gauge field is not strong enough to generate vortices in the ground state. For  $S = 5, 6, 7, 8$ , there are 4, 6, 8, 10 vortices respectively lying on the circle at  $z = 0$  (i.e.  $z_j = 0$ ). These “necklaces” of vortices are all in the alternating pattern  $A-B-A-B-\dots$  with equal spacing.

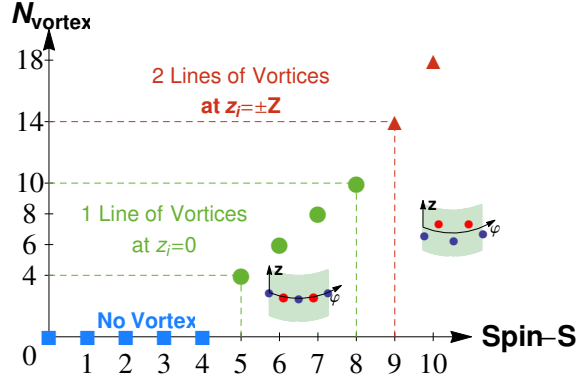


Figure 3.7: For  $S \leq 4$ , the ground state contains no vortex. Within  $S = 5, 6, 7, 8$ , the vortices aligned in one row at  $z_i = 0$  with the pattern A-B-A-B. For  $S \geq 9$ , the vortices array splits into two rows centering at  $z_i = \pm Z$ , with all A vortices aligned in one row and all B vortices in another.

For  $S \geq 9$ , the vortices split into two rows, with the A-vortices shifted above and B-vortices shifted below  $z = 0$ .

The reason that the vortex pattern is so different from the planar case is a consequence of the confining geometry (lack of trapping potential along  $\varphi$  direction). We can see the connection of the necklace pattern to the usual hexagonal pattern in the following hypothetical process. Assuming  $S$  can be increased continuously, the vortices will grow in number and will split into more and more necklaces. The hexagonal array is the limit where the number of necklaces approaches the number of vortices within one necklace. The  $S = 9$  example in Fig. 3.7 can be viewed as a tendency towards the hexagonal lattice limit.

To conclude, we examine the phase function and velocity field of the alternating vortex row in greater detail. Let us consider the case of  $S = 6$  (corresponding to  $^{168}\text{Er}$ ) where the ground state has a necklace of 6 equally spaced, alternating A and B vortices at  $z = 0$  and  $\varphi = n\frac{2\pi}{6}$ , where  $n = 0, 1, \dots, 5$ . Defining  $w = e^{iu} = e^{i\varphi - \frac{2S}{v}z}$ , and  $\alpha = e^{2\pi/6}$ , the phase



function  $W$  in Eq.(3.59) is

$$W = \prod_{n=0,1,2} [(w - \alpha^{2n})(w^{-1} - \alpha^{-(2n+1)})] = w^3 - w^{-3} \quad (3.60)$$

The wave function is then

$$\phi(\varphi, z) \sim \sqrt{1 - z^2} f(\varphi, z) \frac{e^{3i\varphi - 3z\frac{2S}{v}} - e^{-3i\varphi + 3z\frac{2S}{v}}}{|e^{3i\varphi - 3z\frac{2S}{v}} - e^{-3i\varphi + 3z\frac{2S}{v}}|}. \quad (3.61)$$

For  $z > 0$  ( $z < 0$ ),  $\phi(\varphi, z)$  quickly approaches  $e^{-3i\varphi}$  ( $e^{3i\varphi}$ ). The system is essentially two counter-circulating superflows above and below  $z = 0$ , as shown in Fig.2(c).

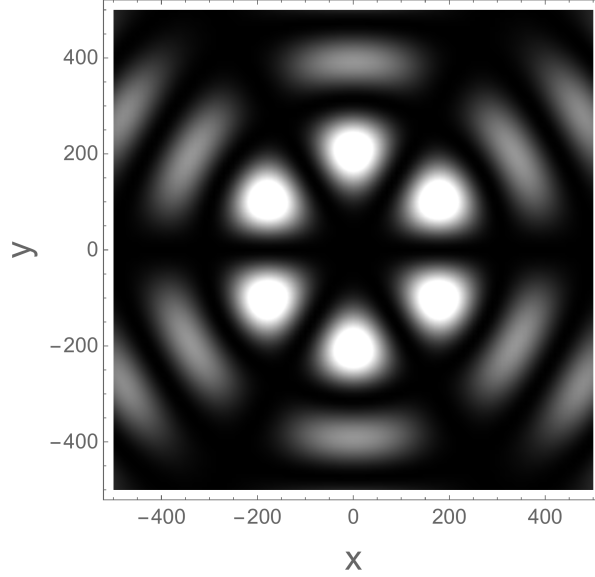


Figure 3.8: The time-of-flight image of the vortex row in figure 2(c), taken at the time  $t$  such that  $x_o/R = \sqrt{\hbar t/m}/R = 7$  on the  $x$ - $y$  plane at  $z = 0$ . Length is measured in units of  $R$ . The  $2n$ -fold symmetry of the image reflects the number of vortices in the vortex row.

### 3.3.4 Experimental Signatures

The presence of these alternating vortex array can be detected in time-of-flight experiments. As we have discussed, a necklace of  $2n$  vortices will generate two counter phase

superflow  $e^{-in\varphi}$  and  $e^{+in\varphi}$  for  $z > 0$  and  $z < 0$ . The system can be approximated by two rings of condensates with opposite circulation, with one ring sitting above the other along  $z$  with a separation of the order of their radius  $R$ . In the time-of-flight experiment, these two rings will produce an interference at the  $z = 0$  plane of the form  $e^{-in\varphi} + e^{+in\varphi}$  and exhibit a density pattern with  $2n$ -fold symmetry. This effect is in fact found in an explicit calculation of the ballistic expansion of the vortex row condensate in Eq.(3.61). The time evolution of the condensate is given by

$$\phi(\mathbf{x}, t) = \int_{-1}^1 dz \int_{-\pi}^{\pi} d\varphi U(\varphi, z, t; \varphi', z') \phi(\varphi', z'). \quad (3.62)$$

where  $U(\varphi, z, t; \varphi', z')$  is the Green's function for free particle propagation at large distance and at long times in cylindrical coordinates,

$$U(\varphi, z, t; \varphi', z') \approx \exp \left[ -i(Rr \cos(\varphi - \varphi') + (\frac{2S}{v})^2 z z') / x_0^2 \right], \quad (3.63)$$

and  $x_0 = \sqrt{\hbar t / m}$ . The density pattern at the equatorial plane  $z = 0$  at long times is shown in Fig.4. Experimentally, the density of the expanded cloud in the equatorial plane (at  $z = 0$ ) can be measured by first using a sheet of light to excite the original atoms (denoted as “ $a$ ”) in this plane to a different atomic state (say, “ $b$ ”), and then imaging the atoms in the  $b$  state afterwards.

### 3.4 Conclusions and Outlook: General Compact Surfaces

The emergence of two kinds of vortices with identical vorticity in a cylindrical manifold is a new feature of Bose condensates in a cylinder. It is a consequence of the topological constraint on the single valueness of the wave function (i.e. that forces the spatial dependence to be expressed in terms of  $e^{in\varphi}$ ), which will persist even when the manifold is deformed. Although we focus on a particular aspect of the quantum gas in curved surfaces,

there is a lot more to explore especially for systems with greater complexity. Realization of quantum gases in curved surfaces will surely open an exciting direction for cold atom research. In the following we extend the topic to other types of surfaces, and briefly discuss the rich physics associated with them.

### 3.4.1 Tentative Schemes for Spherical and Toroidal Surfaces

In this subsection, we tentatively propose the schemes for trapping quantum gases on spherical and toroidal surfaces. The methods described below are all based on current technology in cold atom experiments, so the schemes should have a good chance to be realized in the future.

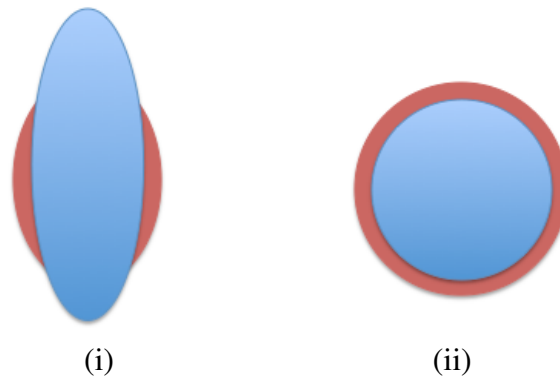


Figure 3.9: The equal-potential line of blue-detuned and red-detuned lasers in the  $x$ - $z$  plane for (i) cylindrical surfaces, (ii) spherical surfaces. The two schemes differ in the Gaussian width of the blue-detuned laser along  $z$ -direction, which can be tuned by changing the focal length of the convex lens for the blue laser.

A spherical surface can be engineered by directly generalizing the scheme for cylindrical surface. In the previous discussions for cylindrical surfaces, we chiefly focus on the  $x$ - $y$  plane where a ring-shaped potential is engineered. In the  $x$ - $z$  plane, the trapping potentials

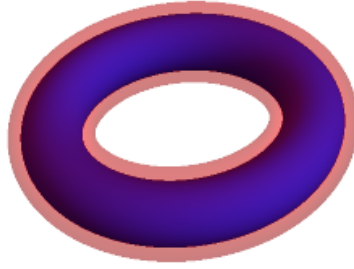


Figure 3.10: Toroidal surface produced by a attractive ring-shaped potential superposed with a repulsive ring-shaped potential.

are highly anisotropic. In particular, the blue-detuned laser has a much larger Gaussian width along  $z$  compared with the red-detuned laser, see Fig.3.9, so it penetrates a hole in the center. On the other hand, if we reduce such an anisotropy for blue-detuned laser, we directly end up with a ring-shaped potential minimum along all of the three directions — that is, a confining potential for a spherical surface. Furthermore, we can similarly put in synthetic gauge fields by using a quadrupolar magnetic field to polarize the spins.

A toroidal surface is more sophisticated to engineer, but should be also within the capability of current technology. To do so, we need to superpose a pair of ring-shaped potentials on top of each other, see Fig.3.10. A thinner repulsive ring-shape potential resides inside an attractive ring-shape potential, and the quantum gases will be confined on a toroidal surface.

In current experiments there exist two ways to engineer a ring-shape potential. One widely used method is similar to the one for cylindrical trap described earlier (i.e. see the experimental thesis [101], and recent experiments [1, 102]). It amounts to reducing the height of the cylinder in Fig. 3.9 (i), i.e. reducing the Gaussian width of the red-detuned

laser along  $z$ . That is, we first have an anisotropic "pancake"-like trapping potential produced by red-detuned laser, and then we penetrate a hole at the center using blue-detuned laser, see Fig. 3.11(ii). The advantage of this method is that the radius and thickness of the ring can be changed separately, which gives good tunability for the shape of the trap. Another method is to employ a so-called Laguerre-Gaussian (LG) laser beam [103–105], which is a laser mode of certain orbital angular momentum. It is denoted by two quantum numbers  $(l, p)$ , with the intensity in the x-y plane shown in Fig.3.11(i). For simplicity, we focus on the modes  $p = 0$ ; then the electric-field component of the laser is (with  $e^{-i\omega t}$  omitted)

$$E_l(r, \phi, z) \propto r^{|l|} e^{-\frac{r^2}{w^2(z)}} e^{il\phi} e^{-ikz}. \quad (3.64)$$

Its intensity peak has the shape of a tube along  $z$ . Then, it is clear that if one superpose a pair of LG laser beams with the same  $l$  counter-propagating along  $z$ -direction, the net intensity

$$I(r, z) = |E_l(r, \phi, z) + E_l(r, \phi, -z)|^2 \propto r^{2|l|} e^{-\frac{r^2}{w^2(z)}} \cos^2(kz) \quad (3.65)$$

has the shape of rings at  $z_0 = 0, \pm \frac{\pi}{k}, \dots$ . Furthermore, the fact that the LG beams carry orbital angular momentum enables the possibility of imparting synthetic gauge field to the quantum gases through Raman coupling [106]. In sum, by suitably applying both methods, we should be able to trap quantum gases on a toroidal surface with synthetic gauge fields.

### 3.4.2 Vortices on Compact Surfaces: Hopf-Poincaré Index Theorem

As we have seen in previous sections, the vortex physics changes qualitatively when quantum gases are placed on cylindrical surfaces. For compact surfaces (surfaces without boundaries such as the spherical and toroidal surfaces), their vortex physics has a further fundamental difference from that on a planar geometry. Consider a vector field  $\mathbf{v}$  tangent

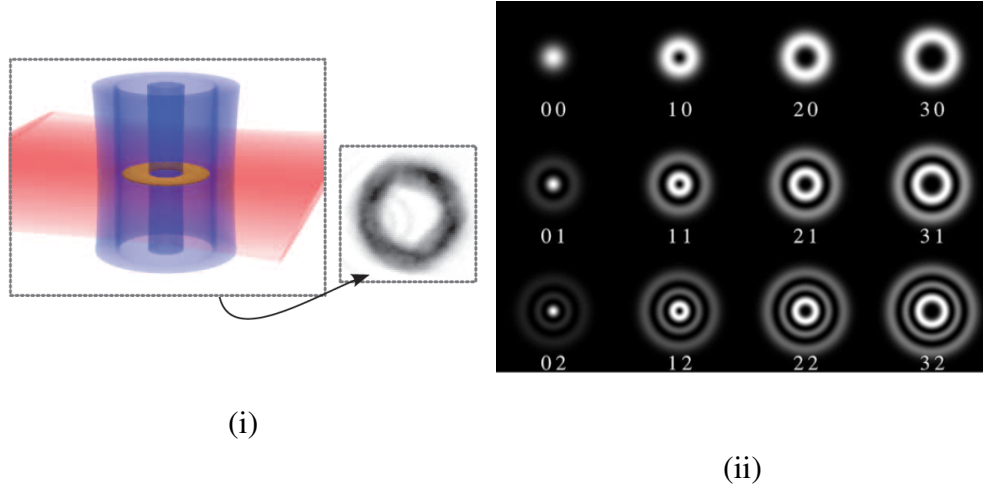


Figure 3.11: Two ways to produce ring-shape potentials. (i) The ring-shape trapping potential used in the experiment c.f. [1] (this figure is taken from the reference). It is produced by superposing red and blue detuned lasers similar to the scheme for cylindrical trap in Fig. 3.9 (i). (ii) Intensity of Laguerre-Gaussian beam in x-y plane for modes  $(l, p)$ .

to the 2D surface that is continuous and is non-vanishing except on isolated points. Such a vector field can represent the velocity field of the superfluid  $\mathbf{v}_s = \frac{\hbar}{m} \Psi^* \nabla \Psi$ , where  $\Psi$  is the order parameter. The total vorticity (or total circulation number)

$$\Gamma = \sum_i \Gamma_i = \oint \mathbf{v}_s \cdot d\mathbf{l} \quad (3.66)$$

of the vector field on a planar geometry can take arbitrary values in general. However, on compact surfaces, the Hopf-Poincaré theorem [107–109]

$$\Gamma = \chi(M). \quad (3.67)$$

relates the total circulation to the Euler characteristic

$$\chi(M) = 2(1 - g) \quad (3.68)$$

of the surface manifold  $M$ , where  $g$  is genus. For instance, a spherical surface  $S^2$  has genus  $g = 0$ , so the total circulation must be 2 for any continuous vector field tangent to  $S^2$ . But a torus has genus  $g = 1$ , so there could be a continuous vector field without any pole on a torus. Further, if there are vortex excitations, they must appear in terms of vortex-antivortex pairs to ensure the total circulation is 0. Moreover, since the Euler characteristic is a topological number, such constraint persists even if the 2D surface is distorted — so long as such distortion does not change the topology.

## 3.5 Appendix

### 3.5.1 Synthetic Abelian and Non-Abelian Gauge Fields

Here we derive the effective energy functional (3.43) for  $\phi$  from the functional (3.38) for  $\psi = \zeta\phi$ , with the spins  $\zeta$  polarized by a quadrupolar magnetic field. The kinetic part of the Hamiltonian is (we have also put in a quadratic Zeeman term for generality, though in the main text we work in the regime where  $\lambda_1$  dominates)

$$T = \frac{p^2}{2M} - \lambda_1 \hat{n} \cdot \mathbf{S} + \lambda_2 (\hat{n} \cdot \mathbf{S})^2 \quad (3.69)$$

where  $\hat{n}$  is the direction of local magnetic field. (Here the  $\hbar$ 's are factored out from spin operators so they are dimensionless). Denotes it as  $(\beta(\varphi, z), \alpha(\varphi, z))$ , that is

$$\mathbf{B} = b_0 \hat{n}, \quad \hat{n} = (\sin \beta \cos \alpha, \sin \beta \sin \alpha, \cos \beta). \quad (3.70)$$

Consider the unitary transform  $U_1 = e^{iS_z \alpha}$ . It rotates the spin with respect to  $\hat{z}$  by  $-\alpha$ , and

$$U_1 \partial_j U_1^\dagger = \partial_j - iS_z (\partial_j \alpha) \quad (3.71)$$

Further,  $U_2 = e^{iS_y \beta}$  rotate the spin along  $\hat{y}$  by  $-\beta$ , and

$$U_2 (U_1 \partial_j U_1^\dagger) U_2 = \partial_j - iS_y (\partial_j \beta) - i(S_z \cos \beta - S_x \sin \beta) (\partial_j \alpha). \quad (3.72)$$

On the other hand,

$$U_2(U_1\hat{n} \cdot \mathbf{S}U_1^\dagger)U_2^\dagger = S_z \quad (3.73)$$

Thus, such consecutive rotations transform the kinetic part into

$$T \rightarrow \frac{\hbar^2}{2M} \left[ -i\nabla - S_y\nabla\beta - (S_z \cos\beta - S_x \sin\beta)\nabla\alpha \right]^2 - \lambda_1 S_z + \lambda_2 S_z^2 \quad (3.74)$$

Depending on the functional form of  $(\beta, \alpha)$ , we can have different types of spin-orbit coupling. One subtlety is the spin directions:  $S_z$  is now pointing to the direction of local magnetic field, and  $(S_x, S_y, S_z)$  form a right-handed coordinate system.

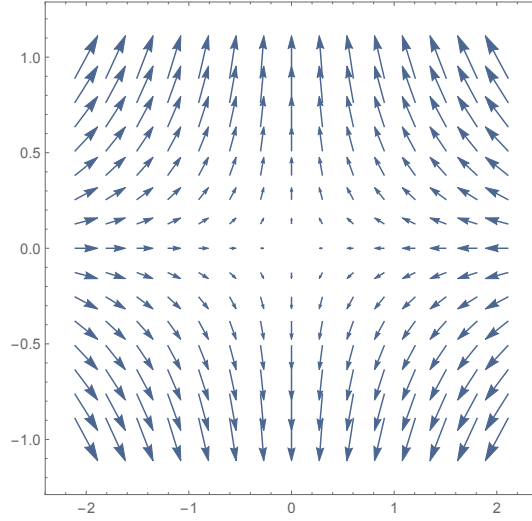


Figure 3.12: Quadrupolar field in the x-z plane.

Now, consider a quadrupolar magnetic field

$$\mathbf{B} = b_0(-x, -y, 2z) = b_0(-R \cos \varphi, -R \sin \varphi, 2z), \quad (3.75)$$

as illustrated in Fig.3.12. We have

$$\cos\beta = \frac{2z}{\sqrt{R^2 + 4z^2}}, \quad \alpha = \varphi + \pi, \quad (3.76)$$



On a cylindrical surface,  $\nabla = \hat{z}\partial_z + (\hat{\varphi}/R)\partial_\varphi$ , so

$$\nabla\beta = \hat{z}\frac{-2R}{R^2 + 4z^2}, \quad \nabla\alpha = \frac{\hat{\varphi}}{R}, \quad \sin\beta = \frac{R^2}{\sqrt{R^2 + 4z^2}}. \quad (3.77)$$

Further, measure length in the unit of  $R$ , i.e.  $z/R \rightarrow z$  and  $z$  is now dimensionless,

$$T = \frac{\hbar^2}{2MR^2} \left[ \left( -i\partial_z + S_y \frac{2}{1 + 4z^2} \right)^2 + \left( -i\partial_\varphi + S_x \frac{1}{\sqrt{1 + 4z^2}} - S_z \frac{2z}{\sqrt{1 + 4z^2}} \right)^2 \right] - \lambda_1 S_z + \lambda_2 S_z^2. \quad (3.78)$$

At  $z = 0$ ,

$$T|_{z=0} = \frac{\hbar^2}{2MR^2} \left[ (-i\partial_z + 2S_y)^2 + (-i\partial_\varphi + S_x)^2 \right] - \lambda_1 S_z + \lambda_2 S_z^2. \quad (3.79)$$

To lowest order in  $z$ , as approximated in previous work,

$$T|_{\text{near } z=0} = \frac{\hbar^2}{2MR^2} \left[ (-i\partial_z + 2S_y)^2 + (-i\partial_\varphi + S_x - 2zS_z)^2 \right] - \lambda_1 S_z + \lambda_2 S_z^2. \quad (3.80)$$

The previous case corresponds to large Zeeman splitting, where the system stays in  $|m_F = F\rangle$  state, and the projection to that state gives  $\langle F|S_x|F\rangle = 0 = \langle F|S_y|F\rangle$ ,  $\langle F|S_z|F\rangle = F$ , and the kinetic part reduces to the previous Abelian case.

### 3.5.2 Details of the Variational Calculation

Our variational wave function is

$$\phi = \sqrt{n_{TH}} f h, \quad h = e^{i\Theta}, \quad (3.81)$$

where  $n_{TH}$  is the Thomas Fermi density profile, which is fixed by the trapping potential.  $f$  is the function that describes the location of vortex core and  $\Theta$  is the phase function of the vortex state. The expression of  $\Theta$  is given in Eq. (15) and the expression of  $n_{TH}$  will be given below. We shall consider  $M$  A-type vortices located at  $\{(\varphi_i, z_i), i = 1, \dots, N\}$ , and  $M'$  B-type vortices located at  $\{(\varphi_i, z_i), i = N + 1, \dots, N + M'\}$ . The entire set of vortex coordinates

$\{(\varphi_i, z_i), i = 1, \dots, M + N\}$  are the variational parameters. In the calculations we have taken  $2S/\nu \rightarrow 1$ , as  $\tilde{\alpha} \sim 1$  (for typical experimental parameters), and  $\nu \rightarrow 2S$ .

Substitute the Eq.(3.81) into the energy functional, we have

$$E[\psi] = \frac{\hbar^2}{2MR^2} \int d^2x \mathcal{E},$$

$$\mathcal{E} = |\partial_z \phi|^2 + \left| (-i\partial_\varphi + 2Sz) \phi \right|^2 - (\tilde{\mu} - \tilde{\alpha}^2 z^2) |\phi|^2 + \frac{\tilde{g}}{2} |\phi|^4, \quad (3.82)$$

we have

$$\mathcal{E} = \mathcal{E}_1 + \mathcal{E}_2 + \mathcal{E}_3, \quad (3.83)$$

$$\mathcal{E}_1 = \left[ (\partial_z \Theta)^2 + (\partial_\varphi \Theta + 2Sz)^2 \right] n_{TH} f^2 \quad (3.84)$$

$$\mathcal{E}_2 = -n_{TH} f \nabla^2 f - \tilde{g} n_{TH}^2 \left( f^2 - \frac{f^4}{2} - \frac{1}{2} \right) - \frac{\tilde{g} n_{TH}^2}{2} \quad (3.85)$$

$$\mathcal{E}_3 = \left[ (\nabla \sqrt{n_{TH}})^2 - (\tilde{\mu} - V(z)) n_{TH} + \frac{\tilde{g}}{2} n_{TH}^2 \right] f^2 \quad (3.86)$$

We recognize that  $\mathcal{E}_3$  has the form of usual Gross-Pitaevskii energy functional, and determines the density profile in the absence of vortices. In the Thomas-Fermi regime, where the gradient term in  $\mathcal{E}_3$  is small, the integral is almost a constant and changes little due to variation of the vortex positions. Thus,  $\mathcal{E}_3$  can be set to zero, and the density is well approximated by

$$n_{TH}(z) = \frac{\mu - V(z)}{g} = \frac{M\omega^2 R^2}{2g} (Z_{\max}^2 - z^2), \quad g = \frac{4\pi\hbar^2 a_s}{M} \quad (3.87)$$

where  $a_s$  is the scattering length, and  $Z_{\max} = \sqrt{2\mu/M\omega_z^2 R^2}$  is the extent of the condensate along  $z$ . Taking the condensate to be homogeneous along radial direction, the total number of particles is given by

$$N = (2\pi\sigma) \int_{-Z_{\max}}^{Z_{\max}} dz n_{TH}(z). \quad (3.88)$$

This gives the relation between particle number  $N$  and the extent of the condensate in the  $z$ -direction,  $Z_{\max}$ ,

$$N = \frac{Z_{\max}^3}{3} \times \frac{\tilde{\alpha}^2}{a_s/\sigma}, \quad \text{Recall: } \tilde{\alpha} = R^2/d^2, \quad d = \frac{\hbar}{M\omega_z} \quad (3.89)$$

where  $a_s$  is the scattering length related to  $g$  by  $g = \frac{4\pi\hbar^2 a_s}{M}$ .

With  $\mathcal{E}_3 = 0$ , we are left with  $\mathcal{E}_1$  and  $\mathcal{E}_2$ . In the absence of vortices,  $f = 1$  everywhere, and the first two terms in  $\mathcal{E}_2$  vanishes. These two terms then describe the energy increase due to the existence of vortices. To evaluate them, we note that the core size of the vortex at  $z$  is given by the local coherence length  $\xi \sim \frac{\hbar}{\sqrt{2Mn(z)g}} \frac{1}{R}$ . At the center of the trap,  $z = 0$ , we have  $\xi_0 \sim \frac{1}{\tilde{\alpha}}$ . In our calculation, we take the harmonic length  $d$  along  $z$  to be an order of magnitude smaller than  $R$ , then we have  $\xi \sim 10^{-2} \ll 1$ .

Hence, the first two terms in  $\mathcal{E}_2$  are only non-zero close to each vortex core. If  $f_1(x)$  is a smooth function, and  $f_2(x)$  is only non-zero within a small region around  $x_i$ 's, we then make the approximation  $\int_{a_1}^{a_2} dx f_1(x) f_2(x) = (\sum_i f_1(x_i)) \int_{-\infty}^{\infty} dx f_2(x)$ . Using this approximation, we have

$$\int d^2x \mathcal{E}_2 = -\frac{2\pi\tilde{\alpha}^2}{3} + (2 + \tilde{\alpha}^2\xi^2)C \sum_i (Z_{\max}^2 - z_i^2), \quad (3.90)$$

where  $C = \frac{\pi}{6}(4 \ln 2 - 1) \approx 0.928$  is the integration result, and  $z_i$  is the  $z$  coordinates of vortices, which is confined to  $|z_i| < Z_{\max}$ . Dropping the constant term in Eq.(3.90), which plays no role in our variational calculation, the energy  $E$  (in units of  $\frac{M\omega^2 R^4}{2g}$ ) can be written as

$$E[\psi] = (2 + \tilde{\alpha}^2\xi^2) \sum_i (1 - z_i^2) + \int_{-\pi}^{\pi} d\varphi \int_{-Z_{\max}}^{Z_{\max}} dz \times \left[ (\partial_z \Theta)^2 + (\partial_\varphi \Theta + 2S z)^2 \right] (Z_{\max}^2 - z^2) f^2. \quad (3.91)$$

This is now a function of the coordinates of the vortices  $\{(\varphi_i, z_i), i = 1, 2, \dots, 2N\}$ , which are contained in the phase function  $\Theta$ . We have performed numerical calculations for different number of A-types and B-types of vortices. The result presented in the main text is for the case  $\tilde{\alpha}\xi = 1$  and  $Z_{\max} = 1$ . However, our result is remains unchanged with other similar parameters.

## Chapter 4: HALL VISCOSITY AND ITS SIGNATURES IN DENSITY RESPONSE FUNCTIONS

### 4.1 Introduction

This chapter investigates another topic related to the geometric effects on quantum fluids, which is the Hall viscosity  $\eta_H$  (or “Lorentz shear modulus”) [110–112]. It is the third viscosity coefficient unique in 2-dimensional isotropic, parity-odd systems. Unlike the usual shear and bulk viscosity, Hall viscosity causes neither dissipation nor entropy increase, and therefore can be defined down to zero temperature. Like Hall conductivity, Hall viscosity bears lots of topological information. It can be regarded as the Berry curvature in the parameter space of a metric tensor [110], and is proportional to the Wen-Zee shift [113, 114], a quantity characterizing the system’s spatial topology [69].

Besides the topological significance, the influence of Hall viscosity on various systems shows up in multiple ways. As discovered recently, for integer quantum Hall systems [115] and Laughlin wave functions [116], the Hall viscosity is related to the density response to the variation of the sample’s scalar curvature. It acts as an anomalous force on vortices and changes their streamlines in an eulerian vortex fluid [117]. More generally, the Hall viscosity appears in the low-momentum expansion of Hall conductivity  $\sigma_H(q)$  for Galilean invariant systems subject to inhomogeneous electric field [118, 119]. Clearly, studying

these physical consequences not only broadens our perspective on Hall viscosity, but also facilitates designing experiments to measure it.

This chapter is devoted to the discussions of basic concepts and characters of Hall viscosity, and point out its signatures in the density response to external fields. Since density mapping [67] or scattering experiments [120] are practical tools for measurements in cold atom systems, this study may pave the way for future measurements of Hall viscosity in cold atom systems. In the following we first review some of the basic concepts about Hall viscosity.

### 4.1.1 Hydrodynamics

For ideal fluids, we have

- Continuity:  $\frac{\partial}{\partial t} \int n dV = - \oint n \mathbf{v} \cdot d\mathbf{S} = - \int \nabla \cdot (n \mathbf{v}) dV,$

$$\frac{\partial n}{\partial t} + \nabla \cdot (n \mathbf{v}) = 0 \quad (4.1)$$

- Stokes equation for force:  $\int mn \frac{d\mathbf{v}}{dt} dV = - \oint P d\mathbf{S} + \int \mathbf{F} dV = \int (-\nabla P + \mathbf{F}) dV,$  and

note  $\frac{d}{dt} = \frac{\partial}{\partial t} + \frac{dx_i}{dt} \frac{\partial}{\partial x_i} = \partial_t + \mathbf{v} \cdot \nabla,$

$$mn \left( \frac{\partial}{\partial t} + \mathbf{v} \cdot \nabla \right) \mathbf{v} = -\nabla P + \mathbf{F}. \quad (4.2)$$

Here  $\mathbf{F}$  is external force density, i.e.  $\mathbf{F} = en(\mathbf{E} + \mathbf{v} \times \mathbf{B})$  for Lorentz force.

- Navier-Stokes equation for momentum:

$$\int m \frac{\partial(nv_i)}{\partial t} dV = \int m \left[ \frac{\partial n}{\partial t} v_i + \frac{\partial v_i}{\partial t} n \right] dV = m \int dV \left[ -\partial_j (nv_j) v_i - n \left( \frac{\partial_i P - F_i}{mn} + v_j \partial_j v_i \right) \right] \quad (4.3)$$

Thus,

$$m \frac{\partial(nv_i)}{\partial t} + \partial_j \tau_{ij} = F_i, \quad \tau_{ij} = P \delta_{ij} + mn v_i v_j \quad (4.4)$$

where  $\tau_{ij}$  is the momentum flux tensor.

The viscosity serves as a force on interfaces of fluid layers,  $\int F_i^{visc} dV = \oint \sigma_{ij} dS_j = \int \partial_j \sigma_{ij} dV$ , so it can be written as a total divergence of a stress tensor  $\sigma_{ij}$ . It can always be symmetrized.

The form of this tensor can be determined by physical considerations: 1) A constant flow would not reveal viscosity, so it depends only on  $\partial_i v_j$  or higher gradients. For slow varying velocity field, higher gradients are neglected. So  $\sigma_{ij}$  has the general form  $A_{ij} \partial_i v_j$ . 2) A constant rotation,  $v_i = \epsilon_{ijk} \Omega_j r_k$ , also cannot reveal viscosity, because the fluid rotates like a rigid body in this case. So  $0 = A_{ij} \partial_i \epsilon_{jkl} \Omega_k r_l = \epsilon_{ijk} A_{ij} \Omega_k$ . Since  $\Omega_k$  is an arbitrary constant, we need  $A_{ij} = A_{ji}$ . So it only depends on combinations of

$$v_{ij} \equiv \frac{1}{2}(\partial_i v_j + \partial_j v_i). \quad (4.5)$$

In sum, the Navier-Stokes equation for viscous flow can be written as

$$\frac{\partial g_i}{\partial t} + \partial_j \tau_{ij} = F_i^{ext}, \quad (4.6)$$

$$g_i = mnv_i \quad (4.7)$$

$$\tau_{ij} = P\delta_{ij} + mnv_i v_j - \sigma_{ij}, \quad \sigma_{ij} = \eta_{ijkl} v_{kl}, \quad (4.8)$$

where  $g_i$  is momentum,  $\sigma_{ij}$  is the viscous part of stress tensor<sup>4</sup> and the viscosity tensor  $\eta_{ijkl}$  is symmetric under  $i \leftrightarrow j, k \leftrightarrow l$ . It can be decomposed into symmetric and anti-symmetric part for exchange of the pair  $(ij) \leftrightarrow (kl)$ :

$$\eta_{ijkl}^S = \frac{1}{2}(\eta_{ijkl} + \eta_{klij}), \quad \eta_{ijkl}^A = \frac{1}{2}(\eta_{ijkl} - \eta_{klij}). \quad (4.9)$$

<sup>4</sup>There could be an elastic term  $\sigma_{ij} = \lambda_{ijkl} u_{kl} + \eta_{ijkl} v_{kl}$ , with  $u_{kl}$  the strain,  $\partial u_{kl} / \partial t = v_{kl}$ . We neglect this term temporarily and will restore it later on. For a fluid, the only elasticity comes from the compression,  $\sigma_{ij} = \kappa^{-1} \delta_{ij} \delta_{kl} u_{kl}$ , with  $\kappa^{-1}$  is the inverse compressibility. We will consider it in the linear response approach.

Onsager's relation implies that under time-reversal,  $\eta^S$  is even while  $\eta^A$  is odd, i.e. in the presence of external magnetic field,  $\eta^S(-B) = \eta^S$ ,  $\eta^A(-B) = -\eta^A(B)$ . It means that the odd viscosity is only present in time-reversal breaking systems.

### 4.1.2 Dissipation

If some force does work on the fluid, we sum over such work over the whole fluid and see whether it is non-zero. If not, the kinetic energy of the fluid will change. In the case of viscous flow, such change corresponds to dissipation.

Specifically, the viscous force acting upon each fluid element is  $\partial_j \sigma_{ij} dV$ . The displacement of the fluid  $u_i$  is varied, corresponding to work done on the fluid which increases total energy

$$\begin{aligned} \int \delta \epsilon dV &= \int (\partial_j \sigma_{ij}) \delta u_i dV \\ &= \int \partial_j (\sigma_{ij} \delta u_i) dV - \int \sigma_{ij} \partial_j \delta u_i dV. \end{aligned} \quad (4.10)$$

The first term is a total derivative and can be evaluated on the surface of the fluid. Consider the surface effect negligible, and use the symmetry of  $\sigma_{ij}$ ,

$$\delta \epsilon = -\sigma_{ij} \delta u_{ij} \quad (4.11)$$

where

$$u_{ij} = \frac{1}{2} (\partial_i u_j + \partial_j u_i) \quad (4.12)$$

is the strain, and  $\partial u_{ij} / \partial t = v_{ij}$ . Using (4.8), and vary the both sides with respect to time  $t$ ,

$$\dot{\epsilon} = -\eta_{ijkl} v_{ij} v_{kl}. \quad (4.13)$$

This shows that only the symmetry part  $\eta^S > 0$  causes dissipation.



Further look at entropy change due to viscosity. The energy under concern is the mechanical energy (kinetic+potential), which equals the maximum amount of work that can be done when the fluid passes from a given non-equilibrium state to equilibrium. According to thermodynamics, the maximal work can be done through an entropy preserving process (reversible). Denote  $E_0$  the initial energy in a non-equilibrium state, and  $E(S)$  the final equilibrium state with entropy  $S$ . Then

$$E_{mech} = E_0 - E(S). \quad (4.14)$$

The time evolution is then

$$\dot{E}_{mech} = -\frac{\partial E(S)}{\partial S} \dot{S} = -T_0 \dot{S}. \quad (4.15)$$

Here  $T_0$  is the temperature that the system would have if it were in equilibrium with entropy  $S$ . Combined with (4.13),

$$T_0 \dot{S} = \eta_{ijkl} v_{ij} v_{kl}. \quad (4.16)$$

Again, we see that only the symmetric part  $\eta^S$  increases the entropy. Thus, the odd viscosity is allowed to exist even down to zero temperature.

### 4.1.3 Independent Components

Due to symmetry of indices, the independent components of  $\eta_{ijkl}$  is significantly reduced. We further express those components in representations in which it is easier to analyze their rotation properties.

#### 2D

In 2D, we use the representation

$$\eta_{ijkl} = \eta_{AB} (\sigma^A)_{ij} \otimes (\sigma^B)_{kl}, \quad i, j = x, y; A, B = 0, 1, 3. \quad (4.17)$$

Table 4.1: Independent components in  $\eta_{ijkl}$ .

	General		Isotropic	
	Even	Odd	Even	Odd
2D	6	3	2	1
3D	21	15	2	0

Here  $\sigma^A$  are Pauli matrices. Since  $i \leftrightarrow j, k \leftrightarrow l$  symmetric, only 0, 1, 3 are adopted. Thus, the independent elements  $\eta_{AB}$  span a 9 dimensional space, with 6 even ones and 3 odd ones.

Next we investigate the independent isotropic elements. Note that

$$\begin{aligned}
 e^{i\sigma^2\theta} &= \sum_{n=0}^{\infty} \frac{(i\theta)^{2n}}{(2n)!} + \sum_{n=0}^{\infty} \frac{(i\theta)^{2n+1}}{(2n+1)!} \sigma^2 \\
 &= \cos \theta I + i\sigma^2 \sin \theta \\
 &= \begin{pmatrix} \cos \theta & \sin \theta \\ -\sin \theta & \cos \theta \end{pmatrix} \equiv U
 \end{aligned} \tag{4.18}$$

So  $U$  is the SO(2) rotation operator. It is real so  $U^T = U^\dagger = U^{-1}$ . That means that under rotation,

$$\begin{aligned}
 \eta_{ijkl} &\rightarrow U_{ii'} U_{jj'} U_{kk'} U_{ll'} \eta_{i'j'k'l'} \\
 &= \eta_{AB} (U_{ii'} \sigma_{i'j'}^A U_{j'j}^\dagger) \otimes (U_{kk'} \sigma_{k'l'}^B U_{l'l}^\dagger) \\
 &= \eta_{AB} (U \sigma^A U^\dagger)_{ij} (U \sigma^B U^\dagger)_{kl}.
 \end{aligned} \tag{4.19}$$

Using  $e^A B e^{-A} = \sum_n [A^{(n)}, B]/n!$ ,

$$U \sigma^1 U^\dagger = \cos 2\theta \sigma^1 + \sin 2\theta \sigma^3 \tag{4.20}$$

$$U \sigma^3 U^\dagger = -\sin 2\theta \sigma^1 + \cos 2\theta \sigma^3. \tag{4.21}$$

So

$$\eta_{ijkl} \rightarrow \sigma^3 \otimes \sigma^3 [\eta_{11}s^2 + \eta_{33}c^2 + sc(\eta_{13} + \eta_{31})] \quad (4.22)$$

$$+ \sigma^1 \otimes \sigma^1 [\eta_{11}c^2 + \eta_{33}s^2 - sc(\eta_{13} + \eta_{31})] \quad (4.23)$$

$$+ (\sigma^1 \otimes \sigma^3 + \sigma^3 \otimes \sigma^1) [\eta_{11} - \eta_{33}] sc \quad (4.24)$$

$$+ \sigma^1 \otimes \sigma^3 [\eta_{13}c^2 - \eta_{31}s^2] \quad (4.25)$$

$$+ \sigma^3 \otimes \sigma^1 [-\eta_{13}s^2 + \eta_{31}c^2] \quad (4.26)$$

$$+ (I \otimes \sigma^1 + \sigma^1 \otimes I) [\eta_{01}c - \eta_{03}s] \quad (4.27)$$

$$+ (I \otimes \sigma^3 + \sigma^3 \otimes I) [\eta_{01}s + \eta_{03}c] \quad (4.28)$$

$$+ \eta_{00} I \otimes I. \quad (4.29)$$

Here  $s = \sin 2\theta, c = \cos 2\theta$ . From these we see there are three independent components that are invariant under rotation:  $\zeta = \eta_{00}, \eta^S = \eta_{11} = \eta_{33}$ , and  $\eta_H = \eta_{13} = -\eta_{31}$ . Explicitly, the isotropic components are

$$\text{Even: } \quad \zeta I \otimes I, \quad \eta^S (\sigma^1 \otimes \sigma^1 + \sigma^3 \otimes \sigma^3), \quad (4.30)$$

$$\text{Odd: } \quad \eta_H (\sigma^1 \otimes \sigma^3 - \sigma^3 \otimes \sigma^1). \quad (4.31)$$

Written explicitly,

$$\text{Even: } \quad \zeta \delta_{ij} \delta_{kl}, \quad \eta^S (\delta_{ik} \delta_{jl} + \delta_{il} \delta_{jk} - \delta_{ij} \delta_{kl}), \quad (4.32)$$

$$\text{Odd: } \quad -\frac{\eta_H}{2} (\epsilon_{ik} \delta_{jl} + \epsilon_{jk} \delta_{il} + \epsilon_{il} \delta_{jk} + \epsilon_{jl} \delta_{ik}). \quad (4.33)$$

The corresponding stress tensor is

$$\text{Even: } \sigma_{ij}^S = \zeta \delta_{ij} \partial_k v_k + \eta^S (\partial_i v_j + \partial_j v_i - \delta_{ij} \partial_k v_k) \quad (4.34)$$

$$\text{Odd: } \sigma_{xx}^A = -\eta_H (\partial_x v_y + \partial_y v_x) \quad (4.35)$$

$$\sigma_{yy}^A = \eta_H (\partial_x v_y + \partial_y v_x) \quad (4.36)$$

$$\sigma_{xy}^A = \sigma_{yx}^A = \eta_H (\partial_x v_x - \partial_y v_y) \quad (4.37)$$

### 3D

Use the representation

$$\eta_{ijkl} S_i S_j S_k S_l \quad (4.38)$$

to map the SO(3) rotation property into SU(2) rotation as follows. Here  $S_i$  are spin operators. A SU(2) rotation corresponds to  $U = e^{-i\mathbf{S} \cdot \hat{\theta}}$  acting on  $S_i$ :

$$\begin{aligned} \eta &= \eta_{ijkl} S_i \otimes S_j \otimes S_k \otimes S_l \\ &\rightarrow \eta_{ijkl} (US_i U^\dagger) \otimes \cdots \otimes (US_l U^\dagger) \cdots \\ &= \eta_{ijkl} (\alpha_{i\bar{i}'} S_{\bar{i}'}) \otimes \cdots \otimes (\alpha_{l\bar{l}'} S_{\bar{l}'}) \cdots \\ &= \left[ \alpha_{i\bar{i}'} \alpha_{j\bar{j}'} \alpha_{k\bar{k}'} \alpha_{l\bar{l}'} \eta_{ijkl} \right] S_{\bar{i}'} \otimes \cdots \otimes S_{\bar{l}'} \end{aligned} \quad (4.39)$$

where  $\alpha_{i\bar{i}'}$  is the matrix element of SO(3) transform in Cartesian coordinates. Then the term in the square bracket is the viscosity tensor after rotation.

We can then analyze the rotation property by first adding  $S_i \otimes S_j$  into total spin representation. Each spin operator can be regarded as  $\hat{Y}_{L=1,M}(\hat{\mathbf{S}})$ , so it is an  $L = 1$  representation of su(2), and their tensor product can be decomposed as

$$1 \otimes 1 = 2 \oplus 1 \oplus 0 \quad (4.40)$$

Technically, this is writing  $S_i S_j$  in terms of  $Y_{L=2,M}(\mathbf{S})$ ,  $Y_{L=1,M}(\mathbf{S})$  and  $Y_{L=0,M}(\mathbf{S})$ . The 2, 0 representations are even under exchanging  $i \leftrightarrow j$ , while 1 is odd. Regarding the symmetry

property of  $\eta_{ijkl}$  we only take  $2 \oplus 0$  representation. The  $S_k \otimes S_l$  can be added in the same way. Then  $S_i S_j S_k S_l$  is added into the total spin representation

$$\begin{aligned}
(2 \oplus 0)^2 &= 4_{22} \oplus 3_{22} \oplus 2_{22} \oplus 1_{11} \oplus 0_{22} \\
&\oplus 2_{20} \oplus 2_{02} \\
&\oplus 0_{00}.
\end{aligned} \tag{4.41}$$

Each representation contributes independent components as summarized in Table 4.2. Even and odd are referring to exchange of index pairs  $(ij) \leftrightarrow (kl)$ . So in total there are 21 even

Table 4.2: Independent elements contributed by each representation

	4 <sub>22</sub>	3 <sub>22</sub>	2 <sub>22</sub>	1 <sub>22</sub>	0 <sub>22</sub>	2 <sub>20</sub> &2 <sub>02</sub>	0 <sub>00</sub>
Even	9		5		1	5	1
Odd		7		3		5	

components and 15 odd components. The only 2 isotropic ones  $0_{22}, 0_{00}$  are all even ones. Thus, there is no Hall viscosity in *isotropic* 3D fluid. The stress tensor is expressed in the usual way

$$\sigma_{ij} = \zeta \delta_{ij} \partial_k v_k + \eta^S (\partial_i v_j + \partial_j v_i - \frac{2}{3} \delta_{ij} \partial_k v_k). \tag{4.42}$$

## 4.2 Adiabatic Approach

The previous section gives macroscopic formulation of viscosity in terms of hydrodynamics. This section shows microscopically that the Hall viscosity can be regarded as Berry curvature in the distortion parameter space, and can be calculated using the distorted wave function.

### 4.2.1 Berry Curvature for Distortion

We start from the microscopic many-body Hamiltonian, with the distortion  $u_{ij}$  as parameter:  $\hat{H}[u_{ij}]$ . ( $u_{ij}$  functions just like  $\mathbf{k}$  for Bloch Hamiltonians). The stress tensor operator can be defined using (4.11). Note  $\hat{H}$  is the many-body Hamiltonian representing the whole system, while  $\delta\epsilon$  in (4.11) is energy density. For *homogeneous* systems the volume integration simply gives  $V$ . So

$$V\hat{\sigma}_{ij} = -\frac{\partial\hat{H}[u_{ij}]}{\partial u_{ij}} \quad (4.43)$$

Then

$$\begin{aligned} V\langle\hat{\sigma}_{ij}\rangle &= -\left\langle\psi[u_{ij}]\left|\frac{\partial\hat{H}[u_{ij}]}{\partial u_{ij}}\right|\psi[u_{ij}]\right\rangle \\ &= -\frac{\partial\langle\hat{H}\rangle}{\partial u_{ij}} + \left\langle\frac{\partial\psi}{\partial u_{ij}}|\hat{H}|\psi\right\rangle + \left\langle\psi|\hat{H}|\frac{\partial\psi}{\partial u_{ij}}\right\rangle \\ &= -\frac{\partial E}{\partial u_{ij}} + \left\langle\frac{\partial\psi}{\partial u_{ij}}|i\hbar\partial_t|\psi\right\rangle + (-i\hbar\partial_t\langle\psi|)\left|\frac{\partial\psi}{\partial u_{ij}}\right\rangle \\ &= -\frac{\partial E}{\partial u_{ij}} + i\hbar\left\langle\frac{\partial\psi}{\partial u_{ij}}\left|\frac{\partial\psi}{\partial u_{kl}}\right\rangle\dot{u}_{kl} - i\hbar\left\langle\frac{\partial\psi}{\partial u_{kl}}\left|\frac{\partial\psi}{\partial u_{ij}}\right\rangle\dot{u}_{kl}\right\rangle \\ &= -\frac{\partial E}{\partial u_{ij}} + \Omega_{ijkl}v_{kl} \end{aligned} \quad (4.44)$$

where the Berry curvature is

$$\Omega_{ijkl} = i\hbar\left[\left\langle\frac{\partial\psi}{\partial u_{ij}}\left|\frac{\partial\psi}{\partial u_{kl}}\right\rangle - \left\langle\frac{\partial\psi}{\partial u_{kl}}\left|\frac{\partial\psi}{\partial u_{ij}}\right\rangle\right] = -2\hbar\text{Im}\left\langle\frac{\partial\psi}{\partial u_{ij}}\left|\frac{\partial\psi}{\partial u_{kl}}\right\rangle\right. \quad (4.45)$$

Compared with the hydrodynamic result (4.8),  $\langle\hat{T}_{ij}\rangle = \eta_{ijkl}v_{kl}$ , we see the Berry curvature in response to distortion in a *homogeneous* system is the viscosity <sup>5</sup>

$$\eta_{ijkl} = \frac{\Omega_{ijkl}}{V} \quad (4.46)$$

(The first term represents elasticity, which we will not discuss here.)

<sup>5</sup>From the derivation we see that for non-homogeneous system,  $\Omega_{ijkl} = \int \eta_{ijkl}(\mathbf{x}) d\mathbf{x}$ . Then we cannot extract viscosity from the Berry curvature calculation in general. Thus, the adiabatic method is effective only in homogeneous systems.

## 4.2.2 Distortion and Metric

The distortion of the system can be described as a change of metric. Specifically, originally we have the line element

$$ds^2 = \delta_{ij} dx^i dx^j \quad (4.47)$$

After distortion,  $dx^i \rightarrow dx^i + du^i(\mathbf{x})$ . Then the line element becomes

$$\begin{aligned} ds'^2 &= \delta_{ij} (dx^i + du^i)(dx^j + du^j) \\ &= \delta_{ij} dx^i dx^j + \delta_{ij} dx^i \frac{\partial u^j}{\partial x^k} dx^k + \delta_{ij} \frac{\partial u^i}{\partial x^k} dx^k dx^j + O((du)^2) \\ &= \left( \delta_{ij} + (\partial_i u_j + \partial_j u_i) \right) dx^i dx^j \end{aligned} \quad (4.48)$$

So we can regard the metric being changed to (see Eq. (4.12) for definition of  $u_{ij}$ )

$$\delta_{ij} \rightarrow g_{ij} = \delta_{ij} + 2u_{ij} \quad (4.49)$$

The inverse of the metric,  $g^{ij} g_{jk} = \delta_k^i$ , is

$$g^{ij} = \delta_{ij} - 2u_{ij}, \quad (4.50)$$

also correct up to linear order in  $u_{ij}$ . Then (4.45), (4.46) can be re-written as

$$\eta_{ijkl} = -\frac{8\hbar}{V} \text{Im} \left\langle \frac{\partial \psi}{\partial g_{ij}} \left| \frac{\partial \psi}{\partial g_{kl}} \right. \right\rangle = -\frac{8\hbar}{V} \text{Im} \left\langle \frac{\partial \psi}{\partial g^{ij}} \left| \frac{\partial \psi}{\partial g^{kl}} \right. \right\rangle \quad (4.51)$$

Due to the simple relation between metric and strain, from now on we would focus on the metric only because it is easier to manipulate.

## 4.2.3 Distortion of Unit Parallelogram

A simplest homogeneous distortion is the distortion of unit parallelogram, as illustrated in Fig. 4.1. Originally, the two edges have ratio 1 : 1. After distortion, as illustrated by red

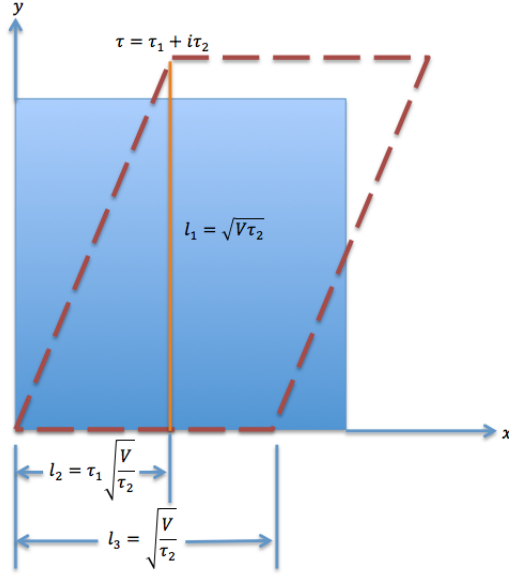


Figure 4.1: Distortion of unit parallelogram. The volume is held fixed.

dashed parallelogram, the two edges have ratio  $1 : \tau$  parametrized by  $\tau = \tau_1 + i\tau_2$ , and are no longer perpendicular to each other. The constraint is that volume is kept the same. So  $l_1 = \alpha\tau_2, l_3 = \alpha \cdot 1 \Rightarrow V = \alpha\tau_2 \cdot \alpha \Rightarrow \alpha = \sqrt{V/\tau_2}$ . Then we have  $l_1, l_2, l_3$  as illustrated in the figure, and further

$$\begin{cases} x' = \sqrt{\frac{V}{\tau_2}}x + y \sqrt{V\tau_2} \cdot \frac{\tau_1 \sqrt{V/\tau_2}}{\sqrt{V\tau_2}} = \sqrt{\frac{V}{\tau_2}}x + y \sqrt{\frac{V}{\tau_2}}\tau_1 \\ y' = \sqrt{V\tau_2}y \end{cases} \quad (4.52)$$

Then

$$ds'^2 = dx'^2 + dy'^2 = \frac{V}{\tau_2}(dx + \tau_1 dy)^2 + V\tau_2 dy^2 \quad (4.53)$$

$$= \frac{V}{\tau_2}[dx^2 + 2\tau_1 dx dy + |\tau|^2 dy^2]. \quad (4.54)$$

That means the metric is

$$g_{ij} = \frac{V}{\tau_2} \begin{pmatrix} 1 & \tau_1 \\ \tau_1 & |\tau|^2 \end{pmatrix}, \quad \Rightarrow g^{ij} = (g_{ij})^{-1} = \frac{1}{V\tau_2} \begin{pmatrix} |\tau|^2 & -\tau_1 \\ -\tau_1 & 1 \end{pmatrix} \quad (4.55)$$



With such parametrization, we can rewrite (4.51).

$$\tau_1 = -\frac{g^{xy} + g^{yx}}{2g^{yy}}, \tau_2 = \frac{\sqrt{g^{xx}g^{yy} - (g^{xy})^2}}{g^{yy}}, V = \frac{1}{\sqrt{g^{xx}g^{yy} - (g^{xy})^2}} \quad (4.56)$$

Thus,

$$\frac{\partial}{\partial g^{xx}} = \frac{1}{2}(\partial_{\tau_2} - \partial_V), \quad (4.57)$$

$$\frac{\partial}{\partial g^{yy}} = -\frac{1}{2}(\partial_{\tau_2} + \partial_V), \quad (4.58)$$

$$\frac{\partial}{\partial g^{xy}} = \frac{\partial}{\partial g^{yx}} = -\frac{1}{2}\partial_{\tau_1}. \quad (4.59)$$

The differentiations are evaluated in Euclidean metric  $g_{ij} = \delta_{ij}$ . Plug these into (4.51), and note the wave function generally does not depend on  $V$  (because  $V$  appears only as a global factor in Hamiltonian for a homogeneous system), there is only one component for Hall viscosity as expected:

$$\eta_H = \eta_{yxxx} = -\eta_{xxxy} = \frac{2\hbar}{V} \text{Im} \left\langle \frac{\partial\psi}{\partial\tau_1} \left| \frac{\partial\psi}{\partial\tau_2} \right. \right\rangle. \quad (4.60)$$

Thus, once we know the distorted wave function parametrized by  $\tau_1, \tau_2$ , we can readily calculate Hall viscosity using this formula.

A special case is that if the coordinate part of the wave function is analytic,

$$\psi(\tau_1, \tau_2, \mathbf{x}) = A(\tau_1, \tau_2)\Phi(\tau, \mathbf{x}) \quad (4.61)$$

where  $\Phi(\tau)$  only depend on  $\tau = \tau_1 + \tau_2$  and  $A$  is real, then

$$\begin{aligned}
& \left\langle \frac{\partial A \Phi}{\partial \tau_1} \middle| \frac{\partial A \Phi}{\partial \tau_2} \right\rangle - \left\langle \frac{\partial A \Phi}{\partial \tau_2} \middle| \frac{\partial A \Phi}{\partial \tau_1} \right\rangle \\
&= \langle (\partial_1 A) \Phi + A \partial_1 \Phi | (\partial_2 A) \Phi + A \partial_2 \Phi \rangle \\
&\quad - \langle (\partial_2 A) \Phi + A \partial_2 \Phi | (\partial_1 A) \Phi + A \partial_1 \Phi \rangle \\
&= [(\partial_1 A) \partial_2 A - (\partial_2 A) \partial_1 A] \langle \Phi | \Phi \rangle
\end{aligned} \tag{4.62}$$

$$+ (\partial_1 A) A \langle \Phi | \partial_2 \Phi \rangle + A (\partial_2 A) \langle \partial_1 \Phi | \Phi \rangle - c.c. \tag{4.63}$$

$$+ A^2 \langle \partial_1 \Phi | \partial_2 \Phi \rangle - c.c. \tag{4.64}$$

Since  $\partial_{\tau_1} = \partial_\tau + \partial_{\bar{\tau}}$ ,  $\partial_{\tau_2} = i(\partial_\tau - \partial_{\bar{\tau}})$ , and  $\partial = (\partial_1 - i\partial_2)/2$ ,  $\bar{\partial} = (\partial_1 + i\partial_2)/2$ ,

$$(4.62) = [(\partial_1 A) \partial_2 A - (\partial_2 A) \partial_1 A] \frac{1}{A^2} = 0$$

$$(4.63) = (A \partial_1 A) i \partial \frac{1}{A^2} + (A \partial_2 A) \bar{\partial} \frac{1}{A^2} - c.c.$$

$$= i(A \partial_1 A) \left(-\frac{2}{A^3}\right) \partial A + (A \partial_2 A) \left(-\frac{2}{A^3}\right) \bar{\partial} A - c.c.$$

$$= -i \frac{\partial_1 A}{A^2} (\partial_1 - i\partial_2) A - \frac{\partial_2 A}{A^2} (\partial_1 + i\partial_2) A - c.c.$$

$$= -i \frac{(\partial_1 A)^2}{A^2} - i \frac{(\partial_2 A)^2}{A^2} - \frac{\partial_1 A}{A^2} - \frac{\partial_2 A \partial_1 A}{A^2} - c.c.$$

$$= -2i \frac{(\partial_1 A)^2 + (\partial_2 A)^2}{A^2}$$

$$(4.64) = A^2 (\bar{\partial} i \partial) \frac{1}{A^2} - c.c.$$

$$= 2i A^2 \left(\frac{\partial_1 + i\partial_2}{2}\right) \left(\frac{\partial_1 - i\partial_2}{2}\right) \frac{1}{A^2}$$

$$= \frac{i A^2}{2} (\partial_1^2 + \partial_2^2) \frac{1}{A^2}$$

$$= -i \left[ \frac{(\partial_1^2 + \partial_2^2) A}{A} - 3 \frac{(\partial_1 A)^2 + (\partial_2 A)^2}{A^2} \right].$$

Together, we have

$$-i \left[ \frac{(\partial_1^2 + \partial_2^2) A}{A} - \frac{(\partial_1 A)^2 + (\partial_2 A)^2}{A^2} \right] = -i(\partial_1^2 + \partial_2^2) \ln A. \tag{4.65}$$

Then

$$\eta_H = -\frac{\hbar}{V}(\partial_1^2 + \partial_2^2) \ln A(\tau_1, \tau_2). \quad (4.66)$$

The calculation is greatly simplified as we only need to look at the normalization factor.

#### 4.2.4 Example: Quantum Hall Systems

First we write down the Hamiltonian in an arbitrary metric. The magnetic field is along  $\hat{z}$  direction and is homogeneous. The system is in x-y plane. The Hamiltonian with flat metric is

$$H = \frac{(\mathbf{p} - e\mathbf{A})^2}{2M} \quad (4.67)$$

$$= \frac{1}{2M}[-\hbar^2\nabla^2 + 2i\hbar e\mathbf{A} \cdot \nabla + i\hbar e(\nabla \cdot \mathbf{A}) + e^2\mathbf{A}^2] \quad (4.68)$$

In a general metric, each term becomes

$$\nabla^2 = \frac{1}{\sqrt{g}}\partial_i \sqrt{g}g^{ij}\partial_j \quad (4.69)$$

$$\mathbf{A} \cdot \nabla = A^i\partial_i \quad (4.70)$$

$$\nabla \cdot \mathbf{A} = \frac{1}{\sqrt{g}}\partial_i \sqrt{g}A^i \quad (4.71)$$

$$\mathbf{A}^2 = g_{ij}A^iA^j \quad (4.72)$$

Using this, and apply the notation  $A_i = g_{ij}A^j$ , we can write the Hamiltonian as

$$H = \frac{1}{2M} \frac{1}{\sqrt{g}}\pi_i \sqrt{g}g^{ij}\pi_j, \quad (4.73)$$

where

$$\pi_i = -i\hbar\partial_i - eA_i. \quad (4.74)$$

In the rest of this section, the metric is taken to be homogeneous (it only has time dependence). Then

$$H = \frac{g^{ij}\pi_i\pi_j}{2M}. \quad (4.75)$$

Adopt the metric (4.55),

$$\begin{aligned}
H &= \frac{1}{2MV\tau_2} [|\tau|^2\pi_x^2 + \pi_y^2 - \tau_1(\pi_x\pi_y + \pi_y\pi_x)] \\
&= \frac{1}{2MV\tau_2} [|\tau|^2\pi_x^2 + \pi_y^2 - 2\tau_1\pi_y\pi_x - i\hbar eB\tau_1] \\
&= \frac{1}{2MV\tau_2} (\tau^*\pi_x - \pi_y)(\tau\pi_x - \pi_y) + \frac{\hbar eB}{2MV},
\end{aligned} \tag{4.76}$$

where we have repeatedly used the commutation relation  $[\pi_i, \pi_j] = i\hbar eB$ . Recall that for Euclidean metric,  $\tau = i$ , and we readily recognize that the corresponding Landau level operators in distorted geometry are

$$a = \frac{1}{\sqrt{2\hbar eB\tau_2}}(\tau\pi_x - \pi_y), \quad a^\dagger = \frac{1}{\sqrt{2\hbar eB\tau_2}}(\tau^*\pi_x - \pi_y), \tag{4.77}$$

and

$$[a, a^\dagger] = 1. \tag{4.78}$$

The Hamiltonian then becomes

$$H = \frac{\hbar\omega}{V} \left( a^\dagger a + \frac{1}{2} \right), \tag{4.79}$$

where  $\omega = eB/M$ . As expected, for a fluid, only changing the volume affects the energy, while shear deformation  $\tau$  does not. But the shear will distort the wave function.

To be specific, we work out lowest Landau level (LLL) wavefunctions in Landau gauge. The discussion in spherical gauge is left to the appendix.

In Landau gauge,  $\mathbf{A} = B(-y, 0, 0)$ , and the wavefunction is an eigenstate of  $p_x$ .  $\pi_x = p_x + eBy$ ,  $\pi_y = -i\hbar\partial_y$ . Then

$$a = \frac{1}{\sqrt{2\tau_2\hbar eB}} [\tau(p_x + eBy) + i\hbar\partial_y], \tag{4.80}$$

$$a^\dagger = \frac{1}{\sqrt{2\tau_2\hbar eB}} [\tau^*(p_x + eBy) + i\hbar\partial_y]. \tag{4.81}$$

The ground state wavefunction is given by the condition  $a\phi_0 = 0$ , which gives

$$\phi_{0,p_x} = \left( \frac{e^{ip_x x}}{\sqrt{L_x}} \right) \left( \frac{eB\tau_2}{\pi\hbar} \right)^{\frac{1}{4}} e^{i\tau \frac{(p_x + eBy)^2}{2\hbar eB}} \quad (4.82)$$

Denote  $l_B = \frac{\hbar}{eB}$ ,  $y_0 = -p_x/eB$ ,

$$\phi_{0,p_x} = \left( \frac{e^{ip_x x}}{\sqrt{L_x}} \right) \left[ \left( \frac{\tau_2}{\pi l_B^2} \right)^{\frac{1}{4}} e^{i\tau \frac{(y-y_0)^2}{2l_B^2}} \right] \quad (4.83)$$

Thus, a general many-body wave function is of the form

$$\Psi = A(\tau_1, \tau_2) f(\mathbf{x}_1 \dots \mathbf{x}_N, \tau) \prod_{i=1}^N e^{i\tau \frac{(y^{(i)} - y_0^{(i)})^2}{2l_B^2}} \quad (4.84)$$

Now we can use (4.66) to evaluate the Hall viscosity. A further simplification occurs in the thermodynamic limit where the filling factor is kept constant, but the degeneracy and the particle number go to infinity. That means  $l_B \rightarrow 0$ , and the normalization is effectively independent of  $f$ . Then in  $A(\tau_1, \tau_2)$ , the relevant part is the factor  $(\tau_2^{1/4})^N$  coming from the normalization of  $e^{-\tau_2(y-y_0)^2/2l_B^2}$  for the  $N$  particles. Therefore,

$$\eta_H = -\frac{\hbar}{V} \partial_2^2 \left[ \frac{N}{4} \ln \tau_2 \right] \Big|_{\tau_2=1} = \frac{\hbar n}{4}, \quad n = \frac{N}{V} \quad (4.85)$$

### 4.3 Wen-Zee Effective Theory

Haldane shows that for a QH on a spherical surface,

$$H = \frac{\mathbf{L}^2 - (\hbar q)^2}{2M}, \quad q = \frac{1}{2}, 1, \frac{3}{2}, 2, \dots \quad (4.86)$$

where  $q$  is the monopole quantization number:

$$\nabla \cdot \mathbf{B} = \Phi \delta(\mathbf{x}), \quad \Phi = \frac{h}{e}(2q) \quad (4.87)$$

$\Phi = B \cdot 4\pi R^2$  is the flux through the spherical surface. And

$$H|lm\rangle = \frac{\hbar^2}{2MR^2} [l(l+1) - q^2] \quad (4.88)$$

Or we can write  $\frac{\hbar^2}{2MR^2} = \frac{\hbar\omega}{2q}$  with  $\omega = eB/M$ . Here

$$\mathbf{L} = \mathbf{\Lambda} + \hbar q \hat{n} \quad (4.89)$$

where  $\vec{\Lambda} = \vec{r} \times \vec{\pi}$ ,  $\vec{\pi} = \vec{p} + e\vec{A}$ , and  $\hat{n} = \mathbf{e}_r$ . But note

$$\vec{L} \cdot \hat{n} = \hbar q, \quad (4.90)$$

$l$  has minimal number  $q$ . So denote

$$l = q + n, \quad n = 0, 1, 2, \dots \quad (4.91)$$

we have

$$H|lm\rangle = \frac{\hbar\omega}{2q} [q(2n+1) + n(n+1)], \quad n = 0, 1, \dots \quad (4.92)$$

The degeneracy of  $n$ -th level is

$$2l + 1 = 2(q + n) + 1 = 2q + (2n + 1) \quad (4.93)$$

Then we see that different from planar QH, the degeneracy differs from the flux quanta by  $(2n + 1)$ .

The Wen & Zee effective theory is that

$$\mathcal{L} = \frac{1}{4\pi} \left( a_\mu^I \epsilon^{\mu\nu\lambda} K_{IJ} \partial_\nu a_\lambda^J + 2A_\mu t_I \epsilon^{\mu\nu\lambda} \partial_\nu a_\lambda^I + 2\omega_\mu s_I \epsilon^{\mu\nu\lambda} \partial_\nu a_\lambda^I \right) \quad (4.94)$$

The first term is the effective Ginzburg-Landau term producing the QHE. It is generalized to multiple components denoted by  $I, J$  with the coupling specified by the  $K$ -matrix. The second term is the coupling of external vector potential  $A_\mu$  to the system. The third term is the key. It describes the coupling of external geometry to the system.

Before proceeding, we do some geometry. Denote the set of basis field as  $\{(e_\mu)^a\}$ . Then

$$(e_\tau)^b \nabla_b (e_\mu)^a = \Gamma_{\mu\tau}^\sigma (e_\sigma)^a. \quad (4.95)$$

Define connection 1-form

$$(\omega_\mu^\nu)_a = -\Gamma_{\mu\tau}^\nu (e^\tau)_a = (e_\mu)^\epsilon \nabla_a (e^\nu)_\epsilon \quad (4.96)$$

It is related to the basis field via the *First Cartan Equation*

$$(de^\nu)_{ab} = -(e^\mu)_a \wedge (\omega_\mu^\nu)_b. \quad (4.97)$$

The curvature two form defined by

$$(R_\mu^\nu)_{ab} = R_{abc}{}^d (e_\mu)^a (e^\nu)_b \quad (4.98)$$

is related to the connection through the *Second Cartan Equation*

$$(R_\mu^\nu)_{ab} = (d\omega_\mu^\nu)_{ab} + (\omega_\mu^\lambda)_a \wedge (\omega_\lambda^\nu)_b \quad (4.99)$$

On a spherical surface,

$$(e^1)_a = R(d\theta)_a, \quad (e^2)_a = R \sin \theta (d\phi)_a. \quad (4.100)$$

Then taking the exterior derivative, we have

$$(de^1)_{ab} = 0, \quad (de^2)_{ab} = R \cos \theta (d\theta)_b \wedge (d\phi)_a. \quad (4.101)$$

Thus, the first Cartan equation (for components  $\nu = 1, 2$ ) is written explicitly as

$$0 = -R(d\theta)_a \wedge (\omega_1^1)_b - R \sin \theta (d\phi)_a \wedge (\omega_2^1)_b, \quad (4.102)$$

$$R \cos \theta (d\theta)_b \wedge (d\phi)_a = -R(d\theta)_a \wedge (\omega_1^2)_b - R \sin \theta (d\phi)_a \wedge (\omega_2^2)_b. \quad (4.103)$$

The Cartan equations do not uniquely fix the connection — just like the connection  $\mathbf{A}$  in gauge theories, they are only fixed up to a gauge transform. From these equations we can choose the simplest connection

$$\omega_1^1 = \omega_2^2 = \omega_2^1 = 0; \quad \omega_1^2 = -\cos \theta d\phi \quad (4.104)$$

Since there is only one component, we will later on denote it simply as

$$\omega = -\cos\theta d\phi. \quad (4.105)$$

Further, the curvature

$$(R_2^1)_{ab} = (d\omega_2^1)_{ab} = \sin\theta(d\theta)_a \wedge (d\phi)_b, \quad (4.106)$$

or simply

$$R = d\omega = \sin\theta d\theta \wedge d\phi \quad (4.107)$$

To extract physics from (4.94), we integrate out gauge fields  $a_\mu^I$  in  $\int \mathcal{D}a e^{i\int \mathcal{L}}$ . Denote (4.94) as

$$\mathcal{L} = \frac{1}{4\pi} [a(K\epsilon\partial)a + (2At\epsilon\partial)a + (2\omega s\epsilon\partial)a] \quad (4.108)$$

and treat the terms in (...) as matrix. From the Gaussian integral formula

$$\int \mathcal{D}v e^{-v^T A v + \rho^T v} = \sqrt{\frac{\pi^D}{\det A}} e^{\frac{1}{2}\rho^T A^{-1}\rho}, \quad (4.109)$$

we get

$$\mathcal{L}_{\text{eff}} = -\frac{1}{4\pi} (At\epsilon\partial + \omega s\epsilon\partial)(K\epsilon\partial)^{-1}(At\epsilon\partial + \omega s\epsilon\partial) \quad (4.110)$$

$$= \frac{1}{4\pi} (At + \omega s)K^{-1}\epsilon\partial(At + \omega s). \quad (4.111)$$

Then, the electric current is

$$J_e = \frac{\delta\mathcal{L}}{\delta A} = \frac{1}{2\pi} tK^{-1}\epsilon\partial(At + \omega s), \quad (4.112)$$

and the ‘‘geometry current’’ is

$$J_s = \frac{\delta\mathcal{L}}{\delta\omega} = \frac{1}{2\pi} sK^{-1}\epsilon\partial(At + \omega s). \quad (4.113)$$



The zero-th component means density. So

$$\begin{pmatrix} \rho_e \\ \rho_s \end{pmatrix} = \begin{pmatrix} tK^{-1}t & tK^{-1}s \\ sK^{-1}t & sK^{-1}s \end{pmatrix} \begin{pmatrix} dA \\ d\omega \end{pmatrix} \quad (4.114)$$

Note  $dA = B, d\omega = R$ . Integrate over space we have

$$\begin{pmatrix} N_e \\ N_s \end{pmatrix} = \begin{pmatrix} tK^{-1}t & tK^{-1}s \\ sK^{-1}t & sK^{-1}s \end{pmatrix} \begin{pmatrix} N_\phi \\ N_R \end{pmatrix} \quad (4.115)$$

where  $\Phi$  is the magnetic flux, and  $N_R = 2(1 - g)$  with  $g$  the genus of the system's topology, i.e. 0 for spherical surface, 1 for plane. That means

$$N_e = (tK^{-1}t)N_\phi + (tK^{-1}s)N_R \equiv \nu(N_\phi + \mathcal{S}). \quad (4.116)$$

Regard

$$\nu = tK^{-1}t \quad (4.117)$$

as filling factor, we see that the shift is

$$\mathcal{S} = \frac{tK^{-1}s}{tK^{-1}t} N_R. \quad (4.118)$$

Now we revisit Haldane's model. The flux through the spherical surface is  $N_\phi = 2q$ . Consider  $\nu = N$  Landau levels being filled, each with degeneracy  $2(q + n) + 1$ . So in total

$$N_e = \sum_{n=0}^{N-1} [2(q + n) + 1] = NN_\phi + N^2 = \nu(N_\phi + N). \quad (4.119)$$

Thus, the shift  $\mathcal{S} = N$ . The non-interacting N-level model corresponds to rank-N  $K_{IJ} = \delta_{IJ}$ , and  $t_I = (1, \dots, 1)$ . Then  $tK^{-1}t = N$ . The  $I$ -th Landau level contributes to the shift by  $\nu^{-1}(2I - 1) = (2I - 1)/N$ . Thus, from (4.118),

$$\frac{2I - 1}{N} = \frac{s_I}{N} 2 \Rightarrow s_I = I - \frac{1}{2}. \quad (4.120)$$

Later on in other literatures,  $\mathcal{S}$  is referred to as “shift”, and  $s_I$ , the curvature charge, is referred to as “orbital spin”. For lowest Landau level being filled,  $s_1 = \frac{1}{2}$ . Compared with (4.85), we can write

$$\eta_H = \frac{sn\hbar}{2}. \quad (4.121)$$

Also, for the ground state,  $\mathcal{S} = 1$ , which mean  $\mathcal{S} = 2s_1$ .

## 4.4 Density Response

Density response measurement is a powerful and widely applicable tool to probe various systems. In recent works, many authors have related Hall viscosity to density response functions, i.e. the static structure factor [115, 121], using certain trial wave functions. It is intriguing to see whether there are *universal* relations between density response functions and Hall viscosity. In the following, we will relate the Hall viscosity  $\eta_H$  to the  $q^4$  term in the density-susceptibility  $\chi(\mathbf{q}, \omega)$  for a general Galilean invariant system, thus allowing for measurements of Hall viscosity through density response experiments, or to calculate Hall viscosity through density response functions. We first derive the relation in the microscopic level using Kubo formulae, and verify the results in the integer quantum Hall example. Then we present an independent derivation by applying effective hydrodynamics. The latter method has been adopted [122–124] to analyze collective modes of fractional quantum Hall system at filling  $\nu = 1/3$ , which gives qualitative agreement with experiment. [125] The two derivations give the same result in the long wave-length expansion. Since both of the derivations are independent of specific wave functions, type of interactions, filling factors, and etc., the results (4.135), (4.136) are valid for a general class of Galilean invariant systems.

### 4.4.1 Kubo Formulae Method

We first sketch the idea of relating viscosity and conductivity to susceptibility before the strict derivation. In a viscous fluid, the stress tensor would respond to the velocity gradient  $v_{\alpha\beta} = \frac{1}{2}(\partial_\alpha v_\beta + \partial_\beta v_\alpha)$  through

$$\delta T_{\mu\nu} = \eta_{\mu\nu\alpha\beta} v_{\alpha\beta}, \quad (4.122)$$

where  $\eta_{\mu\nu\rho\sigma}$  are the viscosity coefficients. In three dimensions, rotation symmetry reduces the number of  $\eta_{\mu\nu\rho\sigma}$  to 2, corresponding to the usual shear and bulk viscosity:

$$\eta^S (\delta_{\mu\alpha}\delta_{\nu\beta} + \delta_{\mu\beta}\delta_{\nu\alpha} - \frac{2}{d}\delta_{\mu\nu}\delta_{\alpha\beta}), \quad \zeta\delta_{\mu\nu}\delta_{\alpha\beta}, \quad (4.123)$$

where  $d$  is spatial dimension. But in 2D, the in-plane isotropy allows for an additional one called Hall viscosity

$$\eta_H (\delta_{\nu\alpha}\epsilon_{\mu\beta} - \delta_{\mu\beta}\epsilon_{\alpha\nu}). \quad (4.124)$$

Meanwhile, the density and current of a system would respond to potential and electric field perturbations

$$\delta n(\mathbf{q}, \omega) = \chi(\mathbf{q}, \omega)\varphi(\mathbf{q}, \omega), \quad (4.125)$$

$$\delta j_\alpha(\mathbf{q}, \omega) = \sigma_{\alpha\beta}(\mathbf{q}, \omega)E_\beta(\mathbf{q}, \omega), \quad (4.126)$$

where  $\chi(\mathbf{q}, \omega)$ ,  $\sigma_{\alpha\beta}(\mathbf{q}, \omega)$  are the (charge-)susceptibility and conductivity respectively. The key idea is that since in linear regime, the different transport processes probe the same equilibrium property of the system, the transport coefficients are all related to each other. Technically, the essential ingredients in the Kubo formulae for the transport coefficients are the correlators  $\chi \sim \langle [n, n] \rangle_0$ ,  $\sigma_{\alpha\beta} \sim \langle [j_\alpha, j_\beta] \rangle_0$ , and  $\eta_{\mu\nu\alpha\beta} \sim \langle [T_{\mu\nu}, T_{\alpha\beta}] \rangle_0$ . For Galilean invariant systems, the current is related to momentum by  $\mathbf{j} = \frac{e}{m}\mathbf{p}$ . Thus, the particle and

momentum conservation for the system at equilibrium,

$$\partial_t n(\mathbf{x}, t) + \partial_\alpha p_\alpha(\mathbf{x}, t) = 0, \quad (4.127)$$

$$\partial_t p_\alpha(\mathbf{x}, t) + \partial_\beta T_{\alpha\beta}(\mathbf{x}, t) = f_\alpha(\mathbf{x}, t) \quad (4.128)$$

naturally provides a bridge among the transport coefficients of different types. Roughly speaking, by writing the conservation laws in Fourier space, we see the viscosity is related to the  $q^2$  and  $q^4$  terms in conductivity and susceptibility respectively. Analogous ideas have been adopted recently to discuss the unitary Fermi gases [126] and the conductivity-viscosity relations [119], while in this paper we focus on the density response signatures for 2D systems subject to uniform magnetic field.

The Hamiltonian describing density coupling to external potential is

$$H_1 = \int d^2x \hat{n}(\mathbf{x}) \varphi(\mathbf{x}, t) = \int \frac{d^2q}{(2\pi)^2} \hat{n}(\mathbf{q}) \varphi(-\mathbf{q}, t), \quad (4.129)$$

where  $\hat{n}(\mathbf{x}) = \sum_{j=1}^N \delta(\mathbf{x} - \hat{\mathbf{x}}^j)$  is the density operator, with the Fourier transform  $\hat{n}(\mathbf{q}) = \sum_{j=1}^N e^{-i\mathbf{q} \cdot \hat{\mathbf{x}}^j}$ . For a translational invariant system, the susceptibility [127] is given by

$$\chi(\mathbf{q}, \omega) = -\frac{i}{\hbar} \int_0^\infty dt e^{i\omega^+ t} \int d^2x e^{-i\mathbf{q} \cdot \mathbf{x}} \langle [\hat{n}(\mathbf{x}, t), \hat{n}(\mathbf{0}, 0)] \rangle_0. \quad (4.130)$$

Here  $\langle \dots \rangle_0$  means ensemble average in the fully interacting equilibrium system, and  $\omega^+ = \omega + i\epsilon$  with  $\epsilon \rightarrow 0$  ensuring that the perturbation adiabatically sets in. On the other hand, for current response to electric field, the Kubo formula gives the conductivity [128]

$$\begin{aligned} \sigma_{\alpha\beta}(\mathbf{q}, \omega) &= \frac{ie^2 \bar{n}}{m\omega^+} \delta_{\alpha\beta} + \frac{1}{\hbar\omega^+} \int_0^\infty dt e^{i\omega^+ t} \\ &\quad \times \int d^2x e^{-i\mathbf{q} \cdot \mathbf{x}} \langle [\hat{j}_\alpha(\mathbf{x}, t), \hat{j}_\beta(\mathbf{0}, 0)] \rangle_0, \end{aligned} \quad (4.131)$$

where  $\bar{n} = N/V$  is the average particle number density. Here the current density  $\hat{j}_\alpha(\mathbf{x}) = \frac{e}{2m} \sum_{i=1}^N \{\hat{\pi}_\alpha^i, \delta(\mathbf{x} - \hat{\mathbf{x}}^i)\}$ , where  $\{\dots\}$  is anti-commutator, and  $\hat{\pi}_\alpha^i = \hat{p}_\alpha^i - e\hat{A}_\alpha^i(\hat{\mathbf{x}}^i)$ .

Here we follow the Kubo formulae construction in [119] and obtain the *frequency-dependent* conductivity-viscosity relation in the low-momentum expansion up to the  $q^2$  term, valid for Galilean invariant systems:

$$\begin{aligned}
\sigma_{\mu\nu}^{(2)}(\mathbf{q}, \omega) &= \frac{e^2}{m^2(\omega^2 - \omega_c^2)^2} \\
&\times \left[ \left( \zeta(\omega) - \frac{\kappa_{int}^{-1}}{i\omega} \right) \left( \omega^2 q_\mu q_\nu + i\omega\omega_c q^2 \epsilon_{\mu\nu} + \omega_c^2 \epsilon_{\mu\beta} \epsilon_{\nu\delta} q_\beta q_\delta \right) \right. \\
&\quad + \eta^S(\omega) q^2 \left( (\omega^2 + \omega_c^2) \delta_{\mu\nu} + 2i\omega\omega_c \epsilon_{\mu\nu} \right) \\
&\quad \left. - \eta_H(\omega) \left( i\omega\omega_c (q_\mu q_\nu + q^2 \delta_{\mu\nu}) - (\omega^2 + \omega_c^2) q^2 \epsilon_{\mu\nu} \right) \right], \tag{4.132}
\end{aligned}$$

where  $\omega_c = eB/m$  is the cyclotron frequency, and the ‘‘internal compressibility’’ is

$$\kappa_{int}^{-1} = -V \left( \frac{\partial P_{int}}{\partial V} \right)_{N,\nu} = B^2 \left( \frac{\partial^2 \mathcal{E}}{\partial B^2} \right)_\nu, \tag{4.133}$$

where  $V$  means area. Here the ‘‘internal pressure’’  $P_{int} = P - BM/V$  excludes the pressure contribution from the magnetization  $M$  due to edge current [119, 129]. Note that the derivative is taken at fixed  $\nu$  instead of fixed  $B$ . Thus, the internal compressibility has a finite value.

In previous literatures [118, 119], the explicit frequency dependence in (4.132) was not given, as for the discussion there it was not important. But from the relation between susceptibility and conductivity [130], obtained from Kubo formulae (4.130) (4.131) and particle conservation (4.127),

$$\chi(\mathbf{q}, \omega) = \frac{q_\alpha q_\beta}{ie^2 \omega^+} \sigma_{\alpha\beta}(\mathbf{q}, \omega), \tag{4.134}$$

we see that even if one only considers the susceptibility at zero-frequency, it reflects the linear-in-frequency part of the conductivity. As we shall see later, it is essential to incorporate the  $\omega$ -dependence in (4.132) before taking the limit. Explicitly, (4.132) and (4.134)

shows the susceptibility-viscosity relation

$$\chi^{(4)}(\mathbf{q}, \omega) = \frac{q^4}{m^2(\omega^2 - \omega_c^2)^2} \left[ \kappa_{int}^{-1} - 2\omega_c \eta_H(\omega) + \zeta(\omega) \frac{\omega}{i} + \eta^S(\omega) \frac{\omega^2 + \omega_c^2}{i\omega} \right]. \quad (4.135)$$

And at zero frequency  $\omega = 0$ , the static susceptibility is

$$\chi^{(4)}(\mathbf{q}, \omega = 0) = \frac{q^4}{m^2\omega_c^4} \left[ \kappa_{int}^{-1} - 2\omega_c \eta_H(\omega = 0) + \omega_c^2 \lim_{\omega \rightarrow 0} \left( \frac{\eta^S(\omega)}{i\omega} \right) - i \lim_{\omega \rightarrow 0} (\omega \zeta(\omega)) \right]. \quad (4.136)$$

We stress that these relations are obtained under the only assumption of Galilean invariance. Thus, the Hall viscosity is guaranteed to show up in the  $q^4$  term in the density response function for a wide range of systems.

#### 4.4.2 Example: Integer Quantum Hall Systems

We apply the above results to discuss the paradigm example of integer quantum Hall effect. The Hamiltonian involves only the kinetic part  $\hat{H}_0 = \sum_i \hat{\pi}_\mu^i \hat{\pi}_\mu^i / 2m = \hbar\omega_c \sum_i (\hat{a}_i^\dagger \hat{a}_i + 1/2)$ , where the ladder operator for Landau levels is  $\hat{a}_i = (\hat{\pi}_x^i + i\hat{\pi}_y^i) / \sqrt{2\hbar eB}$ , with the commutation relation  $[\hat{a}_i, \hat{a}_j^\dagger] = \delta_{ij}$ . Working in the spherical gauge  $\hat{\mathbf{A}}^i = \frac{B}{2}(-\hat{y}^i, \hat{x}^i, 0)$ , and defining  $\hat{\mathbf{R}}^i = \hat{\mathbf{p}}^i + e\hat{\mathbf{A}}^i$ , we can introduce  $\hat{b}_i = (\hat{R}_x^i - i\hat{R}_y^i) / \sqrt{2\hbar eB}$ , with  $[\hat{b}_i, \hat{b}_j^\dagger] = \delta_{ij}$ . It specifies the degeneracy within each Landau level in terms of angular momentum  $\hat{L}_z = \hbar \sum_i (\hat{b}_i^\dagger \hat{b}_i - \hat{a}_i^\dagger \hat{a}_i)$ . Consider a ground state with the lowest  $\nu$  Landau levels fully filled; each level has degeneracy  $V/2\pi l_B^2$ . Using equation (4.130) we calculate the leading terms in susceptibility directly. Start from

$$\chi(\mathbf{q}, \omega) = -\frac{i}{\hbar} \int_0^\infty dt e^{i\omega t} \int d^2x e^{-i\mathbf{q}\cdot\mathbf{x}} \langle [\hat{n}(\mathbf{x}, \tau), \hat{n}(\mathbf{0}, 0)] \rangle_0$$

we can explicitly calculate the charge susceptibility  $\chi(\mathbf{q}, \omega)$  up to the fourth order term

$$\chi^{(2)}(\mathbf{q}, \omega) = (ql_B)^2 \frac{\bar{n}\omega_c}{\hbar((\omega^+)^2 - \omega_c^2)}, \quad (4.137)$$

$$\chi^{(4)}(\mathbf{q}, \omega) = (ql_B)^4 \frac{\varepsilon}{\hbar^2} \left( \frac{1}{(\omega^+)^2 - 4\omega_c^2} - \frac{1}{(\omega^+)^2 - \omega_c^2} \right). \quad (4.138)$$

Here the energy density is  $\varepsilon = (eBv)^2/4\pi m$ , and the average density is  $\bar{n} = v/2\pi l_B^2$ , where the magnetic length  $l_B^2 = \hbar/eB$ .

Next we use (4.134) (4.135) to calculate the same terms in susceptibility so as to verify the susceptibility-viscosity relations. The zeroth order term in conductivity is directly obtained from the Kubo formula (4.131),

$$\sigma_{\mu\nu}^{(0)}(\omega) = \frac{ie^2\bar{n}}{m\omega^+} \frac{\omega^2}{(\omega^+)^2 - \omega_c^2} \delta_{\mu\nu} + \frac{\bar{n}e^2\omega_c}{m(\omega_c^2 - \omega^2)} \epsilon_{\mu\nu}, \quad (4.139)$$

which reduces to the familiar one  $\sigma_{\mu\nu}^{(0)}(\omega = 0) = e^2v/h$  at zero frequency. Using (4.134) we obtain (4.137). Further [119],

$$\kappa_{int}^{-1} = 2\varepsilon, \quad \zeta(\omega) = 0, \quad \eta^S(\omega) = \frac{i\omega^+\varepsilon}{(\omega^+)^2 - 4\omega_c^2}, \quad \eta_H(\omega) = \frac{2\omega_c\varepsilon}{4\omega_c^2 - (\omega^+)^2}. \quad (4.140)$$

Then from (4.135) we have (4.138), as expected.

We can further obtain the dynamic structure factor  $S(\mathbf{q}, \omega)$  [127] using the fluctuation-dissipation theorem  $\text{Im}\chi(\mathbf{q}, \omega) = -\frac{\pi}{\hbar v} (S(\mathbf{q}, \omega) - S(-\mathbf{q}, -\omega))$ , and the identity  $\frac{1}{x \pm i\epsilon} = \mathcal{P}_x^1 \mp \pi i\delta(x)$ ,

$$S^{(2)}(\mathbf{q}, \omega) = (ql_B)^2 \frac{N}{2} \delta(\omega - \omega_c), \quad (4.141)$$

$$S^{(4)}(\mathbf{q}, \omega) = (ql_B)^4 \frac{Nv}{8} [\delta(\omega - 2\omega_c) - 2\delta(\omega - \omega_c)]. \quad (4.142)$$

The static structure factor [127]  $S(\mathbf{q}) = (1/N) \int_0^\infty d\omega S(\mathbf{q}, \omega) = \langle \hat{n}(\mathbf{q})\hat{n}(-\mathbf{q}) \rangle$  is then

$$S(\mathbf{q}) = \frac{(ql_B)^2}{2} - \frac{v}{8}(ql_B)^4 + \mathcal{O}((ql_B)^6). \quad (4.143)$$

For  $v = 1$ , it reduces to the first two terms in the expansion of the well-known result  $S(\mathbf{q}) = 1 - e^{-(ql_B)^2/2}$  for a system with fully-filled lowest Landau level [131].

### 4.4.3 Hydrodynamic analysis

Having performed the strict microscopic analysis, it is interesting to see whether there is a macroscopic derivation of the susceptibility-viscosity relations (4.135) (4.136), which would provide a simpler and more intuitive way to understand them. To this end, we next show that (4.135) and (4.136) can be reproduced by pure classical hydrodynamic equations, despite the underlying highly quantum structure of the electronic liquid. Such a method has been adopted to discuss the fractional quantum Hall liquids and Bose-Einstein condensates recently [67, 122–124, 132, 133].

In hydrodynamics, the microscopic details are averaged over, giving a few effective macroscopic variables,

$$n(\mathbf{r}, t) = \bar{n} + \delta n(\mathbf{r}, t), \quad \mathbf{u}(\mathbf{r}, t) = \bar{\mathbf{u}} + \mathbf{v}(\mathbf{r}, t). \quad (4.144)$$

Here  $n, \mathbf{u}$  are the macroscopically averaged number density and the velocity respectively, including the equilibrium value  $\bar{n}, \bar{\mathbf{u}}$ , and the small deviation  $\delta n(\mathbf{r}, t), \mathbf{v}(\mathbf{r}, t)$  caused by external perturbation. The dynamics is given by the Navier-Stokes equation (momentum conservation) (4.128), where the momentum  $\mathbf{p} = mn\mathbf{u}$ . The force comes from the Lorentz force of the uniform magnetic field and the external potential perturbation  $\mathbf{f} = -enB\mathbf{e}_z \times \mathbf{u} - n\nabla\varphi(\mathbf{r}, t)$ . The stress tensor is

$$T_{\mu\nu} = P_{int}\delta_{\mu\nu} + mn u_\mu u_\nu - \delta T_{\mu\nu}, \quad (4.145)$$

where the viscous part  $\delta T_{\mu\nu}$  is given by (4.122)-(4.124), and  $P_{int}$  is the internal pressure introduced earlier. We stress that  $P_{int}$  excludes the contribution to the pressure from the Lorentz force exerted on the edge current, and therefore is suitable to be used here, as the Navier-Stokes equation only concerns bulk properties and assumes no boundary effect. Consider the linear response regime where  $\delta n(\mathbf{r}, t), \mathbf{v}(\mathbf{r}, t)$  are kept up to linear order, and



use the equilibrium value  $\bar{n} = \text{constant}$ ,  $\bar{\mathbf{u}} = 0$ , the Navier-Stokes equation (4.128) becomes

$$m\bar{n}\partial_t\mathbf{v} = (e\bar{n}B + \eta^H\Delta)(\mathbf{v} \times \mathbf{e}_z) + \nabla(\zeta\nabla \cdot \mathbf{v} - \bar{n}\varphi - P_{int}) + \eta^S\Delta\mathbf{v}, \quad (4.146)$$

On the other hand, the particle conservation, also kept up to linear order, gives

$$\partial_t\delta n + \bar{n}\nabla \cdot \mathbf{v} = 0, \quad (4.147)$$

Then applying the alternative expression for compressibility  $\kappa_{int} = \frac{1}{\bar{n}}\frac{\partial n}{\partial P_{int}}$ , which gives  $\nabla P_{int} = \kappa_{int}^{-1}(\nabla\delta n)/\bar{n}$ , we have the density response to potential perturbation  $\delta n = \chi\varphi$ , where the susceptibility (in momentum space) reads

$$\chi(\mathbf{q}, \omega) = \frac{\bar{n}^2 q^2}{m\bar{n}\omega^2 - \left(\frac{\kappa_{int}^{-1}}{i\omega} - \eta^S - \zeta\right)i\omega q^2 + \frac{(m\bar{n}\omega_c - \eta^H q^2)^2}{\eta^S q^2 / i\omega - m\bar{n}}}. \quad (4.148)$$

In the low momentum expansion, the  $q^2$  term is exactly given by that for the integer quantum Hall effect (4.137). This is because the intra-Landau level excitations start from the  $q^4$  term [131]. Thus, the  $q^2$  contribution must entirely come from inter-Landau level excitations, whose characters are captured by the integer quantum Hall effect. The  $q^4$  term is given by the same equation (4.135), as being derived from the Kubo formula. Thus, in the low-momentum regime, the classical hydrodynamics reproduces the strict susceptibility-viscosity relations obtained from Kubo formulae.

(In general, the viscosity coefficients  $\zeta, \eta^S, \eta_H$  would have momentum dependence also [115, 116]. In the expansion of (4.148) discussed above, we have taken the viscosity coefficients  $\zeta, \eta^S, \eta_H$  to be constant (they only depend on frequency). This is sufficient when we expand  $\chi(q, \omega)$  up to  $q^4$  terms, as can be seen from (4.148). But when applying (4.148) to higher orders in  $q$ , one needs to first expand  $\zeta, \eta^S, \eta_H$  to higher powers in  $q$  (i.e.  $q^0$  and  $q^2$  terms for  $\zeta, \eta^S, \eta_H$ ) before expanding (4.148) (i.e. to  $q^6$  term for  $\chi(q, \omega)$ )).

#### 4.4.4 Obtaining Hall Viscosity through Density Response Signatures

The relations (4.135), (4.136) connect the Hall viscosity with the susceptibility, which can be measured by scattering experiments. Since many recent works only concern the zero frequency value of Hall viscosity  $\eta_H(\omega = 0)$ , we focus on equation (4.136) here. Note that in most cases the bulk viscosity  $\zeta(\omega)$  does not diverge [119] at zero frequency. Then the last term in equation (4.136) vanishes and the formula can be rewritten as

$$\eta_H = \frac{\kappa_{int}^{-1}}{2\omega_c} + \frac{\omega_c}{2} \lim_{\omega \rightarrow 0} \left( \frac{\eta^S}{i\omega} \right) - \frac{m^2 \omega_c^3}{2} \frac{\chi^{(4)}(q)}{q^4}. \quad (4.149)$$

In order to extract  $\eta_H$  from the measurement of  $\chi^{(4)}(q)$ , one has to determine the first two terms in (4.149). The inverse internal compressibility  $\kappa_{int}^{-1} = B^2(\partial^2 \varepsilon(B)/\partial B^2)_v$  can be determined by the auxiliary measurement of magnetic susceptibility  $\chi_M = \mu_0 \left( \frac{\partial M}{\partial B} \right)_v = -\mu_0 \left( \frac{\partial^2 \varepsilon}{\partial B^2} \right)_v$  at constant filling fraction, or a local current measurement in response to the inhomogeneous magnetic field [118]  $\delta \mathbf{j} = \nabla \times \delta \mathbf{M} = -\varepsilon''(B) \mathbf{e}_z \times \nabla \delta B$ . In particular, in high magnetic field where Landau level mixing is negligible, the interaction energy can be neglected compared with the kinetic energy. Then we have the free particle results  $\varepsilon = \frac{(eBv)^2}{4\pi m}$  and  $\varepsilon = \frac{(eB)^2 v}{4\pi m}$  for integer and fractional quantum Hall systems respectively, giving  $\kappa_{int}^{-1} = 2\varepsilon$ .

Further,  $\lim_{\omega \rightarrow 0}(\eta^S/i\omega)$  generally yields a finite value (see the integer quantum Hall system for example), and needs careful evaluations. Here we invoke the Kubo formula for shear viscosity [119],  $\eta^S = \frac{\hbar\omega^+}{V} \int_0^\infty e^{i\omega^+ t} \langle [\hat{J}_{12}(t), \hat{J}_{12}(0)] \rangle_0$ , to compute this quantity.  $\hat{J}_{12}$  is the off-diagonal element of the strain generator  $\hat{J}_{\mu\nu}$ . In the spectral representation,

$$\frac{\eta^S}{i\omega} = \frac{2\hbar}{V} \sum_n \frac{\omega_{n0} |\langle 0 | \hat{J}_{12}(0) | n \rangle|^2}{(\omega^+)^2 - \omega_{n0}^2}, \quad (4.150)$$

where  $\omega_{n0} = \omega_n - \omega_0$ , with  $\omega_n$  the frequency of energy eigenstate  $|n\rangle$ . (In the presence of Landau level mixing,  $|n\rangle$  also includes higher Landau level eigenstates). Therefore, if

$\omega_{n0} = 0$  or the matrix element vanishes, the corresponding term is zero; otherwise, we have the finite result

$$\lim_{\omega \rightarrow 0} \left( \frac{\eta^S}{i\omega} \right) = -\frac{2\hbar}{V} \sum'_n \frac{|\langle 0 | \hat{J}_{12}(0) | n \rangle|^2}{\omega_{n0}}, \quad (4.151)$$

where  $\sum'$  means summing over energy eigenstates which are not degenerate with the ground state. Explicitly, the off-diagonal element of the strain generator assumes the form  $\hat{J}_{12}(0) = \sum_i \left( -\{\hat{x}^i, \hat{\pi}_y^i\} - eB\hat{x}^i{}^2 \right) / 2\hbar$ , and can be written conveniently in the spherical gauge  $\hat{\mathbf{A}}^i = \frac{1}{2}\mathbf{B} \times \hat{\mathbf{r}}^i$  as

$$\hat{J}_{12}(0) = -\sum_i \frac{\hat{x}^i \hat{p}_y^i}{\hbar} = -\frac{1}{4} \sum_i [(\hat{a}_i - \hat{a}_i^\dagger)^2 - (\hat{b}_i - \hat{b}_i^\dagger)^2]. \quad (4.152)$$

where  $\hat{a}_i, \hat{b}_i$  are inter- and intra-Landau level ladder operators defined previously. Consider, for instance, integer quantum Hall effect. Then the only non-zero matrix element in (4.151) is  $\langle 0 | \hat{a}_i^2 | 2 \rangle$ , where  $|2\rangle$  means the state with one electron from either of the top two filled Landau levels in the ground state being excited 2 levels upwards, corresponding to an excitation energy  $\omega_{20} = 2\omega_c$ . Thus,  $\lim_{\omega \rightarrow 0} (\eta^S / i\omega) = -\varepsilon / 4\omega_c^2$ , in consistency with the previous result. The evaluation for various fractional quantum Hall systems is left for future work, which generally requires a numerical evaluation of (4.151) and (4.152) in the presence or absence of Landau level mixings depending on specific experimental situations.

Thus, with  $\kappa_{int}^{-1}$  and  $\lim_{\omega \rightarrow 0} (\eta^S / i\omega)$  being measured or calculated, one can use equation (4.149) to determine the Hall viscosity  $\eta_H$  through the long wavelength part of static susceptibility  $\chi^{(4)}(\mathbf{q}, \omega = 0)$ , which is related to scattering experiments [127]. Explicitly, the quantity being measured is the dynamic structure factor  $S(\mathbf{q}, \omega) = \sum_n S_n(\mathbf{q}) \delta(\omega - \omega_n(\mathbf{q}))$ , where  $\omega_n(\mathbf{q})$ 's are excitation modes. Using Kramers-Kronig relation  $\text{Re}\chi(\mathbf{q}, \omega) = (1/\pi) \int_{-\infty}^{\infty} dz \mathcal{P}(\text{Im}\chi(\mathbf{q}, z)) / (z - \omega)$  and fluctuation dissipation theorem, we have the static

susceptibility  $\chi(\mathbf{q}) = \chi(\mathbf{q}, \omega = 0)$  as

$$\chi(\mathbf{q}) = -\frac{2}{\hbar V} \sum_n \frac{S_n(\mathbf{q})}{\omega_n(\mathbf{q})}. \quad (4.153)$$

We can compare it to the situation in single mode approximation [131]. There  $S_n(\mathbf{q})$  becomes the static structure factor  $S(\mathbf{q})$  while  $\omega_n(\mathbf{q}) \rightarrow \Delta(\mathbf{q})$  corresponds to the single gapped mode. But a recent experiment [125] shows the existence of two collective modes. Thus, we keep the general form (4.153). But the presence of two or multiple modes does not affect the conclusion that intra-Landau level excitation corresponds to  $S(\mathbf{q}, \omega), \chi(\mathbf{q}, \omega)$  starting from  $q^4$ . This can be seen by applying the  $f$ -sum rule [127]  $\int_0^\infty \omega S(\mathbf{q}, \omega) d\omega = \hbar N q^2 / 2m$  and (4.137). Then we see the sum rule is saturated by the inter-Landau level excitations, meaning that the  $q^2$  term comes entirely from the cyclotron mode.

The qualitative behavior of  $\chi(\mathbf{q})$  in the small- $q$  limit can be observed as follows. Using the compressibility sum rule  $\chi(\mathbf{q} \rightarrow 0) = -N\kappa_T^{-1}$  and the incompressible feature of quantum Hall states, we see the constant term in  $\chi(\mathbf{q})$  always vanishes. Here  $\kappa_T^{-1} = -V(\partial P / \partial V)_{N,B}$  is the isothermal compressibility. Moreover, the low-lying excitations within the lowest Landau level correspond to  $\chi(\mathbf{q})$  starting from the  $q^4$  term. That means if the inter-Landau level excitation is suppressed in the large magnetic field limit, (or if we can cancel such contribution by subtracting the  $\chi^{(2)}$  given by equation (4.137)),  $\chi^{(4)}$  is the leading order in  $\chi(\mathbf{q})$ . In sum, the algebraic relation (4.153) clearly means that it will be sufficient to extract the  $q^4$  term in  $\chi(\mathbf{q})$  by measuring only the long wavelength part of  $S(\mathbf{q}, \omega)$ , as is usually the case in current experiments.

## 4.5 Conclusion and outlook

The relation between susceptibility and viscosity in (4.135) and (4.136) is presented and discussed, showing the role of viscosity coefficients in the  $q^4$  term of susceptibility for

a general class of Galilean invariant system. It suggests the possibility of measuring the Hall viscosity in terms of density response experiments for a wide range of quantum Hall systems.

In addition, it is worth mentioning the connection of this work with cold atom systems, where quantum Hall states can be simulated using rotating atomic gases. The quantum Hall state is approached when the rotation frequency of the trapped gas approaches the critical frequency, where the centrifugal force almost cancels the trapping force, and the Galilean invariance is approximately satisfied. Since in cold atom systems, the density measurement and the potential engineering are the most standard experimental tools and can be made to high accuracy, our analysis paves the way for further discussions of Hall viscosity signatures in cold atom experiments.

## Bibliography

- [1] S. Eckel *et. al.* *Nature*, 506:200, 2014.
- [2] M.H. Anderson *et al.* *Science*, 269:5221, 1995.
- [3] C. A. Regal *et. al.* *Phys. Rev. Lett.*, 92:040403, 2004.
- [4] M.W. Zwierlein *et. al.* *Phys. Rev. Lett.*, 92:140403, 2004.
- [5] C. Chin *et. al.* *Science*, 305:1128, 2004.
- [6] M. Greiner *et. al.* *Nature*, 415:39, 2002.
- [7] I. Bloch. *Nature Phys.*, 1:23, 2002.
- [8] N. Flaschner *et. al.* *Science*, 352:1091, 2016.
- [9] L. Duca *et. al.* *Science*, 347:288, 2015.
- [10] J. Struck *et. al.* *Science*, 333:996, 2011.
- [11] L. Tarruell *et. al.* *Nature*, 483:302, 2012.
- [12] P. Soltan-Panahi *et. al.* *Nature Physics*, 7:434, 2011.
- [13] M. Weinberg *et. al.* *2D Materials*, 3:024005, 2016.
- [14] G. Jo *et. al.* *Phys. Rev. Lett.*, 108:045305, 2012.
- [15] M. Aidelsburger *et. al.* *Nature Physics*, 11:162, 2015.
- [16] M. Atala *et. al.* *Nature Physics*, 10:588, 2014.
- [17] M. Aidelsburger *et. al.* *Phys. Rev. Lett.*, 111:185301, 2013.
- [18] T. L. Ho. *Phys. Rev. Lett.*, 81:742, 1998.
- [19] T. Ohmi and K. Machida. *J. Phys. Soc. Jpn.*, 67:1822, 1998.
- [20] Yuki Kawaguchia and Masahito Ueda. *Physics Reports*, 520:253, 2012.

- [21] D. M. Stamper-Kurn and Masahito Ueda. *Rev. Mod. Phys.*, 85:1191, 2013.
- [22] T. L. Ho and S. K. Yip. *Phys. Rev. Lett.*, 82:247, 1999.
- [23] J. Heinze *et. al.* *Phys. Rev. Lett.*, 110:250402, 2013.
- [24] J. S. Krauser *et. al.* *Nat. Phys.*, 8:813, 2012.
- [25] J. S. Krauser *et. al.* *Science*, 343:157, 2014.
- [26] *et. al.* M. Mancini. *Science*, 349:1510, 2015.
- [27] *et. al.* X. Zhang. *Science*, 345:1467, 2015.
- [28] C. Wu *et. al.* *Phys. Rev. Lett.*, 91:186402, 2003.
- [29] J. Jaramillo *et. al.* *Phys. Rev. A*, 88:043616, 2013.
- [30] K. Rodriguez *et. al.* *Phys. Rev. Lett.*, 105:050402, 2010.
- [31] J. Jaramillo *et. al.* *Phys. Rev. A*, 88:043616, 2013.
- [32] Y. Dong and H. Pu. *Phys. Rev. A*, 87:043610, 2013.
- [33] M. A. Cazalilla and A. M. Rey. *Rep. Prog. Phys.*, 77:124401, 2014.
- [34] N.D. Mermin. *Physica*, 90B:1, 1971.
- [35] N.D. Mermin. *Rev. Mod. Phys.*, 51:591, 1977.
- [36] A. M. Turner, V. Vitelli, and D. R. Nelson. *Rev. Mod. Phys.*, 82:1301, 2010.
- [37] F. de Juan *et. al.* *Phys. Rev. B*, 76:165409, 2007.
- [38] X. G. Wen. *Phys. Rev. B*, 40:7387, 1989.
- [39] X. G. Wen. *Int. J. Mod. Phys.*, page 239, 1990.
- [40] X. G. Wen and Q. Niu. *Phys. Rev. B*, 41:9377, 1990.
- [41] N. Schine *et. al.* *arXiv:1511.07381*, 2015.
- [42] M. Lu *et. al.* *Phys. Rev. Lett.*, 107:190401, 2011.
- [43] M. Lu *et. al.* *Phys. Rev. Lett.*, 108:215301, 2012.
- [44] <https://www.uibk.ac.at/exphys/ultracold/atomtraps.html>.
- [45] A. Griesmaier *et al.* *Phys. Rev. Lett*, 94:160401, 2005.

- [46] K. Aikawa *et. al.* *Phys. Rev. Lett.*, 108:210401, 2012.
- [47] Mingwu Lu *et. al.* *PRL 107*, 108:190401, 2011.
- [48] M. Lu, N. Q. Burdick, and B. L. Lev. *Phys. Rev. Lett.*, 108:215301, 2012.
- [49] A. V. Gorshkov *et. al.* *Nat. Phys.*, 6:289, 2010.
- [50] H. Makela and K.-A. Suominen. *Phys. Rev. Lett.*, 99:190408, 2007.
- [51] J. J. Sakurai and J. Napolitano. *Modern Quantum Mechanics*, pp. 232-238. Addison Wesley, Second edition, 2010.
- [52] D. M. Stamper-Kurn and M. Ueda. *Rev. Mod. Phys.*, 85:1191, 2013.
- [53] D. M. Brink and G. R. Satchler. *Angular Momentum*. Clarendon Press, Oxford, Second edition, 1968.
- [54] E. Majorana. *Nuovo Cimento*, 9:43, 1932.
- [55] R. Barnett *et. al.* *Phys. Rev. Lett.*, 97:180412, 2006.
- [56] A. Lamacraft. *Phys. Rev. B*, 81:184526, 2010.
- [57] Y. Kawaguchi and M. Ueda. *Phys. Rev. A*, 84:053616, 2011.
- [58] M. Fizia and K. Sacha. *J. Phys. A: Math. Theor.*, 45:045103, 2012.
- [59] H. Makela and K.-A. Suominen. *Phys. Rev. Lett.*, 99:190408, 2007.
- [60] R. Barnett *et. al.* *Phys. Rev. B*, 80:024420, 2009.
- [61] J. J. Sakurai and J. Napolitano. *Modern Quantum Mechanics*. Addison Wesley, Second edition, 2010.
- [62] N. D. Mermin. *Rev. Mod. Phys.*, 51:591, 1979.
- [63] H. Makela and K.-A. Suominen. *Phys. Rev. Lett.*, 99:190408, 2007.
- [64] M. Vengalattore *et. al.* *Phys. Rev. Lett.*, 100:170403, 2008.
- [65] W. Zwerger. *The BCS-BEC Crossover and the Unitary Fermi Gas*. Springer, First edition, 2012.
- [66] A. Auerbach. *Interacting Electrons and Quantum Magnetism*. Springer, First edition, 1998.
- [67] C. J. Pethick and H. Smith. *Bose-Einstein Condensation in Dilute Gases*. Cambridge University Press, Second edition, 2008.



- [68] A. A. Abrikosov *et. al.* *Methods of Quantum Field Theory in Statistical Physics*. Dover, New York, 1975.
- [69] X.-G. Wen and A. Zee. *Phys. Rev. Lett.*, 69:953, 1992.
- [70] J. E. Avron *et. al.* *Phys. Rev. Lett.*, 75:697, 1995.
- [71] N. Read. *Phys. Rev. B*, 79:045308, 2009.
- [72] N. Read and E. H. Rezayi. *Phys. Rev. B*, 84:085316, 2011.
- [73] N. Cooper. *Advances in Phys.*, page 539, 2008.
- [74] A. L. Fetter. *Rev. Mod. Phys.*, page 647, 2009.
- [75] *et. al.* M. R. Matthews. *Phys. Rev. Lett.*, 83:3358, 1999.
- [76] K. W. Madison *et. al.* *Phys. Rev. Lett.*, 84:806, 2000.
- [77] J. R. Abo-Shaeer *et. al.* *Science*, 292:476, 2001.
- [78] P. Engels *et. al.* *Phys. Rev. Lett.*, 89:100403, 2002.
- [79] V. Schweikhard *et. al.* *Phys. Rev. Lett.*, 92:040404, 2004.
- [80] M. W. Zwierlein *et. al.* *Nature*, 435:1047, 2005.
- [81] Y.-J. Lin *et. al.* *Nature*, 462:628, 2009.
- [82] M. Aidelsburger *et. al.* *Phys. Rev. Lett.*, 111:185301, 2013.
- [83] C. J. Kennedy *et. al.* *arXiv:1503.08243*, 94:160401, 2005.
- [84] A. Eckardt *et. al.* *Phys. Rev. Lett.*, 95:260404, 2005.
- [85] P. Hauke *et. al.* *Phys. Rev. Lett.*, 109:145301, 2012.
- [86] G. Jotzu *et. al.* *Nature*, 515:237–240, 2014.
- [87] M. Lewenstein, A. Sanpera, and V. Ahufinger. *Ultracold atoms in optical lattices: Simulating quantum many-body systems*. Oxford University Press, Oxford, 2012.
- [88] N. Goldman *et. al.* *Rep. Prog. Phys.*, page 126401, 2014.
- [89] O. Boada *et. al.* *New J. Phys.*, page 045007, 2015.
- [90] L. J. LeBlanc *et. al.* *New J. Phys.*, 17:065016, 2015.
- [91] A. L. Fetter. *Rev. Mod. Phys.*, 81:647, 2009.

- [92] N. Goldman *et. al.* *Rep. Prog. Phys.*, 77:126401, 2014.
- [93] N. Goldman and J. Dalibard. *Phys. Rev. X*, 4:031027, 2014.
- [94] T.-L. Ho and V. Shenoy. *Phys. Rev. Lett.*, 77:2595, 1996.
- [95] J.-Y Choi *et. al.* *Phys. Rev. Lett.*, 111:245301, 2013.
- [96] M. W. Ray *et. al.* *Nature*, 505:657, 2014.
- [97] L. D. Landau and E.M. Lifshitz. *Mechanics, Course of Theoretical Physics*. Butterworth-Heinemann, Third edition, 1976.
- [98] M. W. Ray *et. al.* *Nature*, 505:657, 2014.
- [99] T.L. Ho. *Phys. Rev. Lett.*, 87:060403, 2001.
- [100] G. Watanabe *et. al.* *Phys. Rev. A*, 74:063621, 2006.
- [101] E. Nugent. *Novel Traps for Bose-Einstein Condensates*. Ph.D. Thesis, Oxford, 2009.
- [102] S. Eckel *et. al.* *Phys. Rev. X*, 4:031052, 2014.
- [103] R. Fickler *et. al.* *Science*, 338:640, 2012.
- [104] *et. al.* S. Franke-Arnold. *Laser Photonics Rev.*, 2:299, 2008.
- [105] *et. al.* M. Lacki. *Phys. Rev. A*, 93:013604, 2016.
- [106] K. Sun *et. al.* *Phys. Rev. A*, 91:063627, 2015.
- [107] M. Monastyrsky. *Topology of Gauge Fields and Condensed Matter*. Springer, 2013.
- [108] M. I. Monastyrsky and Birkhauser. *Riemann, Topology and Physics*. Boston, Second edition, 1999.
- [109] D. Vollhardt and P. Wolfle. *The Superfluid Phases of Helium 3*. Dover, 2013.
- [110] J. E. Avron, R. Seiler, and P. G. Zograf. *Phys. Rev. Lett.*, page 697, 1995.
- [111] J. E. Avron. *J. Stat. Phys.*, page 543, 1998.
- [112] I. V. Tokatly and G. Vignale. *J. Phys. Condens. Matter*, page 275603, 2009.
- [113] N. Read. *Phys. Rev. B*, page 045308, 2009.
- [114] N. Read and E. H. Rezayi. *Phys. Rev. B*, page 085316, 2011.
- [115] A. G. Abanov and A. Gromov. *Phys. Rev. B*, page 014435, 2014.

- [116] T. Can, M. Laskin, and P. Wiegmann. *Phys. Rev. Lett.*, page 046803, 2014.
- [117] P. Wiegmann and A. G. Abanov. *Phys. Rev. Lett.*, page 034501, 2014.
- [118] B. Bradlyn, M. Goldstein, and N. Read. *Phys. Rev. B*, page 245309, 2012.
- [119] C. Hoyos and D. T. Son. *Phys. Rev. Lett.*, page 066805, 2012.
- [120] R. Landig *et. al.* *Nat. Comm.*, page 7046, 2015.
- [121] D. X. Nguyen, D. T. Son, and C. Wu. *arXiv:1411.3316*, 2014.
- [122] I. V. Tokatly. *Phys. Rev. B*, page 205340, 2006.
- [123] I. V. Tokatly. *Phys. Rev. B*, page 035333, 2006.
- [124] I. V. Tokatly and G. Vignale. *Phys. Rev. Lett.*, page 026805, 2007.
- [125] C. F. Hirjibehedin *et. al.* *Phys. Rev. Lett.*, page 066803, 2005.
- [126] E. Taylor and M. Randeria. *Phys. Rev. A*, page 053610, 2010.
- [127] D. Pines and P. Nozieres. *The Theory of Quantum Liquids, vol.I.* Benjamin, New York, 1966.
- [128] G. D. Mahan. *Many-Particle Physics.* Springer, Third edition, 2013.
- [129] N. R. Cooper, B. I. Halperin, and I. M. Ruzin. *Phys. Rev. B*, page 2344, 1997.
- [130] X.-G. Wen. *Quantum Field Theory of Many-Body Systems.* Oxford University Press, Oxford, 2004.
- [131] S. M. Girvin, A. H. MacDonald, and P. M. Platzman. *Phys. Rev. B*, page 2481, 1986.
- [132] P. B. Wiegmann. *JETP*, page 617, 2013.
- [133] P. B. Wiegmann. *Phys. Rev. B*, page 241305(R), 2013.